TECHNISCHE UNIVERSITÄT WIEN

DISSERTATION

Infrared Reflection Absorption Spectroscopy with Angle Selection

zur Erlangung des akademischen Grades
Doktor der technischen Wissenschaften

unter Anleitung von
Univ.Prof. Gareth S. Parkinson Ph.D.

und Mitbetreuung von
Dr.techn. Jiří Pavelec

im Rahmen des Studiums
Doktorat Technische Physik

ausgeführt am Institut für Angewandte Physik
der Fakultät für Physik

eingereicht von

Dipl.-Ing. David A. Rath BSc
01225498

Wien, 5. September 2024

ACKNOWLEDGEMENTS

I would like to begin by thanking my supervisor, Gareth S. Parkinson, for involving me in his research project and for his ongoing support throughout this journey. His guidance has been instrumental in bringing my ideas to life and successfully completing this project. I am also grateful for the opportunities he provided for both my professional and personal growth.

I would also like to express my sincere thanks to my co-supervisor, Jiří Pavelec, for his support and for encouraging me to approach problems from new perspectives. His creative ideas and our many valuable discussions significantly enriched the quality of this work.

My thanks go to Michael Schmid for his assistance and for sharing his expertise in physics. His constructive feedback and thoughtful guidance were essential in shaping this project and gave me a deeper understanding of applying physics to practical challenges.

I would also like to extend my gratitude to Ulrike Diebold for her valuable input and for providing the resources necessary to complete this thesis. Her influence was a significant factor in my decision to pursue a PhD.

I am thankful to all the members of the Surface Physics Group for their support and the many insightful conversations we shared. Your openness to discussion and collaboration made this experience both productive and enjoyable. I also thoroughly enjoyed the time together in the coffee room and the fun moments we shared at conferences. I am especially grateful to Chunlei Wang and Moritz Eder for their invaluable assistance in the lab as well as to the students Vojtěch Mikerásek and Daniel Mittag for their collaboration and hard work.

Outside the group, I want to thank Anna Niggas for her unwavering support and for being a great listener, especially during the more challenging times.

I also appreciate the support of Rainer Gärtner and Herbert Schmidt, who helped me bring my ideas to reality and provided friendly conversation (a “Plauscherl”) along the way.

Finally, I want to express my deepest gratitude to my parents, brother, and grandparents for their continuous support throughout my PhD journey. Their encouragement and belief in me have been invaluable, and I am truly thankful for all they have done.

ABSTRACT

Performing Infrared Reflection Absorption Spectroscopy (IRAS) experiments on bulk oxide single crystals presents a challenge because the highest sensitivity to adsorbates on these surfaces coincides with regions of low infrared reflectivity. Unlike on metallic substrates, where the surface selection rules are valid, there is no enhancement of the IR signals originating from changing dipole moments normal to the surface. In addition, the band inversion occurring for measurements with p-polarised light on non-metallic substrates results in positive and negative oriented peaks, which, if a wide incidence angle range is used, can significantly reduce the signals.

The IRAS system presented in this thesis has been developed to optimise measurement parameters for non-metallic substrates, thereby maximising the signal-to-noise ratio. It utilises the commercial FTIR spectrometer Bruker VERTEX 80v to conduct IRAS measurements under ultra-high vacuum (UHV) conditions in a custom-built UHV surface chemistry chamber. The optimisation is accomplished by a solid design framework focusing on maximising IR light throughput, selecting optimal incidence angle ranges and high mechanical stability. This achieves a maximum signal-to-noise ratio and high long-term stability. To realise a high-throughput optics, the optical design incorporates sample illumination and light collection from the sample using elliptical mirrors with high numerical aperture, placed in UHV. Additionally, two adjustable aperture plates are implemented to enhance the signal-to-noise ratio, enabling the selection of the incidence angle range. This feature is essential for adequately handling the band inversion. The optimum incidence angle range selection is determined based on the calculation of the normalised reflectivity difference ($\Delta R/R_0$). This thesis expands the ideal picture of $\Delta R/R_0$ by examining the influence of incidence angle spread, depolarisation, and illumination of adsorbate-free sample areas, all decreasing the achievable signal intensities, with the depolarisation having the most significant impact.

Furthermore, the long-term stability of the IRAS system is ensured by connecting all components to a central flange. In addition to performance-enhancing features, the IRAS system includes a sample-position finder. A cooling system for the optics in high vacuum eliminates the need to disconnect the IRAS during a bakeout and realign the optics after the bakeout, thus enhancing user-friendliness.

To evaluate the performance of the system, 1 ML CO on reduced $TiO_2(110)$ was studied by utilising various angle rages leading to an signal-to-noise ratio (SNR) of about 70 and a peak height of 1.83×10^{-3} in the $\Delta R/R_0$ spectrum. These results were obtained at a resolution of $4\,cm^{-1}$ and 1000 scans within 5 minutes total measurement time for one IR spectrum. Additionally, the IRAS spectra of one monolayer D_2O adsorbed on a hydroxylated $TiO_2(110)$ surface show the s-polarised performance of the IRAS system. In this case, a SNR of about 65 was achieved with a $\Delta R/R_0$ peak height of 1.4×10^{-4}, 4000 scans and a resolution of $4\,cm^{-1}$ in 20 minutes.

KURZFASSUNG

Die Infrarot-Reflexions-Absorptions-Spektroskopie (IRAS) auf Oxid-Einkristallen stellt eine Herausforderung dar. Die höchste Empfindlichkeit gegenüber adsorbierten Molekülen auf diesen Oberflächen fällt mit Bereichen geringer Infrarotreflektivität zusammen. Anders als auf metallischen Substraten, wo die Oberflächenauswahlregeln gelten, gibt es keine Verstärkung der IR-Signale, die von veränderlichen Dipolmomenten senkrecht zur Oberfläche stammen. Des Weiteren führt die Signalinversion, die für p-Polarisation auf nichtmetallischen Substraten auftritt, zu positiv und negativ orientierten Signalen. Große Einfallswinkelbereiche können zu einer erheblichen Reduktion der gemessenen Signale führen.

Das in dieser Dissertation vorgestellte IRAS-System wurde entwickelt, um die Messparameter für nichtmetallische Substrate zu optimieren und somit das Signal-Rausch-Verhältnis zu maximieren. Für IRAS-Messungen unter Ultrahochvakuumbedingungen wird das kommerzielle FTIR-Spektrometer Bruker VERTEX 80v verwendet. Es wird in Kombination mit dem entwickeltem IRAS-System an einer auf Oberflächenchemie spezialisierten Ultrahochvakuumkammer eingesetzt. Die Optimierung des IRAS-Systems basiert auf einer soliden Designgrundlage. Diese konzentriert sich auf einen maximalen IR-Lichtdurchsatz, die Auswahl optimaler Einfallswinkelbereiche und die mechanische Stabilität des Systems. Dadurch wird ein maximales Signal-Rausch-Verhältnis sowie hohe Langzeitstabilität erreicht. Um eine Optik mit hohem Lichtdurchsatz zu realisieren, umfasst das optische Design unter anderem zwei elliptische Spiegeln mit hoher numerischer Apertur, die im Ultrahochvakuum (UHV) platziert sind. Sie dienen dazu, die Probe zu beleuchten und das von der Probe reflektierte Licht einzusammeln. Zusätzlich wurden zwei einstellbare Blendenplatten eingebaut, um die Auswahl des Einfallswinkelbereichs zu ermöglichen. Diese Maßnahme verbessert das Signal-Rausch-Verhältnis. Die Implementierung der Blendenplatten ist für die korrekte Berücksichtigung der Signalinversion unerlässlich. Die Auswahl des optimalen Einfallswinkelbereichs erfolgt auf der Grundlage der Berechnung der normalisierten Reflektivitätsdifferenz $\Delta R/R_0$. In dieser

Arbeit wird das Idealbild von $\Delta R/R_0$ erweitert. Der Einfluss des Bereichs des Einfallswinkels, der Depolarisation und der Beleuchtung von Probenbereichen ohne Adsorbat wird analysiert. Diese Faktoren führen allesamt zu einer Verringerung der erreichbaren Signalintensitäten. Dabei hat die Depolarisation den größten Einfluss.

Die Langzeitstabilität des IRAS-Systems durch die Verbindung aller Komponenten über einen zentralen Flansch gewährleistet. Das IRAS-System weist zudem eine Probenpositionierungshilfe auf. Durch ein Kühlsystem für die optischen Komponenten im Hochvakuum ist es nicht mehr erforderlich, das IRAS-System während des Ausheizvorgangs von der Messkammer abzukoppeln und die Optik nach dem Ausheizen neu auszurichten, was die Benutzerfreundlichkeit erhöht.

Zur Evaluierung der Leistungsfähigkeit des Systems wurden Messungen von 1 ML CO auf einer reduzierten $TiO_2(110)$ Oberfläche unter Verwendung verschiedener Einfallswinkelbereiche durchgeführt. Hier wurde ein Signal-Rausch-Verhältnis (SNR – von englisch signal-to-noise ratio) von 70 bei einer Signalintensität im $\Delta R/R_0$-Spektrum von $1{,}8\times10^{-3}$ erreicht. Dieses Ergebnis wurde mit einer Auflösung von $4\,\mathrm{cm}^{-1}$und 1000 Scans innerhalb von 5 Minuten erzielt. Des Weiteren demonstrieren die IRAS-Spektren einer Monolage D_2O, adsorbiert auf einer hydroxylierten $TiO_2(110)$-Oberfläche, die Leistung für s-polarisiertes IR Licht. In diesem Fall wurde ein SNR von 65 bei einer Signalintensität von $1{,}4\times10^{-4}$ bei 4000 Scans und einer Auflösung von $4\,\mathrm{cm}^{-1}$ in 20 Minuten erreicht.

CONTENTS

CHAPTER 1

INTRODUCTION

Global warming is a widely discussed topic in modern society, and its reduction is closely linked to the reduction of fossil energy consumption and the more efficient use of available resources. Catalysts play a crucial role in making chemical processes more energy-efficient. Developing new catalysts is mainly done through trial and error, as the processes driving catalytic reactions are complex and challenging to understand [1]. Another approach, which is still rare but the topic of research, is to develop catalysts from the bottom up. This involves understanding the fundamental processes and combining them to create new, efficient, selective and cost-effective heterogeneous catalysts. Metal oxides are cost-effective, selective and efficient and are thus promising materials to develop new heterogeneous catalysts [1]. To develop catalysts for actual environmental conditions, it is necessary to improve the understanding of fundamental processes gained in well-defined measurement conditions. Surface science provides this fundamental insight by utilising model systems, e.g., single crystals and performing very defined experiments in ultra-high vacuum (UHV); this is also known as the surface science approach [2].

Making the step from the idealised model systems used in surface science to more realistic catalysts requires a reliable measurement technique to characterise each step in this transition. Infrared spectroscopy fulfils this demand and is also a standard analysis tool for catalyst characterisation. This technique makes it possible to identify molecular species based on their characteristic vibrational frequencies. The tech-

nique's beauty lies in its applicability to defined and realistic conditions, making it an ideal bridging technique to connect fundamental research results to real catalysts [3, 4]. Furthermore, different variants of this technique allow its application on various substrates, reaching from powders (diffuse reflectance infrared Fourier transform spectroscopy (DRIFTS)) to flat single crystals (infrared reflection absorption spectroscopy (IRAS or IRRAS)).

In surface science, IRAS is used as it is sensitive to adsorbates on the surface. Synonyms for IRAS are external reflection spectroscopy (ERS) or reflection absorption IR spectroscopy (RAIS or RAIRS). The principle of IRAS is simple – IR light is detected after a single reflection off the sample surface. Combined with a Fourier transform infrared (FTIR) spectrometer, spectra are recorded to identify the adsorbates on the surface and their binding to the surface based on their vibrational frequencies. The measurement of reflected infrared light from adsorbate-covered samples was first explored by Francis and Ellison [5] with measuring on metal mirrors and further theoretically described by Greenler [6]. This served as the foundation for experimental work on the topic [7–10], which led to the development of experimental setups using multiple reflections [11] or single reflection IRAS setups [10, 12]. Nowadays, IRAS on metal surfaces is a well-established technique. It is sensitive only to dipole changes perpendicular to the metal surface, as described by the surface selection rules [6, 13–15]: The electric field normal to the surface is enhanced, leading to strong signals while the electric field parallel to the surface is negligible small, resulting in vanishing small signals.

Regarding non-metallic substrates, the situation is complicated due to the absence of or weak dipole enhancement. Additionally, the optimal sensitivity to adsorbate vibrations on the surface coincides with the range where these materials exhibit low reflectivity. Compared to metals, this leads to higher noise in the measurement and one to two orders smaller signals [16–20]. One way to preserve the advantage of the excellent metal reflectivity and high light-adsorbate interaction while measuring on surfaces of non-metals is to grow a thin film of a non-metallic material on metallic substrate [21, 22]. However, only dipole moment changes perpendicular to the surface can be measured. Furthermore, depending on the investigated non-metallic thin film, growth on a metal substrate may not be possible. In addition, the metallic substrate may influence the mechanical or electronic structure of the film. To ensure that this influence can be excluded, the use of bulk single crystals is necessary. One advantage of measuring on non-metallic bulk single crystals is that signals from all dipole moment orientations are accessible. Therefore, the s-polarised and the p-polarised components parallel to the surface can also be utilised to provide additional information about the molecule orientation on the surface and to probe vibrations parallel to the surface. As IRAS on these materials suffers from low signals and high noise, the measurement of sub-monolayer coverages is challenging and requires extended measurement times [16, 18, 23].

Recent advancements in surface science have led to significant insights into various oxide single crystal model systems, one example beeing TiO_2 with adsorbed water [23–

25] or CO [18, 26, 27], as well as many others [20, 28–30]. These fundamental studies are crucial for understanding the processes occurring on more complex catalysts, effectively bridging the "materials gap" [20, 31–33] by providing a deeper understanding of surface reactions. However, transitioning from model systems to real catalysts presents additional challenges: bridging the "pressure gap", which involves connecting results obtained under UHV with those under real catalytic conditions, typically at ambient or elevated pressures [32, 33]. IRAS (or infrared spectroscopy) is particularly well-suited for this purpose, as it can deliver meaningful results across a wide range of conditions and materials. While progress has been made in studying metal-oxide single crystals, building a robust foundation of well characterised and understood fundamental model systems is a promising strategy for enhancing our understanding of real-world catalysts.

This thesis aimed to develop an IRAS setup for investigating surface reactions of adsorbed molecules on non-metallic substrates helping to expand this foundation. The project required measuring low adsorbate coverages in the sub-monolayer regime on metal oxides using an existing surface analysis chamber. Achieving good measurement performance presented significant challenges due to the low reflectivity of the samples in the adsorbate-sensitive measurement range, spatial restrictions imposed by the chamber, losses due to optical components, a small measurement area and vacuum design-specific requirements. To address these challenges, a customised design approach and the introduction of the possibility of tuning the measurement parameters to their optimum for various materials was necessary. Calculations for the sensitivity of IRAS on non-metallic substrates and optical ray tracing simulations were performed to push the optimisation to its limit, laying the foundation for the design. Additionally, the design incorporates features to enhance the user-friendliness of the system.

The main results of this thesis have been published in Ref. [34]. The initial section of the thesis presents an introduction to the fundamentals of infrared spectroscopy. It begins with an elementary model for molecular vibrations. Subsequently, it explains the fundamental concept of a Fourier transform infrared spectrometer (FTIR) and provides further insights into infrared absorption spectroscopy (IRAS) and its theoretical basis. These basic concepts are then employed to develop a framework for designing and optimising optical systems. Additionally, the influence of aberrations occurring in real systems on the signal intensity is discussed. Having established the optical design and its underlying influencing parameters, the next part of the thesis examines the realisation of the IRAS system. Details of the mechanical design and essential functions are explained. Next, the performance of the system is demonstrated. In the end, the crucial parameters are concluded, and an outlook for potential improvements and applications of the system is given.

CHAPTER 2

IR SPECTROSCOPY

Infrared spectroscopy is a non-destructive technique that can be applied in various conditions, reaching from very defined environments in ultra-high vacuum (UHV) to realistic conditions. This makes it a widely used technique in industry but also fundamental research. One of the most common forms of IR spectroscopy is transmission spectroscopy. Here, the sample is probed by shining IR light through. Other variants of this technique using IR light for probing are attenuated total reflection (ATR) spectroscopy, diffuse reflectance infrared Fourier transform spectroscopy (DRIFTS) and infrared reflection absorption spectroscopy (IRAS). The latter technique is discussed in more detail in the following. All the mentioned techniques are based on the same principles for detecting vibrations of molecules. Parts of the chapter can be found in [34].

2.1 Molecular Vibrations

The principle of IR spectroscopy is based on the interaction between electromagnetic radiation and molecules. When the energy of a photon $E_{\text{photon}} = h\nu$, where h is Planck's constant and ν the frequency of the light, matches the vibrational and rotational quantised transition energies of the molecule, the photon gets absorbed by the molecule. This absorbance is very characteristic in its frequency and allows for the determination of the type of molecule based on the position of the peaks in the spectrum.

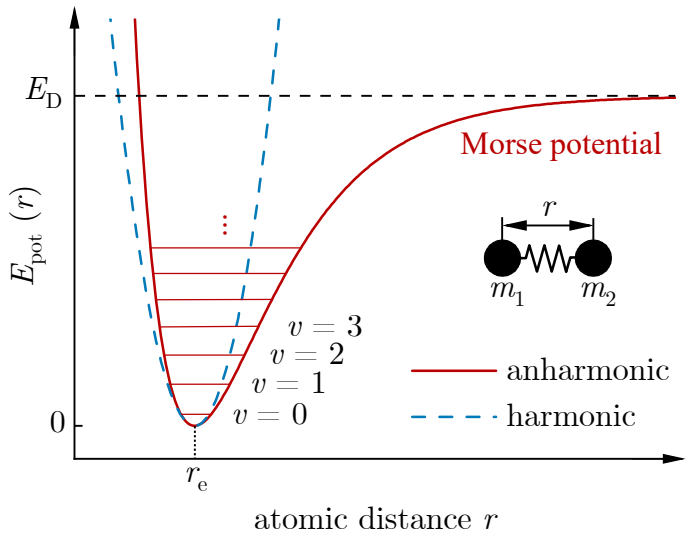

Figure 2.1: Potential energy $E_{pot}(r)$ of a vibrating diatomic molecule (atoms with m_1 and m_2) as function of the atomic distance r. A harmonic oscillator (blue dashed line) and an anharmonic oscillator (Morse potential, red solid line) are shown. The red horizontal lines schematically indicate the vibrational energy levels. r_e marks the equilibrium distance of the two atoms in the molecule. E_D is the dissociation energy of the molecule.

The number of vibrational modes for a molecule with N_a atoms is $3N_a - 6$. For a linear molecule, this reduces to $3N_a - 5$ [35]. Molecules can also be seen as clusters of positive (atomic nuclei) and negative charges (electrons). These charges can be distributed so that the centre of charge of the positive charges does not overlap with the centre of charge of the negative charges, resulting in an electrical dipole moment $\vec{p}$, further only called dipole moment. Molecules can have such a dipole moment by nature, or it can be induced by vibration when the atoms of the molecule change their position. To detect molecular vibrations with IR spectroscopy, the dipole moment $\vec{p}$ has to change during vibration; then the vibrational mode is IR active.

A simple way to describe the molecular vibrations is possible with the example of a diatomic molecule; two masses m_1 and m_2 are connected through a massless spring with the spring constant k following Hooke's law. Such a system can be described with the potential of the harmonic oscillator (shown as the blue dashed curve in Fig. 2.1). Solving the stationary Schrödinger equation for the harmonic potential leads to quantised energy states

$$E(v) = \hbar\omega\left(v + \frac{1}{2}\right), \tag{2.1}$$

where v is the vibrational quantum number, $\hbar$ the reduced Planck constant. The angular frequency $\omega = \sqrt{k/\mu}$ of the oscillator can be calculated with the reduce mass

$$\mu = \frac{m_1 m_2}{m_1 + m_2} \tag{2.2}$$

and characterises the fundamental angular frequency of the molecular vibration. In IR spectroscopy, the wavenumber $\tilde{\nu} = 1/\lambda$ expressed in cm^{-1} is commonly used to specify the vibrational frequency where λ is the wavelength of the light. For the harmonic oscillator

$$\tilde{\nu} = \frac{1}{2\pi c}\sqrt{\frac{k}{\mu}}, \tag{2.3}$$

which allows an estimation of the vibrational frequency based on the reduced molecule mass (μ, in g), the bond strength (analogue to k, in mN/m) and the speed of light (c, in cm/s). Molecules with heavier atoms (high μ) or weak bonds (small k) vibrate with lower wavenumbers. In contrast, peaks in the spectrum originating from stronger bound or lighter molecules appear at higher wavenumbers. For small energies, the harmonic oscillator is a valid approximation; however, higher energies are better described with the Morse potential (the red curve in Fig. 2.1). This potential shows a higher repulsion of the atoms for atomic distances smaller than the equilibrium distance r_e and molecular dissociation at E_D for $r \to \infty$. In contrast to the harmonic oscillator, the vibrational energy levels [36]

$$E(v) = \hbar\omega\left(v + \frac{1}{2}\right) - \frac{\hbar^2\omega^2}{4E_\mathrm{D}}\left(v + \frac{1}{2}\right)^2 \tag{2.4}$$

are not equally spaced, are finite in number and the energy difference ΔE between the neighbouring levels decreases with increasing vibrational quantum number v.

In most cases, the energy which is necessary to excite the molecule from the vibrational ground state with $v = 0$ into the first excited state with $v = 1$ corresponds to the energy of photons in the mid-infrared (MIR) region reaching from $400\,\mathrm{cm}^{-1}$ to $4000\,\mathrm{cm}^{-1}$ ($25\,\mu\mathrm{m}$ to $2.5\,\mu\mathrm{m}$) [35]. The full infrared range is completed by the far-infrared (FIR) ranging from $10\,\mathrm{cm}^{-1}$ to $400\,\mathrm{cm}^{-1}$ ($1000\,\mu\mathrm{m}$ to $25\,\mu\mathrm{m}$) and the near-infrared (NIR) extending from $4000\,\mathrm{cm}^{-1}$ to $12500\,\mathrm{cm}^{-1}$ ($2.5\,\mu\mathrm{m}$ to $0.8\,\mu\mathrm{m}$) [37].

2.2 Fourier Transform Infrared Spectrometer

Nowadays, Fourier transform infrared (FTIR) spectrometers are commonly used to record infrared spectra due to their advantages over grating spectrometers. These advantages include the simultaneous measurement of all wavelengths (Fellgett's or multiplex advantage) and the throughput advantage, also called Jacquinot's advantage [35].

The key component of an FTIR is the interferometer. A Michelson-type interferometer is commonly used, as shown in Figure 2.2. The beam splitter splits a parallel light beam into two partial beams with equal intensity. One beam reflects off a fixed mirror, and the second beam off a moving mirror. The two beams are then recombined after the beam splitter and interfere. This interference beam is used for probing. The

position of the moving mirror is determined by detecting the intensity zero crossings of an interfered helium-neon (HeNe) laser beam, which passes through the same interferometer as the IR beam. Therefore, the mirror speed f_M of the moving mirror is usually specified in kHz and can be recalculated to the mechanical speed of the mirror according to

$$v_M = \frac{1}{2} f_M \lambda_{HeNe}. \tag{2.5}$$

With a HeNe laser wavelength of $\lambda_{HeNe} = 632.816\,nm$, a mirror speed of $f_M = 60\,kHz$ is equivalent to a mechanical speed of the mirror of $v_M = 19\,mm/s$. The precise detection of the moving mirror position provides a high wavenumber accuracy and is known as Connes advantage [35]. A heated silicon carbide rod (about 1200 to 1400 K), the glow bar, is typically used as an MIR source, emitting a broadband IR spectrum. The emitted light is collected by a source mirror, focused onto the Jacquinot stop (J-stop), and then transmitted to the collimation mirror (CM), creating a parallel light beam for the interferometer. After the interferometer, the light is focused onto the sample and further guided and focused on the detector. Light emitted from a real extended source always results in a divergent light beam with an estimated divergence angle (see Figure 2.2)

$$\alpha = \arctan\left(\frac{d_J}{2 \cdot f_{CM}}\right), \tag{2.6}$$

where d_J is the J-stop diameter and f_{CM} the focal length of the collimation mirror. The divergence of the light beam in the interferometer and the maximum measurement wavenumber $\tilde{\nu}_{max}$ limit the best achievable resolution [38] to

$$\Delta\tilde{\nu}_{limit} = \alpha^2 \cdot \tilde{\nu}_{max} = \arctan^2\left(\frac{d_J}{2 \cdot f_{CM}}\right) \cdot \tilde{\nu}_{max}, \tag{2.7}$$

with α in units of rad. Equation 2.7 is valid when the J-stop is the defining field stop. Generally, the field stop is an aperture in an optical system, which defines the maximal possible object size. For high resolution measurements, e.g. $0.1\,cm^{-1}$ the image of the glowbar on the detector is restricted by the J-stop and smaller than the detector element. For low resolution measurements, e.g. $\Delta\tilde{\nu} = 4\,cm^{-1}$, the object size defining aperture is often the detector element. In this case, d_J in equation 2.7 has to be replaced by an effective J-stop diameter (based on paraxial concepts)

$$d_{J,effective} = \frac{d_{limit}}{\beta_J}, \tag{2.8}$$

where β_J is the reproduction scale [39] of the optical system between the J-stop and the detector and y_{limit} is the size of the detector element[1]. If an optical element other than the detector defines the image size, e.g. the sample, then the reproduction scale

[1]The reproduction scale of the presented IRAS system combinded with the FTIR Bruker Vertex 80v (between J-stop and detector) is $\beta_{total} = 0.31$ (see also Section 3.1.2).

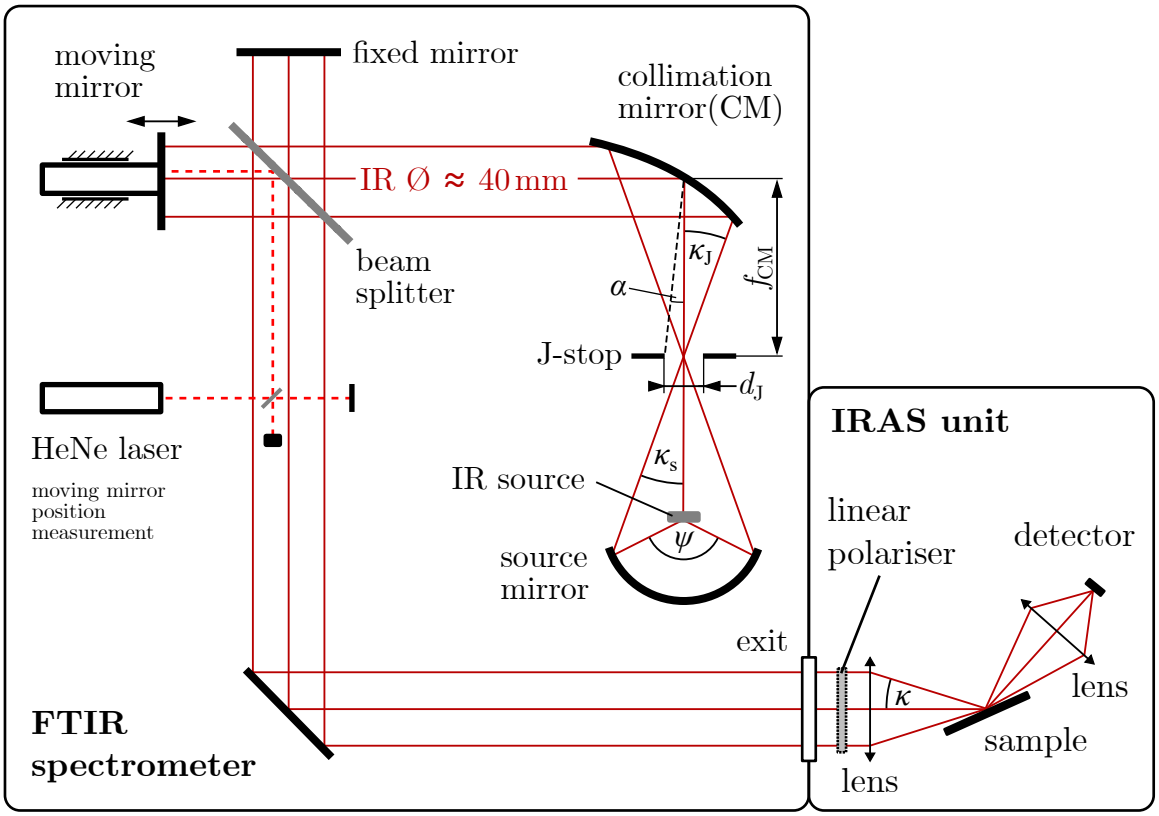

Figure 2.2: Schematic representation of an FTIR spectrometer and an external IRAS unit. The main optical components of the spectrometer are shown: the IR source with source optics, the Michelson interferometer and a helium-neon (HeNe) laser to determine the velocity and position of the moving mirror. The primary components of the IRAS unit are a linear polariser, focusing and collection optics (e.g. lens or mirror), the sample and a detector.

up to the sample and the sample size have to be used. The reproduction scale can be calculated by the ratio of the image distance to the object distance [39], valid for paraxial optics and the same media before and after the optical element.

During a measurement, the FTIR spectrometer records the intensity variation on the detector with respect to the position of the moving mirror. This leads to a characteristic interferogram with a central maximum. The maximum splits the interferogram into two halves; one half is called one scan. The spectrometer software OPUS [40] outputs the intensity of the central maximum as an ADC-count, equivalent to the intensity (see appendix A.4). On the measured interferogram, a Fast Fourier Transform (FFT) is applied and results in an intensity spectrum in respect of the wavenumber $\tilde{\nu}$.

To perform IRAS, the parallel beam from the spectrometer is directed to the sample, focussed and used to probe a sample surface as schematically shown in Figure 2.2.

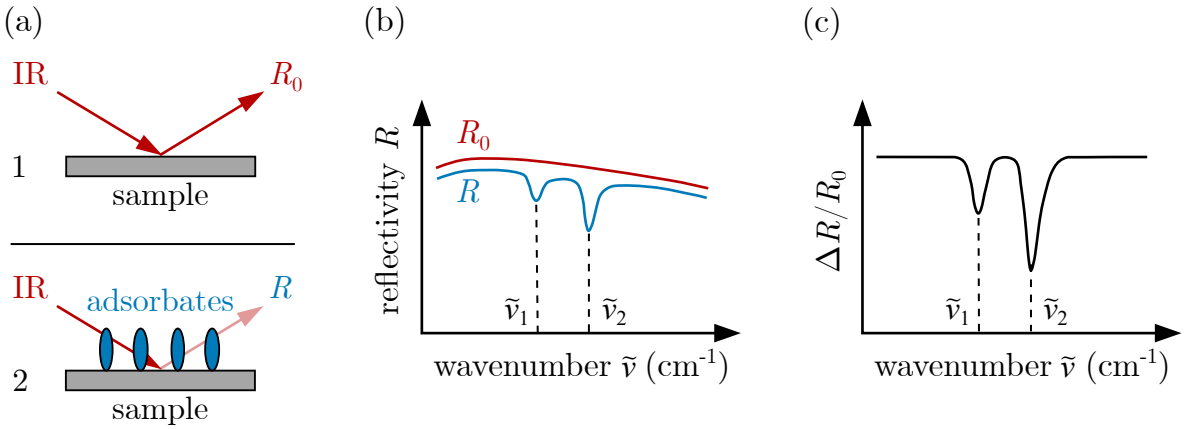

Figure 2.3: Schematic drawing of the measurement steps common for IRAS. (a1) depicts IRAS on the clean sample where the reference spectrum R_0 is acquired. (a2) shows IRAS on the adsorbate-covered where the sample spectrum R is measured. (b) visualises schematic single beam spectra acquired on a clean sample (R_0) and an adsorbate-covered sample (R). To enhance clarity, R shows an offset from R_0. In (c), the normalised reflectivity difference ($\Delta R/R_0$) spectrum is depicted.

Performing IRAS requires additional components like a linear polariser and focussing optics before the sample and the detector.

2.3 Infrared Reflection Absorption Spectroscopy

Infrared reflection absorption spectroscopy (IRAS, IRRAS), also known as external reflection spectroscopy (ERS) or reflection absorption spectroscopy (RAIRS), is a surface-sensitive measurement technique, making it an ideal tool for investigations of adsorbed molecules on surfaces. With IRAS, only vibrational modes are probed because the adsorption of the molecule on the surface usually prevents rotational modes.

The basic principle of IRAS is to reflect IR light once off a sample and detect the reflected intensity, schematically shown in Figure 2.3(a). The resulting spectrum is called the single beam spectrum and contains the information of how much intensity is reflected at a specific wavenumber $\tilde{\nu}$ [see Figure 2.3(b)]. Adsorbates on the sample surface absorb a particular part of the incoming IR light. Peak positions in the spectrum can then be related to the molecule type and how it is bonded to the surface. Furthermore, it also contains information about the surroundings of the molecule.

Optical components in the path contribute to the absorption of the IR light. This leads to additional features in the single beam spectrum besides the absorbance peaks caused by the molecules adsorbed on the sample surface. Measuring only one single beam spectrum is therefore insufficient to identify the features originating from adsorbed molecules. Hence, IRAS has to be performed in a two-step process. The first spectrum is measured by reflecting the IR beam off the sample before adsorbing molecules (see

Fig. 2.3 (a1)). The resulting single beam spectrum (the red curve in see Fig. 2.3 (b)) is commonly referred to as reference spectrum R_0. In a second step, the sample with the adsorbed molecules is measured (see Fig. 2.3 (a2)), leading to a second single beam spectrum (the blue curve in Fig. 2.3 (b)). This spectrum is called the sample spectrum R and has additional absorbance peaks compared to the reference spectrum R_0. These two spectra are then used to calculate the normalised reflectivity difference

$$\frac{\Delta R}{R_0} = \frac{R - R_0}{R_0}, \tag{2.9}$$

which is schematically visualised in Fig. 2.3(c) and used throughout this work. Sometimes also the absorbance $A = -\log_{10}(R/R_0)$ can be found in literature. Note that the peak orientation in absorbance spectra is reversed compared to $\Delta R/R_0$ spectra.

2.4 Theoretical Background for IRAS

The light reflection off a surface is the fundamental concept behind IRAS. Therefore, it is essential to understand the interaction of light with both the clean surface and the adsorbate-covered surface. The Fresnel equations provide the fundamental theoretical concept for describing the reflection of light from a clean surface. Describing the reflection off an adsorbate-covered surface requires a more elaborate approach. This can be done by the introduction of a thin layer characterised by a dielectric function ϵ and an effective thickness d representing the adsorbates on the surface [41–44] (three-layer model) or the use of a 2D surface polarisability [45]. This work uses the latter method to model the adsorbate-covered surface. It is important to consider not only the reflection from the surface but also the electric field on the surface and its incidence angle dependence as it gives insight into the optimum conditions for the light-adsorbate interaction. Parts of the following chapter can be found in [34].

2.4.1 Fresnel Reflectivity

The Fresnel equations were developed by the French physicist Augustin-Jean Fresnel in the early 19th century to explain the behaviour of light at the interface between different media. These equations represent a fundamental tool in optics and describe the reflection and transmission of light at the boundary between two media with different complex refractive indices

$$\hat{n} = n + ik = \sqrt{\epsilon(\omega)}. \tag{2.10}$$

The real part of the refractive index, denoted by n, describes the ratio between the speed of light in in vacuum, c_0, and the material, c_m. The extinction coefficient k, provides information about the damping of the electromagnetic wave in the medium. Another equivalent quantity to describe the interaction of an electromagnetic field with matter is the complex dielectric function

$$\epsilon(\omega) = \epsilon'(\omega) + i\epsilon''(\omega). \tag{2.11}$$

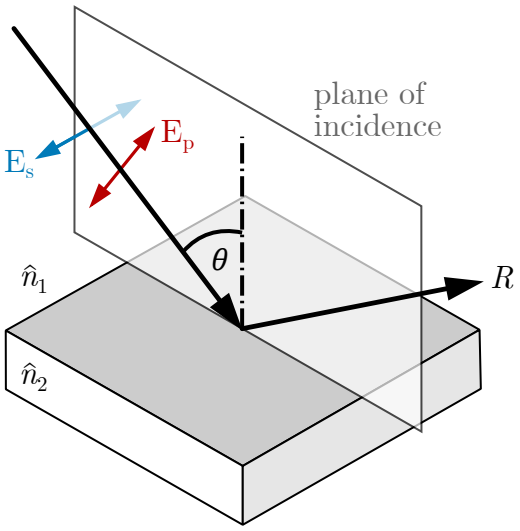

Figure 2.4: Schematic illustration of the reflection on a surface for linear polarised light. The general reflection case is described by the incidence angle θ and the refractive indices of the two neighbouring media $\hat{n}_1$ and $\hat{n}_2$ (equivalent to ϵ_1 and ϵ_2). In the case of p-polarised light, the E-field oscillates only in the plane of incidence (E_p in red). Light oscillating only perpendicular to the plane of incidence is called s-polarised light (E_s in blue).

Both quantities, the dielectric function ϵ and the refractive index $\hat{n}$ are linked according to equation 2.10. Therefore, the real (ϵ') and imaginary part (ϵ'') of the dielectric function can be expressed in terms of the real refractive index n and the extinction coefficient k:

$$\epsilon' = n^2 - k^2 \text{ and} \tag{2.12}$$

$$\epsilon'' = 2nk. \tag{2.13}$$

Figure 2.4 shows a schematic illustration of the general case of reflection. The incidence angle θ is measured with respect to the surface normal. To describe the reflection, splitting the light in an s- and p-component is common. For s-polarised light, the electric field (E-field) oscillates only perpendicular to the plane of incidence. For p polarisation, the incoming E-field oscillates only parallel to the incidence plane.

The Fresnel equations provide amplitude coefficients of the reflected (r) and transmitted (t) light, describing their amplitude and phase shift in relation to the incoming light. The coefficients r and t depend on the angle of incidence θ, polarisation state (s or p polarisation), and the refractive indices $\hat{n}_\mathrm{i}$ of the media involved. In the following, only the case of reflection is considered, as this is relevant for IRAS. For the calcula-

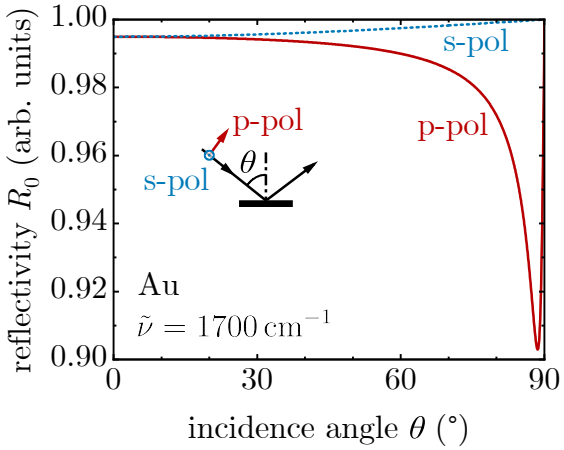

Figure 2.5: Calculated reflectivity of gold at $\tilde{\nu} = 1700\,\mathrm{cm}^{-1}$. The plot shows the reflectivity for s-polarised light (blue, dotted curve) and p-polarised light (red, solid curve) as a function of the incidence angle θ. The refractive index of Au is $\hat{n}_{\mathrm{Au}} = 2.06 + 40.36\,i$ [46, 47].

tions in this work, Fresnel equations in the form given by Langreth [45] were used. The complex amplitude coefficients for reflection of s-polarised light

$$r_{0,\mathrm{s}} = \frac{\cot(\theta) - \sqrt{\epsilon \csc^2(\theta) - 1}}{\cot(\theta) + \sqrt{\epsilon \csc^2(\theta) - 1}} \tag{2.14}$$

and p-polarised light

$$r_{0,\mathrm{p}} = \frac{\epsilon \cot(\theta) - \sqrt{\epsilon \csc^2(\theta) - 1}}{\epsilon \cot(\theta) + \sqrt{\epsilon \csc^2(\theta) - 1}} \tag{2.15}$$

describe the reflection on a clean surface, as the subscript zero indicates. Here, the dielectric function ϵ_1 (equivalent to $\hat{n}_1$ in Fig. 2.4) was set to unity (i.e., assuming vacuum), and the properties of the substrate are described with ϵ (corresponding to $\hat{n}_2$ in Fig. 2.4). ϵ, $r_{0,\mathrm{s}}$ and $r_{0,\mathrm{p}}$ are complex numbers. The reflectivity

$$R = |r|^2 \tag{2.16}$$

describes the fraction of incident light that is reflected at the interface.

Figure 2.5 shows the reflectivity of a gold surface for s- and p-polarised light with a wavenumber $\tilde{\nu} = 1700\,\mathrm{cm}^{-1}$ ($\lambda = 5.9\,\mu\mathrm{m}$), calculated using equations 2.14 to 2.16. The s-polarised reflectivity $R_{0,\mathrm{s}}$ is close to unity for all angles of incidence θ and is one at $\theta = 90°$. However, the reflectivity for p polarisation has a minimum of $R_{0,\mathrm{p}} \approx 0.9$ at very grazing angles (pseudo-Brester angle). Despite this, the reflectivity of gold in the MIR range is excellent.

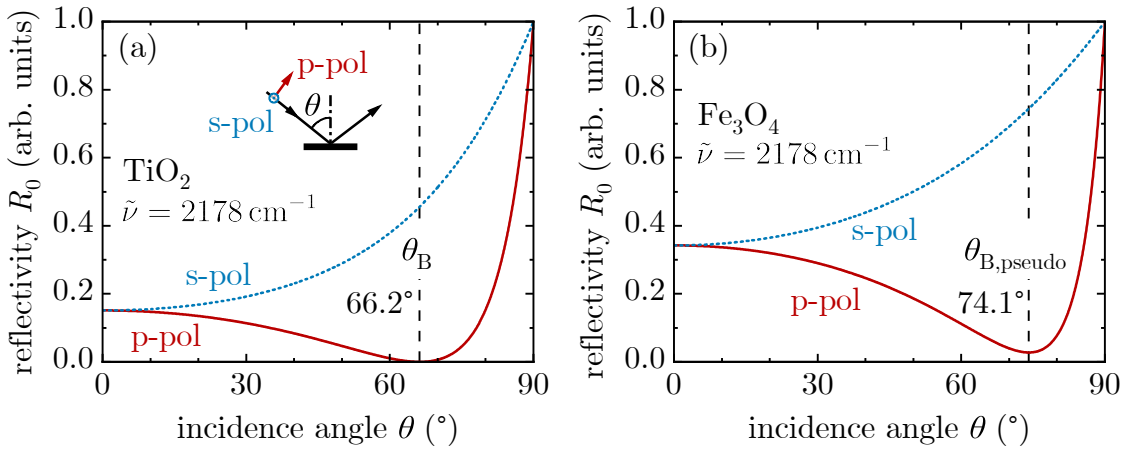

Figure 2.6: Calculated Fresnel reflectivity on two non-metallic substrates, TiO_2 and Fe_3O_4. The reflectivity of s-polarised light (blue, dotted curve) and p-polarised light (red, solid curve) is calculated as a function of the incidence angle θ at $\tilde{\nu} = 2178\,\mathrm{cm}^{-1}$. (a) shows the reflectivity of TiO_2 with a refractive index of $\hat{n}_{TiO_2} = 2.27 + 0.002\,i$ [46, 49] and the Brewster angle θ_B (dashed, vertical line); adapted from [34]. (b) depicts the reflectivity of s- and p-polarised light of Fe_3O_4 with a refractive index of $\hat{n}_{Fe_3O_4} = 3.33 + 1.23\,i$ [46, 50] and the pseudo-Brewster angle $\theta_{B,pseudo}$ (dashed, vertical line).

In contrast to metals, non-metallic substrates exhibit a different behaviour, with lower overall reflectivity in the mid-infrared (MIR) range and the appearance of a reflectivity minimum of zero or close to zero. Figure 2.6 shows the reflectivity of two such materials, i.e., TiO_2 and Fe_3O_4. By comparing these materials to gold in Figure 2.5, one can see a decreased reflectivity at all incidence angles except 90°, especially for p-polarisation. The reflectivity exceeds 0.8 only at very grazing incidence angles. At the Brewster angle

$$\theta_B = \arctan\left(\frac{n_2}{n_1}\right), \tag{2.17}$$

shown in Figure 2.6(a), zero reflection appears for p polarisation and dielectric materials where the extinction coefficient is negligibly small or zero. At θ_B, for p polarisation, the reflected and transmitted beams are at an angle of 90° to each other, and just s-polarised radiation is reflected. For media with a non-zero extinction coefficient k, the reflectivity for p-polarised light exhibits only a minimum at the so-called pseudo-Brewster angle $\theta_{B,pseudo}$ [see Figure 2.6(b)]. Beyond the Brewster angle, the reflectivity for p-polarisation exhibits a slow increase.

On birefringent materials, e.g. TiO_2, the simple definition of θ_B according to equation 2.17 is not valid [48]. Depending on the crystal orientation of the sample, variations in the position of the Brewster angle compared to an isotropic material occur. The birefringent character of TiO_2 is neglected for all the calculations shown in this thesis.

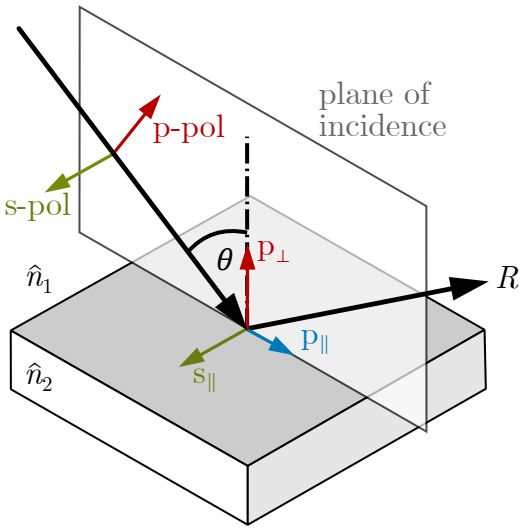

Figure 2.7: Splitting of the linear polarised light components on the surface. The electric field of p-polarised light (parallel to the incidence plane) can be split into components parallel ($p_\parallel$) and perpendicular ($p_\perp$) to the surface. The s-polarised light has the electric field parallel to the surface ($s_\parallel$) but perpendicular to the incidence plane.

2.4.2 Reflectivity with Surface-Adsorbates

When adsorbates influence the reflectivity of the surface, it is helpful to split the electric field of the p-polarised component into two parts: one perpendicular to the surface ($p_\perp$) and one parallel to the surface ($p_\parallel$), as shown in Figure 2.7. S-polarisation has only a parallel component ($s_\parallel$) and is oriented perpendicular to the incidence plane. Adsorbates with dipole moments parallel to the surface, and perpendicular to the plane of incidence can only be detected with s-polarisation. Dipole moments oriented in the light incidence plane are detected by p-polarisation. When an adsorbate dipole moment exhibits an angle to the plane of incidence and the surface, all light polarisations contribute to the signal.

As stated at the beginning of section 2.4, modified Fresnel equations are required to describe the impact of an adsorbate on surface reflectivity. This thesis uses Fresnel-like equations presented by Langreth [45]. These equations are derived by introducing surface polarisability to calculate the surface reflectivity for s-polarised light and p-polarised light. They are only valid for low adsorbate coverages with film thicknesses d much smaller than the wavelength λ_d of the light in the film ($d \ll \lambda_d$). For example, the dimensions of small molecules are less than 1 nm, while the MIR range extends from 2.5 µm to 25 µm [35]. By combining the equations formulated by Langreth [45] with the Lorentzian oscillator in reference [51], one can calculate the reflection amplitude coefficients

$$r_{s,\parallel} = \frac{\cot(\theta) - \sqrt{\epsilon \csc^2(\theta) - 1} + 8\,i\,\pi^2 N \alpha_{s,\parallel}\,\tilde{\nu}\,\csc(\theta)}{\cot(\theta) + \sqrt{\epsilon \csc^2(\theta) - 1} - 8\,i\,\pi^2 N \alpha_{s,\parallel}\,\tilde{\nu}\,\csc(\theta)}, \tag{2.18}$$

$$r_{p,\parallel} = \frac{8\,\pi^2 N \alpha_{p,\parallel}\,\tilde{\nu}\,\cos(\theta)\sqrt{\epsilon \csc^2(\theta) - 1} - i\left(\sqrt{\epsilon \csc^2(\theta) - 1} - \epsilon \cot(\theta)\right)}{8\,\pi^2 N \alpha_{p,\parallel}\,\tilde{\nu}\,\cos(\theta)\sqrt{\epsilon \csc^2(\theta) - 1} + i\left(\sqrt{\epsilon \csc^2(\theta) - 1} + \epsilon \cot(\theta)\right)}, \tag{2.19}$$

$$r_{p,\perp} = \frac{\epsilon \cot(\theta) - \sqrt{\epsilon \csc^2(\theta) - 1} + 8\,i\,\pi^2 N \alpha_{p,\perp}\,\epsilon\,\tilde{\nu}\sin(\theta)}{\epsilon \cot(\theta) + \sqrt{\epsilon \csc^2(\theta) - 1} - 8\,i\,\pi^2 N \alpha_{p,\perp}\,\epsilon\,\tilde{\nu}\sin(\theta)} \tag{2.20}$$

for s-and p-polarisation and the different orientations of the electric field components on the surface ($\parallel, \perp$ as shown in Figure 2.7). Again, θ defines the incidence angle, ϵ is the dielectric constant of the substrate where the light is reflected on (corresponding to $\hat{n}_2$ in Figure 2.7), N is the density of the surface adsorbates (per area), $\tilde{\nu}$ is the wavenumber and the polarisability [51] is

$$\alpha_{i,j}(\tilde{\nu}) = \alpha_e + \frac{\alpha_v}{1 + (\frac{\tilde{\nu}}{\tilde{\nu}_0})(\frac{\tilde{\nu}}{\tilde{\nu}_0} + i\frac{\gamma}{\tilde{\nu}_0})} \tag{2.21}$$

in volume units. Here, α_e defines the static electronic polarisability and α_v the vibrational polarisability. $\tilde{\nu}$ is the wavenumber, $\tilde{\nu}_0$ is the resonance wavenumber and γ is the line width of the oscillator. Both quantities $\tilde{\nu}_0$ and γ are expressed in wavenumber units.

The reflectivities for the adsorbate-covered surface can be calculated with the equations 2.18 to 2.21 and equation 2.16, resulting in three cases: $R_{s,\parallel}$, $R_{p,\parallel}$, $R_{p,\perp}$. The first subscript denotes the polarisation, and the second subscript relates to dipole moment orientation. In combination with the reflectivities of the clean surface $R_{0,s}$ and $R_{0,p}$, it is possible to calculate the normalised reflectivity difference intensity $\Delta R/R_0$ as a function of the incidence angle θ according to equation 2.9. $\Delta R/R_0$ calculated at the resonance frequency ($\tilde{\nu} = \tilde{\nu}_0$) is a measure for the peak height (signal intensity) expected at a certain incidence angle θ. Fixing the incidence angle and varying the wavenumber $\tilde{\nu}$ allows to calculate the peak shape [34, 38]. Because the peak height is equivalent to the normalised signal intensity, both expressions will be used throughout this work. To improve readability, the term normalised is sometimes omitted in the following.

For the calculations of $\Delta R/R_0$ shown in this thesis, the density of adsorbates on the surface $N = 5.2 \times 10^{14}\,\mathrm{cm}^{-2}$ was taken from reference [27] and represents the coverage of one monolayer (ML) CO on the $TiO_2(110)$ surface where one CO is adsorbed at each Ti_{5c} site. The line width $\gamma = 6\,\mathrm{cm}^{-1}$ was evaluated from the spectrum shown in Figure 5.2(b) where one monolayer CO on $TiO_2(110)$ was measured with $4\,\mathrm{cm}^{-1}$ resolution. The

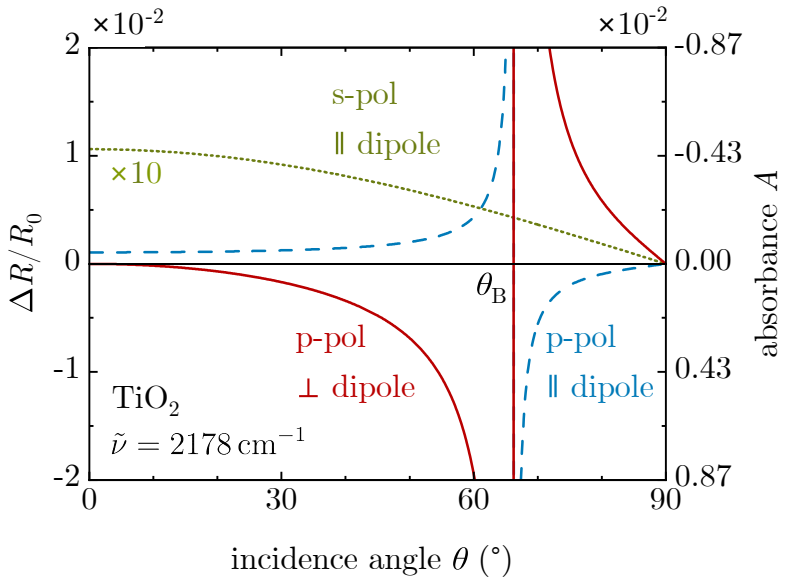

Figure 2.8: Calculated normalised reflectivity difference for TiO_2 with an adsorbate at $\tilde{\nu} = \tilde{\nu}_0 = 2178\,\mathrm{cm}^{-1}$. Three cases are presented: p-polarised light with the dipole moment perpendicular to the surface oriented (red, solid line), p-polarised light with the dipole moment parallel to the surface in the plane of incidence (blue, dashed curve), and s polarisation interacting with the dipole moment normal to the incidence plane (green, dotted line). The curve for s polarisation is multiplied by 10 to enhance clarity, and the Brewster angle θ_B is marked. The calculation parameters are defined in this section. The left y-axis represents the normalised reflectivity difference $\Delta R/R_0$ and the right y-axis the absorption.

static electronic polarisability α_e was assumed to be zero, and $\alpha_v = 3.4 \times 10^{-26}\,\mathrm{cm}^3$ resulted from the preliminary fit procedure shown and explained in more detail in Appendix A.2. Furthermore, $\tilde{\nu}_0 = \tilde{\nu}$, $\hat{n}_{TiO_2} = 2.27 + 0.002\,i$ ($\epsilon_{TiO_2} = 5.16 + 0.01\,i$) [46, 49] and $\hat{n}_{Fe_3O_4} = 3.33 + 1.23\,i$ ($\epsilon_{Fe_3O_4} = 9.54 + 8.18\,i$) [46, 50] were used as input parameters for the calculations.

Figure 2.8 shows the incidence angle dependent normalised reflectivity difference $\Delta R/R_0$ on TiO_2 covered with an adsorbate for s and p polarisation, considering dipole moment orientations in the three main directions, resulting in three curves for $s_\parallel$, $p_\parallel$, and $p_\perp$ as depicted in Figure 2.7. TiO_2 represents an ideal dielectric material with a negligible extinction coefficient k. The calculation was performed for a wavenumber $\tilde{\nu}$ of $2178\,\mathrm{cm}^{-1}$, close to the stretching frequency of CO on the $TiO_2(110)$ surface [27]. At 0° incidence angle, s polarisation with a parallel dipole moment oriented perpendicular to the plane of incidence (green, dotted line) and p polarisation with a parallel dipole moment oriented parallel to the incidence plane (blue, dashed line) exhibit identical values. Here, both polarisation components parallel to the surface are equivalent, and for p polarisation, the E-field perpendicular to the surface is zero (see also Figure 2.11). The $\Delta R/R_0$ signal for s-polarised light (multiplied by 20 in the plot) decreases with increasing incidence angle θ until $\theta = 90°$, where it becomes zero. The adsorbate enhances the surface reflectivity for s polarisation at the adsorbate resonance frequency (negative absorbance) for the whole incidence angle range.

The p-polarised signals significantly increase or decrease at the Brewster angle (dipole moment orientation dependent), where a $1/x$-like behaviour of $\Delta R/R_0$ is observed. This singularity is caused by ΔR having a zero for order one and R_0 a zero of order two, as illustrated in Figure 2.6(a). At this specific angle, the signal changes its sign, a phenomenon known as band inversion [52–55]. For p polarisation and incidence angles below the Brewster angle ($\theta < \theta_B$), dipole moments perpendicularly oriented to the surface lead to a decrease in reflectivity and a negative signal in the $\Delta R/R_0$ spectrum, while dipole moments that are oriented parallel result in positive signals and an increase in surface reflectivity. Incidence angles higher than θ_B ($\theta > \theta_B$) lead to positive signals for perpendicular dipole moments and negative signals for parallel dipole moments. At $\theta = 90°$, $\Delta R/R_0$ approaches zero for all three cases ($s_\parallel$, $p_\parallel$ and $p_\perp$). The signal intensity from parallel dipole moments is approximately one order of magnitude smaller than that of dipole moments normal to the surface. The expected signal intensities are similar only at low incidence angles.

Figure 2.9 illustrates the calculation of the normalised reflectivity difference $\Delta R/R_0$ calculated at the resonance wavenumber on Fe_3O_4. It is a non-metallic substrate exhibiting a finite extinction coefficient k. The calculation was performed with the same adsorbate as used for TiO_2 (Figure 2.8). The trend of band inversion around the pseudo-Brewster angle (in the case of TiO_2, the Brewster angle) for p-polarised light remains the same, with smaller signal intensities at up to incidence angles of about 78° and similar peak heights for $\theta > 78°$. Also, s polarisation (multiplied by 20 in the plot) remains similar to TiO_2, showing increasing reflectivity due to the adsorbate for all incidence

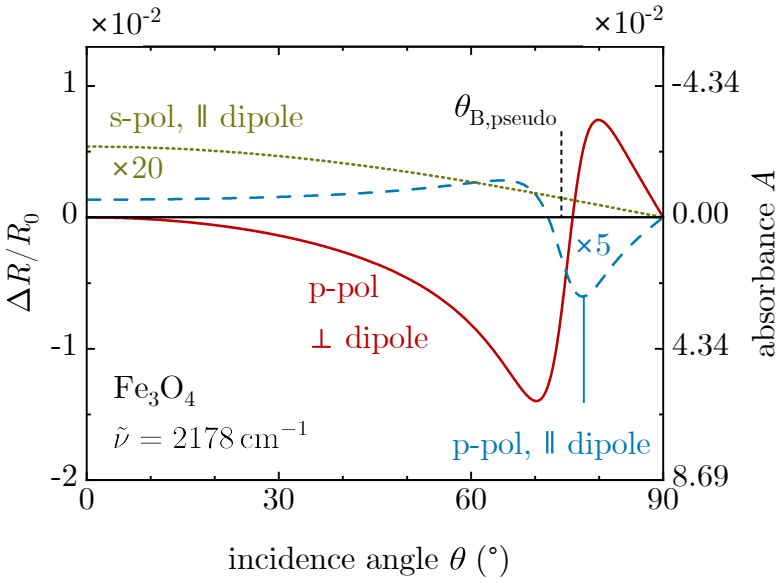

Figure 2.9: Calculated normalised reflectivity difference for Fe_3O_4 with an adsorbate at $\tilde{\nu} = \tilde{\nu}_0 = 2178\,\mathrm{cm}^{-1}$. Three cases are presented: p-polarised light with a dipole normal to the surface oriented (red, solid line), p-polarised light with an dipole moment parallel to the surface in the plane of incidence (blue, dashed curve), and s polarisation interacting with a parallel dipole moment perpendicular to the incidence plane (green, dotted line). The curve for s polarisation is multiplied by 20 to enhance clarity, and the pseudo-Brewster angle is marked (black, dashed line). The calculation parameters are defined in this section. The left y-axis represents the normalised reflectivity difference $\Delta R/R_0$and the right y-axis the absorption.

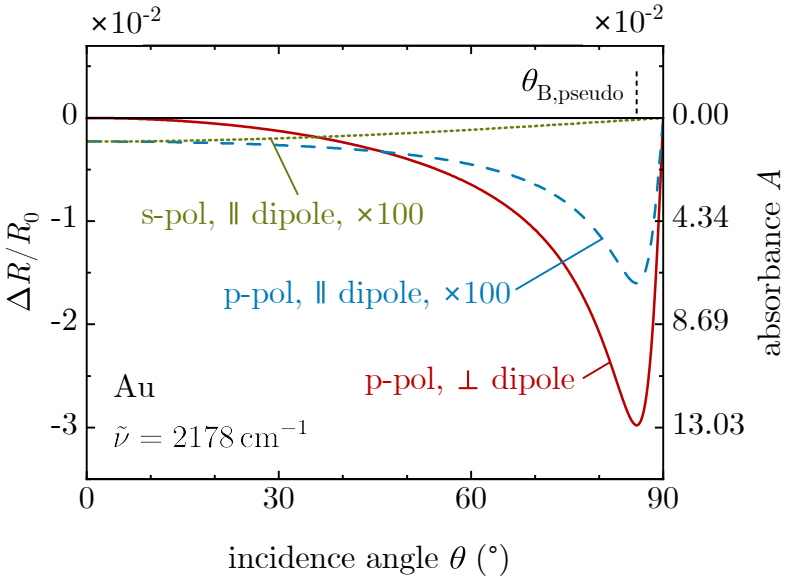

Figure 2.10: Normalised reflectivity difference $\Delta R/R_0$ for an adsorbate on Au ($\hat{n}_{\mathrm{Au}} = 0.92 + 13.780\,i$) [46, 56] at $\tilde{\nu} = 2178\,\mathrm{cm}^{-1}$. In red (solid line), p-polarisation with a dipole moment normal to the surface and in the incidence plane is shown. The blue (dashed) line depicts p-polarisation with a dipole parallel to the surface and in the incidence plane. The case of s-polarisation with a dipole parallel to the surface and perpendicular to the incidence plane is green (dotted). Both curves for the parallel dipole moments are multiplied by 100. The black (dashed) line indicates the pseudo-Brewster angle. The left y-axis represents the normalised reflectivity difference $\Delta R/R_0$and the right y-axis the absorption.

angles but lower signals than on TiO_2 by approximately a factor of four. For a parallel dipole moment, both polarisation components, s polarisation (green, dotted curve) and p polarisation (blue, dashed curve), show the same signal intensity at $\theta = 0°$.

On material with finite k, ΔR has a zero of order one, but R_0 only approaches a minimum as shown in Figure 2.6(b) at the pseudo-Brewster angle. Therefore, $\Delta R/R_0$ is finite for all incidence angles θ and exhibits a maximum and minimum close to the pseudo-Brewster angle, as illustrated in Figure 2.9. Measurements with p polarisation of signals originating from parallel dipole moments change sign at a slightly lower incidence angle of 72° than $\theta_{\mathrm{B,pseudo}}$ (74.1°), whereas signals from perpendicular dipole moments exhibit band inversion shortly after $\theta_{\mathrm{B,pseudo}}$ at 76.7°. In IRAS measurements of such materials, near the pseudo-Brewster angle, peaks have a Fano-line shape instead of a Lorentzian peak shape [34, 57] and asymmetric peaks for s polarisation are expected [34].

On metals, no band inversion occurs and the maximum signal intensity for p polarisation and a normal dipole occurs at very grazing incidence angles. Figure 2.10 shows the normalised reflectivity difference $\Delta R/R_0$ on gold with a refractive index of $\hat{n}_{\mathrm{Au}} = 0.92 + 13.780\,i$ ($\epsilon = -189.04 + 25.355\,i$) [46, 56]. The calculation was performed at

$\tilde{\nu} = \tilde{\nu}_0 = 2178\,\mathrm{cm}^{-1}$ with the same adsorbate parameters as used in the calculations shown in Figure 2.8 and 2.9. The expected signal intensities from parallel dipole moments are very small and are multiplied by 100 to make them visible in Figure 2.10. At very grazing angles, the calculation predicts signals in the order of 10^{-4} for p-polarisation and a dipole moment parallel to the surface and oriented along the IR light incidence plane. P-polarisation and a dipole moment oriented perpendicular to the surface shows the strongest signal where $\Delta R_p/R_{0,p}$ is in the order of 10^{-2}. Note that this calculation does not include any corrections and represents the ideal calculation.

2.4.3 Mean Square Electric Field on the Surface

When measuring IRAS, the adsorbed molecules interact with the electric field on the surface formed by the interference of the incident and reflected light. This interference results in a standing wave [6] with different electric field magnitudes with respect to the height z above the surface. Understanding the behaviour of the surface electric field provides an important insight into the strength of the interaction between the adsorbate and light. As the wavelength of infrared light in the MIR range is much larger than the dimensions of the adsorbed molecules (or layers), the electric field directly above the reflecting surface (at $z = 0$) can be investigated [6]. Previous studies present the behaviour of the mean square electric field on optical interfaces [13, 41, 58, 59]. In the following, the mean square electric field components $\langle E^2_{\mathrm{s},\parallel}\rangle$, $\langle E^2_{\mathrm{p},\parallel}\rangle$, and $\langle E^2_{\mathrm{p},\perp}\rangle$ on the surface are calculated following the equations presented in reference [58], using the complex amplitude coefficients of the reflectivity, specified in equations 2.18 to 2.20.

Figure 2.11 shows the mean square electric field for the electric field components in the three main directions, as shown in Figure 2.7. The calculation of the mean square electric fields assumes that the incident amplitudes of the mean square electric fields for s and p polarisation are equal to one. In frame (a) the mean square electric field is calculated for TiO_2 (the values are given in section 2.4.2). The maximum mean square electric field of the E-field components with s- and p-polarised light (blue and dark green), which are parallel to the surface occurs at normal incidence ($\theta = 0°$). As the incidence angle θ increases, the mean square electric field diminishes, reaching zero at $\theta = 90°$. Therefore, the optimal interaction between IR light and parallel dipole moments on the surface is at low incidence angles θ. For the perpendicular component of the surface electric field and p polarisation, the maximum light-adsorbate interaction is seen at $\theta \approx 75°$. However, at grazing and low incidence angles θ, this interaction decreases and is zero at $\theta = 0°$ and $\theta = 90°$. The maximum field normal to the surface is more than two times higher than that parallel to the surface. On Fe_3O_4 the mean square electric fields behave similarly as for TiO_2, with smaller values for the parallel oriented field components and higher values for the perpendicular field intensity. On average over the whole incidence angle range, $\langle E^2_{\mathrm{p},\parallel}\rangle$ is 2.2 times smaller, $\langle E^2_{\mathrm{p},\parallel}\rangle$ 1.6 times smaller and $\langle E^2_{\mathrm{p},\perp}\rangle$ 1.4 times higher (compared to TiO_2).

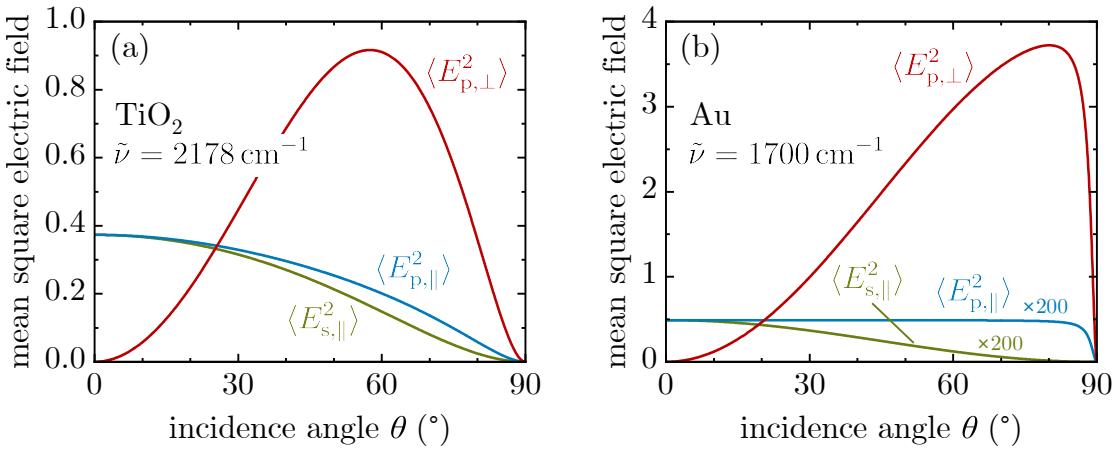

Figure 2.11: Surface electric field intensity directly on the surface. (a) shows the electric field intensities on a non-metallic surface of TiO_2 and (b) on the metallic surface of gold. The mean square electric field components on the surface directly at the interface are split up into the three major components: s-polarised light with the electric field parallel to the surface and perpendicular to the incidence plane $\langle E^2_{\mathrm{p},\parallel}\rangle$, the component of p-polarised light parallel to the surface in incidence plane $\langle E^2_{\mathrm{p},\parallel}\rangle$ and the component of p-polarised light perpendicular to the surface $\langle E^2_{\mathrm{p},\perp}\rangle$. The calculation parameters are defined in section 2.4.2.

This behaviour of the electric field components explains why IRAS on non-metallic substrates is sensitive to adsorbate dipole moment changes in all directions. Depending on the investigated system, this can lead to more complex spectra than on metals providing more information about the adsorbate orientation.

In the case of metals, e.g., gold shown in Figure 2.11(b), the perpendicular surface electric field $\langle E^2_{\mathrm{p},\perp}\rangle$ is enhanced. The maximum is located at very grazing angles and is about four times higher than the maximum on TiO_2. The mean square electric field for the parallel components, $\langle E^2_{\mathrm{s},\parallel}\rangle$ and $\langle E^2_{\mathrm{p},\parallel}\rangle$, are negligibly small [58]. A vanishing parallel surface electric field means no interaction with the a parallel dipole moment is possible. Thus, no signals are observed in the IRAS spectra. This can be directly related to the surface selection rules, which are only valid for IRAS measurements on metals [6, 13, 14]. A more descriptive explanation is often given by the formation of image dipoles, which cancel out the dipole change parallel to the surface of a vibrating molecule, while a dipole moment in normal direction is enhanced by the image dipole [15].

The dipole enhancement on metals with its strong light-adsorbate interaction for normal to the surface oriented dipole moments at grazing incidence angles (see Figure 2.11(b)) and the high reflectivity of these materials (see Figure 2.5) facilitate IRAS measurements with a high signal-to-noise ratio. This allows the routine detection of low adsorbate coverages. In contrast, non-metallic substrates exhibit weak light-adsorbate interaction with the maximum of the mean square electric field coinciding with the low

reflectivity of these substrates, leading to much lower signals, thus lower signal-to-noise ratio, more demanding measurements and longer measurement times.

2.4.4 Optimisation Parameters for Non-Metals

For optimising a measurement system for IRAS measurements on non-metallic substrates, two factors are essential: the normalised reflectivity difference $\Delta R/R_0$ and the reflectivity of the surface R_0. As mentioned above, the normalised reflectivity difference $\Delta R/R_0$ calculated at the resonance frequency of the adsorbate represents the expected peak height at a certain incidence angle θ. Figure 2.8 and 2.9 show band inversion for p polarisation at the Brewster or pseudo-Brewster angle, respectively, making these angles critical angles. The band inversion leads to positive and negative peak orientations in the spectrum, dependent on which side of the critical angle the light incidences onto the sample. Therefore, it is crucial to avoid measuring with an incidence angle range that overlaps the critical angle. The highest $\Delta R/R_0$ signals occur close to the critical angle. However, the reflectivity R_0 at this angle is very low or even zero (see Figure 2.6), leading to low throughput and high noise. This means that for optimum signal-to-noise ratio, some distance from the critical angle is recommended for p-polarised measurements. Note that the position of the Brewster angle or the pseudo-Brewster angle changes with the refractive index.

For s polarisation, maximum peak heights are predicted at incidence angles of $\theta = 0$. In IRAS measurements this is not feasible, requiring a non-zero angle θ to separate the incoming and outgoing beam. However, peak heights of s-polarised spectra benefit from incidence angles as low as possible. Figure 2.6 shows that the reflectivity has its optimum at very grazing angles. So, to reach optimised SNRs, it is necessary to balance the incidence angle leading to high peaks and good throughput.

Note that the calculations presented in this chapter describe the ideal case of reflection, where a perfectly parallel incidence beam reflects entirely off the surface. This representation provides a solid foundation for understanding the fundamental principles behind IRAS on non-metals. Still, it needs further expansion to reflect realistic conditions where additional effects change $\Delta R/R_0$. These effects are investigated in the following chapter. However, the main takeaway is that the incidence angles have to be wisely chosen (defines the peak height), and the Brewster angle or the pseudo-Brewster angle is a critical criterion for p-polarised IRAS. The peak height must also be balanced with the throughput defined by the reflectivity R_0 to reach optimum SNR.

2.4.5 Summary

Fourier transform infrared reflection absorption spectroscopy is a useful tool for investigating adsorbates on various substrates. By employing the Fresnel equations and considering surface polarisability, it is possible to calculate the normalised reflectivity difference $\Delta R/R_0$ with respect to the incident angle θ for thin films ($d << \lambda$). It corresponds to the signal intensity when $\Delta R/R_0$ is calculated at the resonance frequency

of the adsorbate. The most sensitive region for detecting adsorbates on non-metallic substrates coincides with low reflectivity, making IRAS challenging on these materials. Furthermore, IRAS on non-metallic substrates exhibits band inversion at the Brewster or pseudo-Brewster angle for p-polarised light. Consequently, it is essential to consider this critical angle when selecting the appropriate incident angles for IRAS measurements.

CHAPTER 3

DESIGN FRAMEWORK

In the process of designing a measurement system, crucial decisions are made that significantly impact the system performance even before the design is started. Some of these decisions can be changed later, some not. Therefore, identifying essential design parameters is crucial for building a solid design framework. This framework enables the system to be optimised. It helps to identify potential areas where compromises can be made without sacrificing too much performance, as boundary conditions often impose restrictions that cannot be escaped. Additionally, a solid design framework opens the possibility to estimate where future changes in a measurement system can improve performance.

The ability to achieve high signal-to-noise ratios (SNR) is crucial in designing an IRAS setup as it ensures the high sensitivity of the system. This facilitates measurements of low adsorbate coverages and short measurement times. To optimise the IRAS design, a thorough understanding of the underlying theoretical concepts, as discussed in section 2.4, is required. These concepts lead to important optimisation parameters, following from the surface reflectivity R_0 and the expected normalised signal $\Delta R/R_0$, all of which depend on the incidence angle θ and polarisation of the light. Based on these parameters, optimised signal-to-noise ratios can be achieved by increasing the throughput of the optical system and choosing the correct incidence angles which directly relate to signal intensities for the different measurement cases. Effects occurring in real optical systems alter the achievable signal intensities, which can be ascribed to effects such

as depolarisation of the light or divergence of the beam. A combination of the ideal theory with additional considerations originating from the real system leads to a robust design framework for the design of the optical system. Furthermore, selecting the right optical components, a spectrometer, and a detector with good noise performance and high sensitivity sets the foundation for a high-performance system.

Realising the design requires combining the solid design framework with existing boundary conditions to develop an IRAS system with maximised performance. Parts of the chapter can be found in [34].

3.1 Throughput Optimisation

Low noise is an important parameter to improve the measurement performance of an IRAS setup. There are several ways to achieve this, such as increasing the number of scans for spectrum acquisition, using components and electronics with good noise performance, and increasing the intensity through the optical system. The mechanic stability also influences the noise performance of the system as increasing this reduces the noise caused by environmental vibrations. Increasing the number of scans works without changing the optical system but results in longer measurement times. This also means that more adsorption or desorption occurs on the sample surface between the reference and sample spectrum or that the baseline changes, e.g. due to a temperature change.

A high throughput of the optical system leads to a high intensity on the detector and consequently good SNR. The basis of the system throughput is the optical design, which is difficult to change when the measurement system is operational. The source also has a major influence on the detected intensity as it defines the initial intensity of the system. Because the source can be changed more easily than the optics, this thesis and the following part concentrates on the optical design. The throughput optimisation can be divided into parts related to the geometry of the optical system, such as mirror sizes, mirror positions, focal lengths, apertures or sample size. This optimisation is based on the étendue [60, 61] (paraxial quantity) and ray tracing. The second factor is related to losses along the beam path after the light passes through or reflects off windows, polarisers, beam splitters, mirrors and other optical components.

By optimising the beam path geometry and choosing suitable materials, the loss of light travelling through the system is reduced. This allows more light to reach the detector and improves the SNR.

3.1.1 Étendue

The optical throughput describes the efficiency with which an optical system can collect and transfer light from a source to the detector. The goal in optics design is to minimise the losses in the system and, therefore, maximise the throughput. Losses appear either when light interacts with materials, e.g., absorption, or when the beam is bigger than

the optical components. The étendue provides a definition for the concept of how many light rays can be transmitted through an optical system and is typically defined in paraxial quantities [61]. It can be written as [60, 61]

$$E = A_\mathrm{i}\Omega_\mathrm{i} = A_\mathrm{s}\Omega_\mathrm{s}, \tag{3.1}$$

with the refractive index n taken as unity, A_i representing the illuminated surface area, Ω_i the solid angle with which the surface area is illuminated, A_s the surface area of the light source and Ω_s the solid angle of emission. Ideally, the étendue is conserved throughout the focal points of the system[1] and can be used to estimate the shape and size of the optical components. The conservation of étendue is also true for an object emitting a divergent beam, which is then focused to create an image. When an aperture clips the beam, the étendue is reduced and equatable with a loss of intensity. The étendue can also be understood as a phase space volume of the light beam, which is incompressible. Therefore, reducing the illuminated area A will increase the solid angle of the illumination beam Ω, and vice versa.

In real systems with extended sources, the parallel beam exhibits divergence, corresponding to the solid angle Ω of the beam. The solid angle Ω increases by focusing the parallel beam, and the illuminated area A in the focal plane decreases, keeping the étendue unchanged. When focussing a nearly parallel beam, the solid angle Ω is inversely proportional to the focal length of the optical element. In the case of a large parallel beam diameter, as is the case for the IR beam at the spectrometer exit, a small illumination area requires a short focal length and a large solid angle.

3.1.2 Optical design

When developing the optical system, several design parameters must be taken into consideration. This is particularly important when fitting optics into an existing surface analysis chamber [62] (see also Figure 4.1), as spatial boundary conditions limit the freedom of the design to optimise the system to its maximum potential. Therefore, it is essential to clearly understand these parameters before designing the measurement system. The optical system is the basis of the measurement system, and any compromises in the design must be made carefully.

In this thesis, the key design parameters include the existing surface analysis chamber, the geometry of the adsorbate-covered area on the sample [see Figure 3.13(a)] created by a molecular beam [63, 64], the spectrometer, optimal measurement parameters derived from theoretical calculations, and the capability of measuring low coverages. To optimise the final system, it is efficient to generate an optical concept with mirror positions and sizes of the optical elements based on étendue to achieve high throughput and compatibility with the existing chamber. The development of the optical system can-

[1] In realistic optical systems, a parallel beam will exhibit divergence, which can be interpreted as a focused beam that has been focused by an optical element with a long focal length.

not be neatly separated from the mechanical design. During the optics design process, rough checks and estimations of the mechanical design must be made.

The main objective for designing the optical path of the IRAS setup is to efficiently guide all radiation emitted from the spectrometer output to the adsorbate-covered area of the sample and then to the detector. To achieve this, étendue provides a good tool for developing the basic optical concept. Here, it is vital to consider the starting condition arising from the commercially available Bruker VERTEX 80v spectrometer used in the presented IRAS setup. This instrument provides an almost parallel IR beam of approximately 40 mm diameter at the external measurement exit and a divergence of about 1.7° at a J-stop setting of 6 mm (see equation 2.6). This determines the initial étendue. Conservation of étendue now states that the same étendue is available to illuminate the sample (see equation 3.1). A molecular beam [63, 64], which is used in the surface analysis chamber for adsorbate dosing, generates a adsorbate-covered area with 3.5 mm diameter on the sample surface. All the IR radiation must be reflected off the adsorbate-covered area to get maximum adsorbate information. One can estimate the required solid angle of illumination using the known étendue and illumination area size, defined by the molecular beam spot. Consequently, it is possible to evaluate the focal length of the mirror needed to illuminate only the adsorbate-covered area.

The result is a short focal length of a few centimetres for the illumination mirror. To collect all the reflected light, the collection mirror should have a focal length similar to the illumination mirror if both mirrors are similar in size. The short focal length design ensures a small illumination spot on the sample, leads to high throughput and is a key feature of the IRAS optics. It requires placing these two mirrors inside the UHV chamber. The boundary conditions given by the UHV chamber also influenced the focal lengths because existing measurement techniques hindered the free placement of the mirrors inside the chamber. Using short focal lengths is uncommon. Other IRAS systems utilise longer focal lengths [27, 65–68]. Also designs with the illumination and the collection mirror outside the UHV chamber were checked, but resulted in large optical components incompatible with the spatial restrictions or low throughput due to long focal lengths featuring a large illuminator spot. The last part of the optical system involves collecting all light with the detector. Combining the boundary conditions of the detector, i.e., the detector element size ($1 \times 1\,\mathrm{mm}^2$), the field of view of the detector (60°), and the étendue, an even shorter focal length can be estimated compared to the illumination mirror because the illumination spot on the detector has to be smaller than on the sample to gather the maximum amount of the light.

The fundamental parameters for achieving maximum light throughput are established with these three focal lengths of the mirrors. By considering the size of the room and chamber, the position of the chamber within the room, the space required for moving equipment, and the dimensions of the spectrometer, along with applying the concept of étendue, it is possible to estimate the parameters for the complete optical layout that transfers the beam between the spectrometer and chamber. This leads to a system design with four elliptical mirrors (two located in the UHV chamber) for efficient

light transfer into and out of the chamber and one parabolic mirror to focus the parallel light beam from the spectrometer (see Figure 3.1). Furthermore, it sets the foundation for optimising the optics with a standard optical ray tracing program.

In addition to basic parameters from the étendue estimation, grazing light incidence on the sample, lossless mirrors, lossless windows and a simplified spectrometer model [38, 69] were used to simulate the optics with the sample in IRAS measurement position. Furthermore, spatial constraints by the UHV system were also considered. The optical throughput was maximised for the full incidence angle range in the first step of the optimisation process. This also included finding the best parameters for the width and position of illumination-shaping slit to reduce the illumination of the adsorbate-free area on the sample (see Section 3.3.4). Optimising the system for the full angle range leads to a balance between optimum parameters for low incidence angles and grazing incidence angles. However, the system can be used in both cases without a change in the optics and significant throughput loss. The optimisation process was performed for a J-stop setting of 6 mm. Utilizing the maximum available J-stop of 8 mm in the spectrometer did not improve the simulated throughput. This was later verified with the real system.

In the second step, the optical system was refined to reduce sensitivity to manufacturing tolerances of optical components, the optical platform and deviations from the ideal optical path. Two mirrors, the spectrometer-link mirror and the detector mirror, were identified as crucial for adjusting the throughput and focal spot positions. These mirrors were made adjustable to correct for optical misalignment and manufacturing errors, ensuring a high-performance IRAS system. The other three mirrors are fixed to enhance long-term stability.

Figure 3.1 schematically shows the optimised IRAS system with its main optical components. The focal lengths of the mirrors in the system are collected in Table 3.1. The illumination path transfers the IR light beam with an approximate diameter of 40 mm from the spectrometer exit (Bruker VERTEX 80v) over the spectrometer-link mirror, the input mirror and the illumination mirror to the sample.

At the spectrometer exit, indicated by “IR” and a white arrow, the parallel beam passes through a 3.5 mm thick wedged BaF_2 window with a clear aperture of 49 mm. To prevent interference peaks in the measured spectra, all windows along the beam path feature a wedge angle of 0.5°. A commercial, off-axis parabolic mirror (shown in black in Figure 3.1) focuses the light at the polariser focus. Positioned 9.6 mm after the focus point, a 2 mm thick rotatable holographic wire-grid polariser (Medway Optics, BaF_2, grid spacing: 0.25 µm) creates linear polarised light. The polariser substrate is BaF_2. The input mirror follows the polariser. It is an off-axis elliptical mirror, reflecting the light through the illumination-shaping slit located at the shaping focus. The shaping focus between the input mirror and the illumination mirror ensures an efficient light transfer over a distance of nearly 1 m with minimal loss. At the boundary between the high vacuum box and the UHV chamber, the beam passes through a 3 mm thick

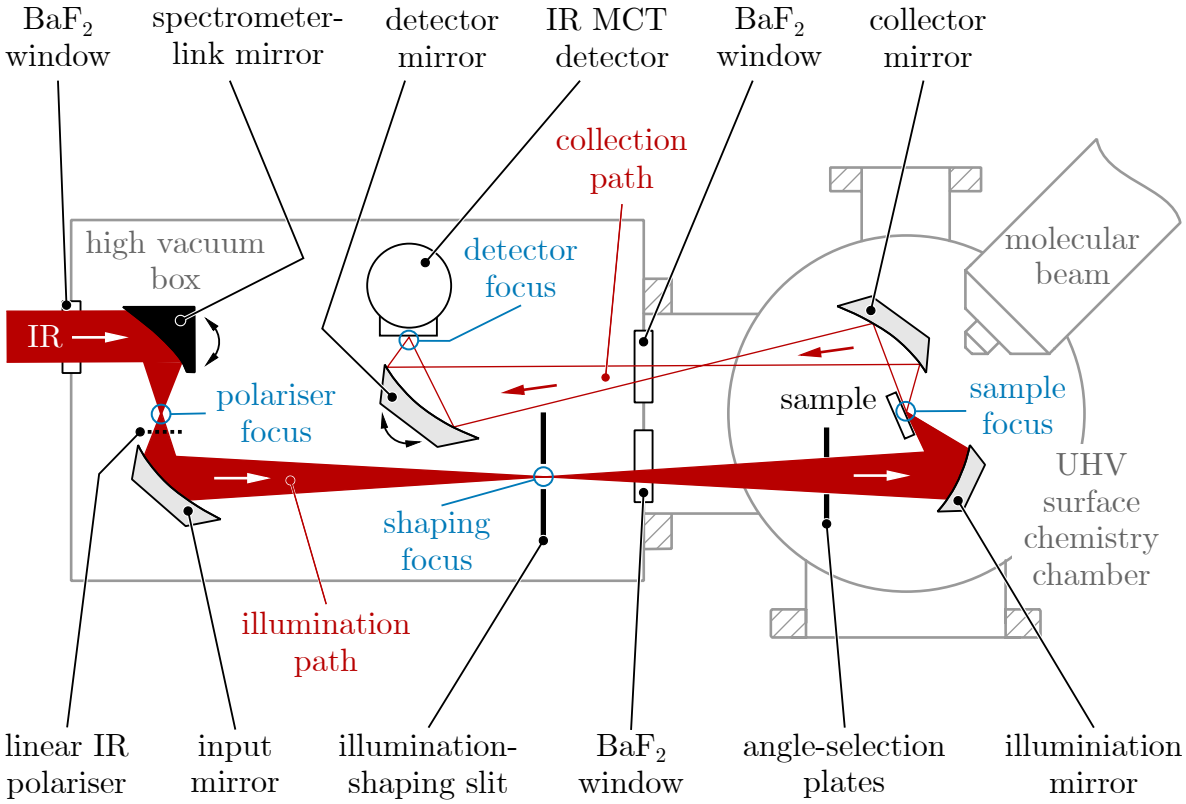

Figure 3.1: Schematic optical path of the IRAS system. The complete IR path is visualised in red. The illumination path is depicted in full red, and the collection path has a red outline. The focal points are indicated with blue circles. The mirrors of the IRAS system, an off-axis parabolic mirror (black), four off-axis elliptical mirrors (grey with a black outline) and additional optical components can be seen. The detector is a liquid-nitrogen-cooled mercury cadmium telluride (MCT) detector. The functional apertures of the optical system (illumination-shaping slit, angle-selection plates) are visualised as black rectangles. The black double arrows indicate the adjustable mirrors. This figure is adapted from [34].

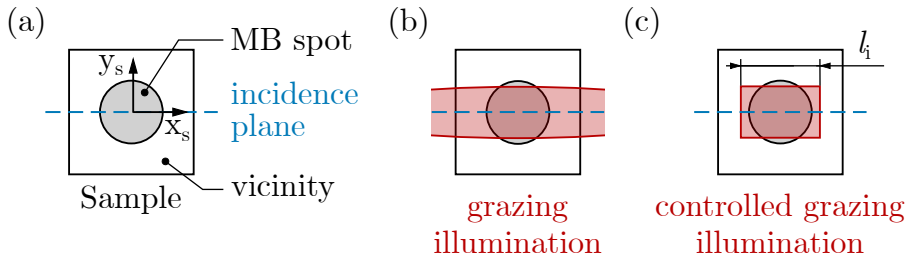

Figure 3.2: Schematic illustration of the sample and different illumination cases. (a) shows the sample with the central MB spot (grey) defining the adsorbate-covered sample area, the sample coordinate system (x_s, y_s) and the projection of the light incidence plane (blue, dashed line) along x_s. The vicinity is the adsorbate-free area. (b) Sample illumination under grazing angle: the illumination exceeds the sample area in the direction of the light incidence. (c) shows a by the illumination-shaping slit controlled illumination of the MB spot with an illumination length l_i. The illumination is visualised in red.

wedged BaF_2 window (clear aperture of 34 mm) and the two angle-selection plates before reaching the illumination mirror. The illumination mirror focuses the light with an illumination cone angle of 39° onto the sample, resulting in an almost rectangular $3 \times 1.5\,mm^2$ sized illumination area at normal incidence (θ = 0°). However, when the sample is in the IRAS measurement position, the illumination area along the incidence plane increases due to grazing incidence as schematically shown in Figure 3.2(b) and (c). The maximum illumination width of 3 mm perpendicular to the incidence plane is not influenced by the grazing incidence of the light. It is smaller than the circular adsorbate-covered area on the sample with a diameter of 3.5 mm. The adsorbate-covered area is created with a molecular beam (MB) [63, 64], also called the MB spot and shown in Figure 3.13(a). The sample area surrounding the MB spot will be called the vicinity. The slightly smaller illumination width compensates for positioning errors of the sample in a perpendicular direction to the incidence plane. Furthermore, it helps to reflect more light from the MB spot. A comparison of the measured and simulated intensity distribution on the surface can be found in Section 5.1.

The illumination of the sample is of tremendous importance for the design, as this is a critical point defining the throughput and the adsorbate sensitivity of the IRAS system. The adsorbate-covered area sets the boundary condition for the illumination on the sample, the MB spot, as shown in Figure 3.2(a). It is crucial to reflect all the light from the MB spot (⌀3.5 mm) for high adsorbate sensitivity and throughput. This cannot be fulfilled at grazing angles anymore because the illumination area exceeds the sample, equating in a loss of throughput and adsorbate sensitivity, schematically shown in Figure 3.2(b). On the one hand, radiation is lost because the illumination exceeds the sample. On the other hand, light detected from the vicinity reduces the signal intensity (see Section 3.3.4) as it contains no information about the adsorbate and only contributes to the background.

Under these circumstances, a small focus spot and a short focal length of the illumination mirror ensures reflecting most of the light from the sample surface. Additionally, a controlled illumination area, ensured by the sample-illumination slit, maintains adsorbate sensitivity. It reduces the influence of the vicinity [see Figure 3.2(c)], which is described in further detail in Section 3.3.4.

Besides the sample-illumination slit, the angle-selection plates also change the sample illumination properties. With these aperture plates, the incidence angle θ measured in the plane of incidence of the light can be controlled by moving the plates into the beam. The illumination length l_i [see Figure 3.2(c)] at lower incidence angles is smaller than for very grazing incidence angles of the light. Even if reducing the throughput seems counterintuitive, it can increase the IRAS measurement performance. A detailed explanation of this topic and why the angle-selection plates improve the SNR will be given in Section 4.2.3.

The collection beam path directs the IR light reflected from the sample to the detector and is shown in Figure 3.1 with a red outline. The path includes two off-axis elliptical mirrors and a wedged BaF_2 window. The key element in this part of the IRAS system is the complete collection of the light reflected from the sample at the detector, which requires efficient transmission with minimal losses. The intermediate focus point achieves an efficient light transfer between the two mirrors, separated by about 0.6 m. To realise the complete collection of the reflected light from the sample, the collector mirror is designed with a slightly shorter front focal length than the back focal length of the illumination mirror. This design keeps the optical system compact within the chamber and reduces sensitivity to sample tilts around x_s [see Figure 3.2(a)]. Additionally, it enables sample rotation up to ±3° out of the ideal IRAS measurement position (around y_s) without significant loss of throughput, compensating incidence angle deviations. Due to the limited space, which restricts the distance between the collector mirror and the detector mirror, maximising the collected light at the detector required some compromises. The detector has a field of view of 60° and a $1\times1\,\mathrm{mm}^2$ sized detector element, which is 45° rotated, so the diagonal is aligned with the y_s direction of the sample. The detector mirror focuses the light with a cone angle of about 64° onto the detector element.

The reproduction scale of an optical system is defined as the ratio of the size of an image produced by the system to the size of the object being imaged [39]. Multiplication of the mirror reproduction scales (see Table 3.1) results in the total reproduction scale β_total = 0.31 of the IRAS system between the J-stop and the detector. The J-stop of diameter 6 mm is demagnified to a size of 1.86 mm at the detector, slightly bigger than the diagonal of the detector element measuring 1.4 mm.

Maximising the achievable intensity on the detector with the consideration of the limited space and the limitations of the detector, therefore, required a balancing of the focal lengths of the collector mirror and the detector mirror. This resulted in a simulated throughput of about 66 % for all the light reflected from a $6\times6\,\mathrm{mm}^2$ sample reaching

mirror name	mirror type	front focal length (mm)	back focal length (mm)	reproduction scale β
spectrometer collimation mirror[2]	90° off-axis parabolic	100	—	0.5
spectrometer-link mirror	90° off-axis parabolic	—	50.8	
input mirror	90° off-axis elliptical	50.9	281.2	5.52
illumination mirror	60° off-axis elliptical	409.8	60.2	0.15
collector mirror	90° off-axis elliptical	50.9	281.2	5.52
detector mirror	90° off-axis elliptical	308.7	43.4	0.14

Table 3.1: Parameters for the mirrors used in the IRAS system. The type of mirror, distance to the focus points, and reproduction scales are specified for each mirror. The reproduction scale β for the first two mirrors is given only for the combination of the two off-axis parabolic mirrors because the beam between these mirrors is parallel. The total reproduction scale of the system (between J-stop and detector) is $\beta_{\text{total}} = 0.31$. The front or back focal length correspond to the effective focal length for the off-axis parabolic mirrors. For the off-axis elliptical mirrors the front focal length corresponds to the object distance and the back focal length to the image distance.

the detector element and a throughput of about 73% for the light reflected from the MB spot compared to a system where all light reflected from the sample is detected. Based on the throughput estimation using the étendue some losses are expected.

The optimisation of throughput also involves selecting appropriate materials for the optical components to minimise reflective and transmissive losses within the desired measurement range of 1000 $\text{cm}^{-1}$to 4000 cm^{-1}. Also, reducing the number of optical surfaces is crucial in reducing these losses. The IRAS setup described in this text includes two main types of mirrors: an off-axis parabolic mirror and four custom-made off-axis elliptical mirrors. The spectrometer-link mirror is an off-axis parabolic mirror with a gold-plated reflective surface featuring an average reflectivity of ≥ 98 % in the targeted wavelength range. The custom-made off-axis elliptical mirrors are manufactured from EN AW-6061-T6 type aluminium. The reflective surface of these mirrors is covered by the native oxide of the aluminium, resulting in an average reflectivity of ≥ 98,% for the relevant wavenumber range. To reach high detection sensitivity a liquid nitrogen cooled mercury cadmium telluride (MCT) detector from InfraRed Associates with a $1 \times 1\,\text{mm}^2$ detector element and a field of view of 60° is implemented into the IRAS system. This detector features an approximately 1 mm thick BaF_2 window in front of the detection element, a spectral range reaching from 850 cm^{-1} to 12000 cm^{-1}, a specific detectivity bigger than $4 \times 10^{10}\,\text{cm}\,\text{Hz}^{1/2}\,\text{W}^{-1}$ and a liquid nitrogen dewar which keeps the detector element cold for 12 h.

The windows in the IRAS system are made from BaF_2. In the wavenumber range from 1200 cm^{-1} to 5000 cm^{-1} this material features a higher transmission of about 95 % compared to 90 % of KBr ($n_{\text{KBr}} > n_{\text{BaF}_2}$), which is also commonly used as window material. Therefore, the windows that separate the chambers with the different pressure regimes – the FTIR spectrometer (≈ 1 mbar), the high-vacuum box (≈ 10^{-3} mbar) and the UHV chamber (≈ 5×10^{-11} mbar) – feature window thicknesses of about 4 mm

and show an increasing absorption from about 1000 cm^{-1} to lower wavenumbers. The substrate of the linear holographic wire grid polariser is also BaF_2.

Effective J-stop of the IRAS system

Reducing the J-stop from 6 to 4 mm decreases the illumination area size on the detector element. The smaller J-stop leads only to minor intensity losses of about 4 %, although the light transmission area (J-stop area) reduces over 50%. This small intensity loss is due to the cut of the illumination area by the detector, when a J-stop of 6 mm is used. Furthermore, the 10 mm wide illumination-shaping slit clips the beam at the sides in the shaping focus at a J-stop setting of 6 mm. So, a reduction of the J-stop does not reduce the size of the whole illumination area in the shaping focus, but only parts which pass through the slit. The complete beam passes through for J-stop values lower than 3.5 mm. This also contributes to the fact that only small losses occur till a J-stop setting down to 4 mm. Below 3.5 mm, a more substantial intensity decrease compared to larger J-stop settings can be observed.

The J-stop diameter is directly linked to the throughput of the IRAS system and the best achievable resolution $\Delta\tilde{\nu}_{\text{limit}}$ as defined in equation 2.7. In this context, it was mentioned that for IRAS systems measuring with lower resolution, the J-stop is often not the field stop that defines the illumination size on the detector (see Section 2.1). Instead, the detector itself limits the divergence of the rays that are used for the spectrum (see Section 3.1.2 and 5.1). Therefore, the effective J-stop diameter $d_{\text{J,effective}}$ was introduced in equation 2.8. With the total reproduction scale of $\beta_{\text{total}} = \beta_{\text{J,effective}} = 0.31$ between the J-stop and the detector, discussed in Section 3.1.2 and Table 3.1, it is possible to calculate the effective J-stop diameter of the IRAS optics. J-stop diameters larger than this effective J-stop will not affect the resolution limit. However, lower values affect the best achievable resolution.

In the case of the IRAS setup presented in this thesis, the calculated effective J-stop is 4.5 mm (not available in the standard configuration of the Bruker VERTEX 80v). Here, the MCT detector element diagonal of 1.4 mm was assumed as the maximum size of the illumination area. With equation 2.7 this results in a resolution limit of $\Delta\tilde{\nu}_{\text{limit}} = 1.7\,cm^{-1}$. Note that this calculation is based on paraxial concepts. So, the resolution limit might be slightly lower in the real system due to optical aberrations.

3.2 Signal Optimisation

In the design of an optical measurement system, it is essential to maximise the signal-to-noise ratio. This includes maximising the throughput, which impacts the noise described in Section 3.1 before, and maximising signal intensities (peak heights). Both measures result in better measurement performance of the system, i.e., reduced measurement time and enhanced sensitivity to low coverages.

As demonstrated in Section 2.4, it is necessary to thoroughly investigate the signal behaviour as a function of the incidence angle. This is because non-metallic substrates can exhibit effects such as band inversion at the Brewster angle. Depending on the measurement case, this necessitates the counterintuitive approach of using a lower throughput by eliminating undesired angles of incidence for the measurements, resulting in a higher signal-to-noise ratio. However, signal intensities are influenced not only by the incidence angle. Also, effects occurring in real optical systems, e.g., depolarisation or incidence angle spread and the detection of light reflected from the adsorbed-free surface, reduce the signal intensity and alter its angle dependence (see Section 3.3).

3.2.1 Incidence Angle Optimisation

The sensitivity of IRAS measurements on non-metallic substrates is highly incidence angle-dependent (see Section 2.4.2). Therefore, choosing the right incidence angle is a crucial element to optimise the SNR and depends on the IR light polarisation, the orientation of the changing dipole moment on the surface and the position of the Brewster angle or the pseudo-Brewster angle, respectively. Due to the focused light beam illuminating the sample, measurements are always performed with a specific angle range. The IRAS setup presented can optimise this incidence angle range between 48° and 87° to provide optimal measurement conditions for different materials and polarisations. For this, the angle-selection plates modify the IR beam before the illumination mirror (see Figure 3.1).

Figure 3.3 shows a more detailed explanation of the two independently movable angle-selection plates fitted to the IRAS setup. (a) depicts the angle-dependent signal as shown in Figure 2.8 and the full measurement range between θ_{min} and θ_{max}. Additional schematic peaks indicate the peak orientation in the spectrum. Four illumination cases with varying angle ranges are shown: (b) the full range, (c) the grazing range, (d) the non-grazing range and (e) the partial range. Figure 3.3 (b) shows a measurement configuration with the full angle range of the system (θ_{min} = 48° to θ_{min} = 87°, see Section 3.3.4) where the angle-selection plates (APS) do not obstruct the beam. In (c), the grazing range, the non-grazing angle selection plate is moved into the beam. Here, grazing angles from $\theta_{\mathrm{L,N}}$ to 87° can pass. Lower incidence angles ranging from 48° to $\theta_{\mathrm{L,N}}$ are clipped. $\theta_{\mathrm{L,N}}$ is the angle limit for the non-grazing range indicated by the subscript N. (d) shows the non-grazing range where the grazing angle selection plate is moved into the beam. Here, rays with incidence angles from 48° to $\theta_{\mathrm{L,G}}$ pass to the sample, whereas the very grazing angles from $\theta_{\mathrm{L,G}}$ to 87° are blocked. In the case of the grazing range and the non-grazing range, only one angle-limiting plate is moved. In contrast, the partial range, depicted in (e), utilises both angle-selection plates moving into the beam, establishing an angle range between $\theta_{\mathrm{L,N}}$ to $\theta_{\mathrm{L,G}}$. These limiting angles θ_{L} must be between θ_{min} = 48° and θ_{min} = 87°. The angle-selection plates only limit the incidence angles measured in the plane of incidence. The extent of the illumination cone angle perpendicular to the plane of incidence is not limited by the aperture plates. The mechanical realisation and the position readout of the angle-selection plates is

discussed in Section 4.2.3. Moving an angle-selection plate into the beam reduces the throughput of the system, consequently increasing the noise. However, for p-polarised measurements, clipping the beam at the right limiting angle θ_L gives a better SNR despite lower throughput as the signal intensity increases.

For p-polarised measurements, the Brewster angle θ_B is the crucial criterion. The material reflectivities in Figure 2.6 show that the position of θ_B depends on the refractive index (see equation 2.17) of the substrate and changes position significantly, e.g., when comparing TiO_2 and Fe_3O_4(see Figure 2.6). At this critical angle, band inversion occurs. This means that the orientation of the signal in the spectrum changes [see Figure 3.3(a)]. A simultaneous measurement of positive and negative signals results in a small or zero signal. Therefore, the specific signal characteristics on non-metallic substrates require a restriction, roughly speaking, to one side of the Brewster angle.

For substrates with a vanishing extinction coefficient k, as shown for TiO_2 in Figure 2.8, $\Delta R/R_0$ for p-polarisation and perpendicular dipole moment orientation (red, solid curve) shows maximum peak heights around the Brewster angle. However, the low reflectivity of TiO_2 at these angles drastically limits the throughput and consequently results in significant noise [see Figure 2.6(a)]. Despite the high peaks, the limited throughput leads to poor SNR. For improved SNR, a wide angle range is better. The limiting angle θ_L has to be set close to the Brewster angle θ_B. The other angle-selection plate is set to allow incidence angles up to θ_{max} or θ_{min}, depending on the desired angle range (grazing or non-grazing). By this, the signal intensity averages over the measurement range, but the increased throughout reduces the noise to achieve maximum SNR. Setting the limiting angle θ_L as before, close to the Brewster angle, and the second angle-selection plate such that θ_{max} or θ_{min} is clipped by a few degrees may improve the signal further. This depends on the shape of the $\Delta R/R_0$ curve. As will be shown later (Section 3.3), the shape of the ideal curve is altered by various effects impacting the optimised measurement angle range. Utilising the angle-selection plates also improves p-polarised measurements with parallel dipole moments.

On Fe_3O_4 shown in Figure 2.9, a material with a non-vanishing extinction coefficient k, the pseudo-Brewster angle remains an important criterion. However, the band inversion for p-polarised signals does not appear at $\theta_{B,pseudo}$ directly. Instead, for p-polarisation and parallel dipole moments, the angle of band inversion is smaller than $\theta_{B,pseudo}$, and for perpendicular dipole moments, it is higher than $\theta_{B,pseudo}$. This has to be considered when setting the angle range for p-polarised measurements to avoid the simultaneous measurement of positive and negative peaks. Also, the reflectivity R_0 is no longer zero at the minimum.

Reflection of s-polarised light does not exhibit band inversion as demonstrated in Figure 2.8 and 2.9. Therefore, measurements with s-polarisation require no restriction of the incidence angle range, independent of the substrate. Here, it is beneficial to utilise the whole throughput of the system to reduce the noise and maximise SNR as long as the detector does not saturate.

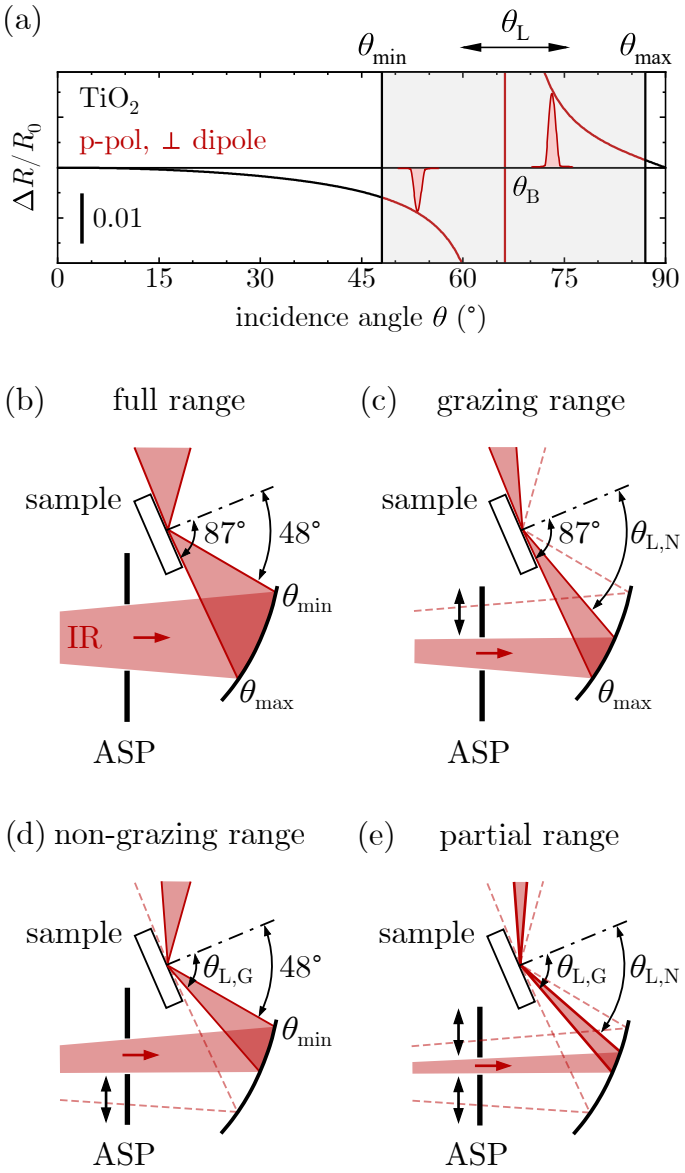

Figure 3.3: Schematic illustration of various possible angle-selection plate (ASP) settings for IRAS measurements. (a) shows the normalised reflectivity difference on TiO_2 as shown in Figure 2.8 with schematic peak orientations. θ_B marks the Brewster angle ant the zero-crossing. (b) full range: angle-selection plates are fully open, have the largest possible usable angle range, and do not clip the beam. (c) grazing range: only grazing incidence angles from to $\theta_{L,N}$ to 87° pass and low incidence angles are clipped. (d) non-grazing range: only non-grazing incidence angles from 48° to $\theta_{L,G}$ pass and grazing incidence angles are clipped. (e) partial range: every desired incidence angle range between θ_{min} and θ_{max} can be set. This Figure is partly adapted from [34]

The setting of the angle-selection plates is not only defined by the maximum SNR. Still, they can also control the signals originating from the different adsorbate orientations on the surface. At very grazing angles, the parallel components of the incident light show a decreased response (see Figure 2.11). When multiple dipole moment components are visible simultaneously in the spectrum and overlap, grazing angle measurements can be used to enhance signals from perpendicular dipole changes and reduce signal intensities from parallel components.

Thus, besides controlling the SNR, the angle-selection plates can also be used to control the magnitude of the signals contributing to the spectrum. As a result, the correct incidence angle range has to be chosen wisely according to the requirements of the investigated system, including the substrate material, measurement polarisation, and orientation of the vibrational modes on the surface.

3.3 Effects in Real Systems

In real optical systems, optical errors lead to deviations from the ideal behaviour of the infrared light beam as it travels through the system. The following section examines the impact of light beam depolarisation [61, 70], angular spread of the light beam [55, 71], and the effects of reflection from adsorbate-free sample surfaces. All these effects share a common consequence: a reduction in signal intensity observed in the final spectrum. When considering the influence of parameters on the signals alongside sample reflectivity, the normalised intensity change $\Delta I/I_0$ at the detector is the accurate definition instead of $\Delta R/R_0$. However, for simplicity, it is still referred to $\Delta R/R_0$ in the following.

3.3.1 Depolarisation Γ

Light maintains a consistent polarisation state in ideal optical systems as it propagates through the system. However, in real-world optical systems, various factors can introduce polarisation aberrations, causing changes in the polarisation state of light. The depolarisation of light can be attributed to three types of aberrations: diattenuation, retardance [72], and skew [61, 73]. Diattenuation aberration occurs when different polarisation components of incident light experience different attenuation levels as the light passes through or reflects on a material. Retardance aberration occurs when different polarisation components of light experience different phase delays. For skew aberration, depolarisation emerges purely due to geometric effects resulting in a rotation of the polarisation state, which leads to an intermixing of the s- and p-components of the light. This aberration is mostly noticeable in optical systems with a high numeric aperture [73].

The s- and p-polarised components can be mixed to describe the depolarisation. Hence, the reflectivity of a surface measured at the detector can be expressed as effective reflectivity [70] for s-polarised light

$$R_{0,\mathrm{s}}^{\mathrm{eff}} = R_{0,\mathrm{s}} + \Gamma_{\mathrm{p}}(R_{0,\mathrm{p}} - R_{0,\mathrm{s}}) \tag{3.2}$$

and for p-polarised light

$$R_{0,\mathrm{p}}^{\mathrm{eff}} = R_{0,\mathrm{p}} + \Gamma_{\mathrm{s}}(R_{0,\mathrm{s}} - R_{0,\mathrm{p}}), \tag{3.3}$$

with the light reflecting off the clean surface. Here, $\Gamma_{\mathrm{j}} = I_{\mathrm{j}}/I$ defines the depolarisation factor as the ratio of the intensity I_{j} of the "leaking-in" polarisation component and the total intensity I transmitted through the polariser. The index j indicates s or p polarisation. The light reflecting off the adsorbate-covered surface can be calculated according to

$$R_{\mathrm{s},\parallel}^{\mathrm{eff}} = R_{\mathrm{s},\parallel} + \Gamma_{\mathrm{p}}(R_{0,\mathrm{p}} - R_{\mathrm{s},\parallel}), \tag{3.4}$$

$$R_{\mathrm{p},\parallel}^{\mathrm{eff}} = R_{\mathrm{p},\parallel} + \Gamma_{\mathrm{s}}(R_{0,\mathrm{s}} - R_{\mathrm{p},\parallel}) \tag{3.5}$$

and

$$R_{\mathrm{p},\perp}^{\mathrm{eff}} = R_{\mathrm{p},\perp} + \Gamma_{\mathrm{s}}(R_{0,\mathrm{s}} - R_{\mathrm{p},\perp}), \tag{3.6}$$

when only one orientation of the dipole moment, out of the three main cases (s$\parallel$, p$\parallel$, p$\perp$), affects the reflected light. In case of an additional dipole moment oriented along one of the two remaining main directions, $R_{0,\mathrm{s}}$ or $R_{0,\mathrm{p}}$ in equation 3.4 to 3.6 have to be replaced by the corresponding reflectivities from the adsorbate covered surface.

The degree of polarisation is usually documented on the data sheet for polarising optical components. The IRAS system presented utilises a linear holographic wire-grid polariser from Medway Optics Ltd with a wire grid spacing of 0.25 µm (4000 lines per mm) processed on a 2 mm thick BaF_2 substrate. The degree of polarisation at 2.5 µm is specified with 99.5 %. At a perfect orientation of the polariser, this results in a depolarisation factor of $\Gamma = 0.005$.

As mentioned above, another source of depolarisation is the mirrors. The Jones formalism [72, 74] allows to describe the polarisation when the light travels through the system. There, the Jones vector (J-vector) represents the electromagnetic wave (which describes the magnitude and phase of the E-field in 2D). The polarising optical components are characterised by the Jones matrix modifying the J-vector. Note that the k-vector is assumed to be perpendicular to the E-field, and changes of the E-field in the z-direction are not included in the analysis.

This formalism was used in the simulation to approximate the depolarisation occurring between the polariser and the sample (see Figure 3.1), when the unpolarised light rays travel from the source via the entrance pupil (source mirror in Figure 2.2) to the sample. The pupil of an optical system defines the light acceptance angle of the system. Normal light incidence onto the sample ($\theta = 0°$) was assumed and a coordinate transformation was applied to the pupil coordinates $(P_{\mathrm{x}}, P_{\mathrm{y}})$ to show the polarisation

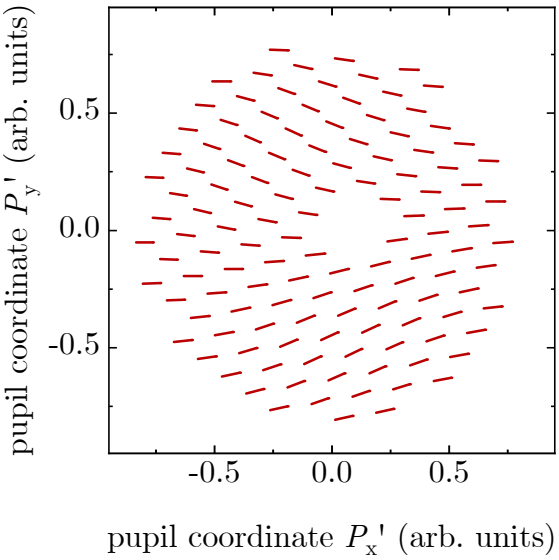

Figure 3.4: Simulated polarisation pupil map for p-polarised light and normal incidence on the sample. The map shows the orientation of the J-vector (reaching the sample) at different positions of the pupil (P'_x, P'_y) and an average depolarisation of $\Gamma = 0.21$. The pupil coordinates (P'_x, P'_y) are normalised to unity, ranging from -1 to 1. The unpolarised light from the source is polarised with the polariser of the IRAS system and then reflected by two mirrors before the beam reaches the sample.

pupil map in sample coordinates (P'_x, P'_y). This resulted in the polarisation pupil map shown in Figure 3.4. Figure 3.4 shows the J-vector orientation of rays traced from the centre point of the source (intersection with the principal ray) through a grid of points (P_x, P_y) on the entrance pupil. Dividing the absolute value of the J_y-component by the magnitude of the field at each intersection point and applying an average over all points gives a depolarisation factor of $\Gamma = 0.21$ for p-polarised light incidence and the full incidence angle range.

The area in Figure 3.4 near $P'_x = P'_y = 0$ without J-vectors is caused by a small prism in the spectrometer beam path, which is used for the HeNe laser to detect the moving mirror position (see Figure 2.2) shading the IR beam. The J-vectors at $P'_x \approx -0.75$ can be associated with incidence angles close to θ_{max} (grazing angles) and those at $P'_x \approx 0.75$ with incidence angles close to θ_{min} (non-grazing angles). Rays reflected from the top of the illumination mirror are represented by J-vectors at $P'_y \approx 0.75$ and those reflected on the bottom of the illumination mirror can be associated with the J-vectors at $P'_y \approx -0.75$. Moving the angle selection-plates into the beam changes the average depolarisation, equivalent to shading some areas in the polarisation pupil map (Figure 3.4). So, various incidence angle ranges show different degrees of depolarisation. For s polarisation, the simulation resulted in an average depolarisation for the full angle range of $\Gamma = 0.2$.

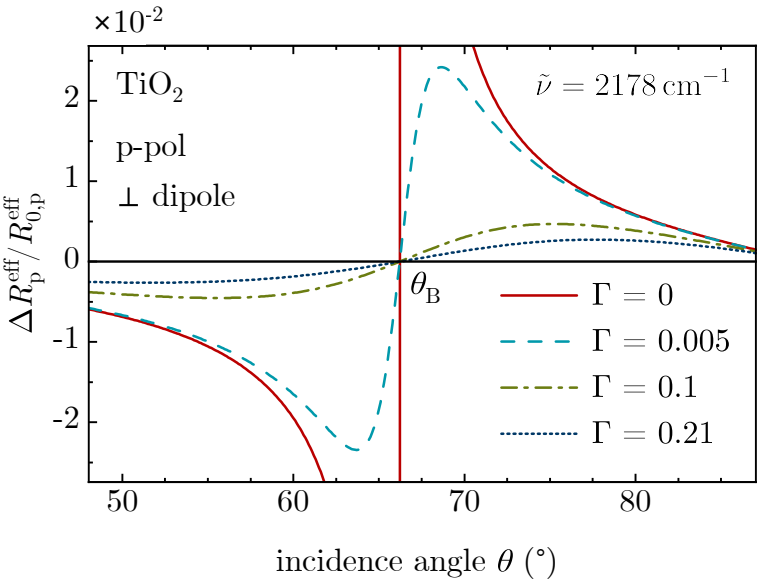

Figure 3.5: Various degrees of depolarisation affecting the ideal normalised reflectivity difference $\Delta R/R_0$. $\Delta R^\mathrm{eff}/R_0^\mathrm{eff}$ is calculated for p-polarised light reflected on TiO_2 with a changing dipole moment normal to the surface at $\tilde{\nu} = 2178\,\mathrm{cm}^{-1}$. The plotted range of the incidence angle θ is the measurement range of the IRAS system. The red (solid) curve indicates the ideal calculation with no depolarisation ($\Gamma = 0$) of the IR beam. The blue (dashed) curve shows a depolarisation of $\Gamma = 0.005$ applied to the ideal curve; the dark green (dash-dotted) and dark blue (dotted) curves show a depolarisation of $\Gamma = 0.1$ and $\Gamma = 0.21$, respectively. θ_B marks the Brewster angle of the uncorrected calculation.

Figure 3.5 shows how the depolarisation changes the signal intensity $\Delta R/R_0$ for a dipole moment normal to the surface and p-polarised radiation reflected at TiO_2. The adsorbate parameters used for the calculation are defined in Section 2.4.2 where the ideal case was already described (red, solid curve in Figure 3.5). The calculation is plotted in the range of incidence angles available with the IRAS system. One can see that the depolarisation of the incident beam smears out the $1/x$-like singularity of the ideal $\Delta R/R_0$. The singularity in the ideal case is caused by the zero reflectivity of p-polarised light at the Brewster angle (see Figure 2.6). Due to depolarisation, an additional s-polarised portion ($R_{0,\mathrm{s}}$) contributes to the p-polarised light. This lifts the effective reflectivity $R^{\mathrm{eff}}_{0,\mathrm{p}}$ to non-zero values at the Brewster angle because the s-polarised reflectivity is not zero and strongly affects the $\Delta R/R_0$ signal. The magnitude of the s-polarised portion is defined by the depolarisation Γ. The s-polarised portion contains no information about the perpendicular oriented dipole moment and only contributes to the background signal, decreasing the relative peak height.

As the depolarisation Γ increases, a significant decrease of the peak heights can be observed, affecting the entire angle range at higher depolarisations of 0.1 and 0.21. Moreover, the highest peak heights are shifted further away from the Brewster angle. At low depolarisation of $\Gamma = 0.005$ (caused by the polariser), the largest peak heights are close to the Brewster angle. The maxima and minima of $\Delta R^{\mathrm{eff}}/R^{\mathrm{eff}}_0$ with their corresponding incidence angles are summarised in Table 3.2. Since the maximum and minimum values of $\Delta R^{\mathrm{eff}}/R^{\mathrm{eff}}_0$ for different depolarisations exhibit significant shifts, the table presents $\Delta R^{\mathrm{eff}}/R^{\mathrm{eff}}_0$ values at $\theta = 57.1°$, which is the midpoint between the minimum measurement limit ($\theta_{\mathrm{min}} = 48°$) and the Brewster angle θ_{B}. For higher incidence angles, the midpoint is at $\theta = 76.6°$ between θ_{B} and the maximum measurement angle of 87°. This enables a better comparison of $\Delta R^{\mathrm{eff}}/R^{\mathrm{eff}}_0$ with respect to measurements within an angle range and a reasonable signal-to-noise ratio. A comparison of $\Gamma = 0.005$ and $\Gamma = 0.21$ reveals a decrease of $\Delta R^{\mathrm{eff}}/R^{\mathrm{eff}}_0$ by a factor of 5.2 at 57.1° and 3.2 at 76.6°. The impact of depolarisation is more pronounced for incidence angles below θ_{B}. Note that a change of depolarisation due to a smaller J-stop can be neglected.

Γ	$\Delta R^{\mathrm{eff}}/R^{\mathrm{eff}}_{0,\mathrm{max}}$	θ_{max} (°)	$\Delta R^{\mathrm{eff}}/R^{\mathrm{eff}}_{0,\mathrm{min}}$	θ_{min} (°)	$\Delta R^{\mathrm{eff}}/R^{\mathrm{eff}}_0(57.1°)$	$\Delta R^{\mathrm{eff}}/R^{\mathrm{eff}}_0(76.6°)$
0	3.04	66.3	-7.60×10^{-1}	66.2	-1.32×10^{-2}	9.27×10^{-3}
0.005	2.42×10^{-2}	68.7	-2.35×10^{-2}	63.7	-1.21×10^{-2}	8.87×10^{-3}
0.1	4.69×10^{-3}	75.2	-4.53×10^{-3}	55.5	-4.46×10^{-3}	4.6×10^{-3}
0.21	2.73×10^{-3}	77.7	-2.62×10^{-3}	51.7	-2.32×10^{-3}	2.7×10^{-3}

Table 3.2: Collection of the values for p polarisation and a perpendicular dipole moment. The values are evaluated from Figure 3.5 showing different degrees of depolarisation affecting $\Delta R/R_0$. The table summarises the maximum and minimum values of the incidence angle dependent $\Delta R^{\mathrm{eff}}/R^{\mathrm{eff}}_0$ for p-polarised light incidence on a TiO_2 surface and an adsorbate defined in Section 2.4.2. Furthermore, the expected signal intensities at 57.1° and 76.6° are tabulated for better comparability of the different degrees of depolarisation.

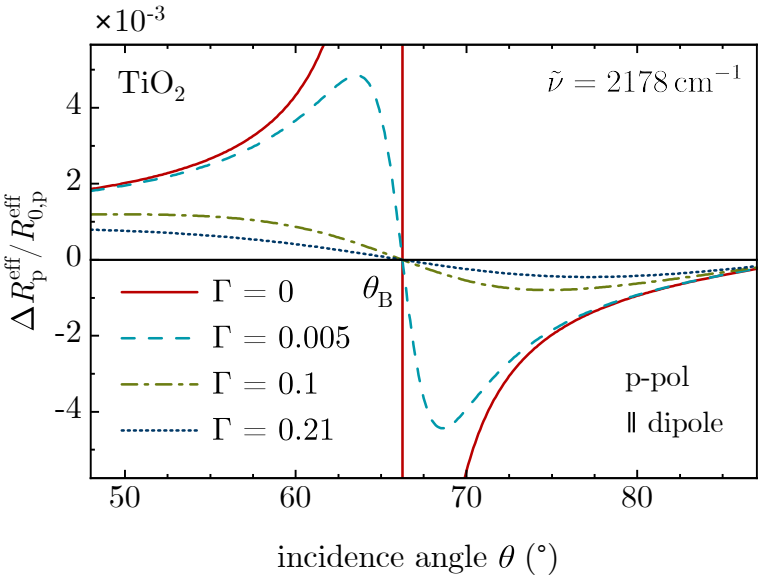

Figure 3.6: Different degrees of depolarisation affecting the ideal normalised reflectivity difference $\Delta R/R_0$. The $\Delta R^{\text{eff}}/R_0^{\text{eff}}$ curves are calculated for p-polarised light reflected on TiO_2 with a dipole moment parallel to the surface and aligned with the incidence plane at $\tilde{\nu}$ = 2178 cm^{-1}. The red (solid) curve indicates the ideal calculation with no depolarisation ($\Gamma = 0$) of the IR beam. The blue (dashed) curve shows a depolarisation of Γ = 0.005 applied to the ideal curve, the dark green (dash-dotted) and dark blue (dotted) curves show a depolarisation of Γ = 0.1 and Γ = 0.21, respectively. θ_B marks the Brewster angle of the uncorrected calculation.

Figure 3.6 shows the influence of the depolarisation on p-polarised signals from parallel to the surface oriented dipole moments aligned with the incidence plane. The leak of s-polarisation leads to a lowered signal intensity, similar to the case p⊥. A comparison of Γ = 0.005 and Γ = 0.21 shows a decrease of $\Delta R^{\text{eff}}/R_0^{\text{eff}}$ by a factor of 5.3 at 57.1° and 3.3 at 76.6°.

Γ	$\Delta R^{\text{eff}}/R_{0\,\max}^{\text{eff}}$	$\theta_{\max}$(°)	$\Delta R^{\text{eff}}/R_{0\,\min}^{\text{eff}}$	$\theta_{\min}$ (°)	$\Delta R^{\text{eff}}/R_0^{\text{eff}}(57.1°)$	$\Delta R^{\text{eff}}/R_0^{\text{eff}}(76.6°)$
0	4.62×10^{-1}	66.2	-3.35×10^{-1}	66.3	3.14×10^{-3}	-1.55×10^{-3}
0.005	4.85×10^{-3}	63.6	-4.44×10^{-3}	68.6	2.88×10^{-3}	-1.48×10^{-3}
0.1	1.19×10^{-3}	46.9	-7.95×10^{-4}	74.7	1.06×10^{-3}	-7.68×10^{-4}
0.21	8.25×10^{-4}	45	-4.53×10^{-4}	77.2	5.54×10^{-4}	-4.51×10^{-4}

Table 3.3: Collection of the values for p polarisation and a dipole moment parallel to the surface in plane of incidence. The values are evaluated from Figure 3.6 showing different degrees of depolarisation affecting $\Delta R/R_0$. The table shows the maximum and minimum values of the incidence angle dependent $\Delta R^{\text{eff}}/R_0^{\text{eff}}$ for a TiO_2 sample and an adsorbate defined in Section 2.4.2. Furthermore, the expected signal intensities at 57.1° and 76.6° are tabulated for better comparability of the different degrees of depolarisation.

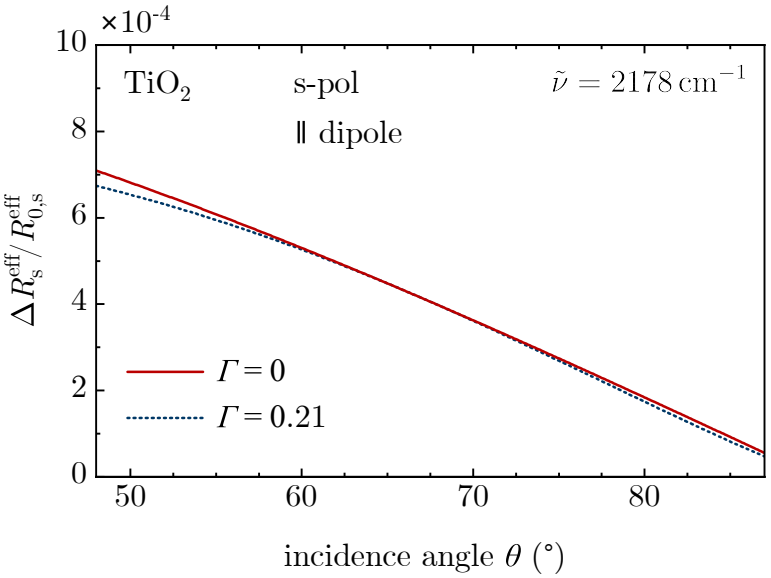

Figure 3.7: Different degrees of depolarisation affecting the ideal normalised reflectivity difference $\Delta R/R_0$. The $\Delta R^{\mathrm{eff}}/R_0^{\mathrm{eff}}$ curves are calculated for s-polarised light reflected on TiO_2 with a dipole moment parallel to the surface at $\tilde{\nu} = 2178\,\mathrm{cm}^{-1}$. The red, solid curve indicates the ideal calculation with no depolarisation ($\Gamma = 0$) of the IR beam. The dark blue (dotted) curve shows a depolarisation of $\Gamma = 0.21$ applied to the ideal curve.

For s-polarisation, shown in Figure 3.7, the effect of signal decrease is negligible even at a depolarisation of $\Gamma = 0.21$. At lower incidence angles $\Theta < 30°$ (not shown) the depolarisation gets more noticeable. This is because p polarisation exhibits a lower reflectivity than s polarisation (see Figure 2.6). At θ_B the signal decrease is zero. However, the leakage of p polarisation might cause additional signals in the s-polarised measurements because the magnitude of p-polarised vibrational signals is up to an order of magnitude higher than s-polarised signals. The presented IRAS system can set the incidence angle range such that p-polarised signals from the left and right of the Brewster angle (positive and negative peaks in p-polarised measurements) cancel out. Also, the reverse can happen and s-signals appear in measurements with p polarisation.

On materials with a non-negligible absorption coefficient k, like Fe_3O_4, the depolarisation effect results in a weaker decrease of the p-polarised $\Delta R/R_0$ compared to TiO_2. Depolarisation affecting the s-polarisation is negligible in the IRAS measurement range, if no p-polarised signal leaks in.

In summary, the depolarisation affects the whole angle range. It has the strongest effect on the achievable signal intensities for p-polarised measurements around the Brewster angle. For s-polarisation, the peak height decrease is negligible. Still, care has to be taken about signals leaking from the polarisation channel that should be nominally suppressed. This might cause additional peaks and can lead to misinterpretation of the spectra, especially when the IRAS measurements are performed only on one side

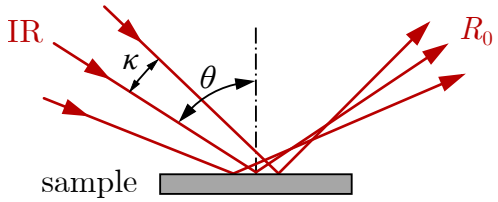

Figure 3.8: Schematic drawing of a focused IR light beam reflecting off a sample in the plane of incidence. The IR beam hits the sample at a nominal incidence angle θ. The focused beam exhibits a cone angle $\pm\kappa$.

of the Brewster angle. In the presented IRAS system, depolarisation can be attributed mainly to skew aberration on the mirrors. Due to the spatial restrictions, a different position of the polariser (closer to the sample), which would reduce this aberration, or an error-compensating mirror layout to reduce depolarisation was not feasible (see Section 6.2).

3.3.2 Incidence Angle Spread

As discussed in previous chapters, the incidence angle θ of light on the sample is crucial. Different incidence angles θ result in different signal intensities. A minimum spread of the incidence angle is always required for measurements because the beam needs to be focused. Therefore, it is important to investigate the factors contributing to the spread of incidence angles hitting the sample, such as divergence, optical errors, and the cone angle κ of the focused beam illuminating the sample. The crucial angles are illustrated in Figure 3.8. The analysis of the incidence geometry focuses on the angle spread in the plane of incidence.

A minimum divergence in the optical path occurs due to the extended source. In the FTIR spectrometer, the divergence is determined by the size of the J-stop, which defines the size of the IR source visible to the interferometer (see Figure 2.2). The divergence of the parallel beam after the collimation mirror is determined by the J-stop diameter and the focal length of the collimation mirror. A J-stop diameter of 6 mm in combination with a collimation mirror focal length of 100 mm results in a divergence of ±1.7° (according to equation 2.6). The J-stop setting of 6 mm represents a standard measurement setting used for IRAS measurements with the presented setup. Smaller J-stop diameters decrease the divergence.

In Figure 3.9, the minimal angle spread of the sample illumination is simulated for a J-stop setting of 6 mm. The y-position of the rays intersecting the movement plane of the angle-selection plates (see schematic sketch in Figure 3.9 and compare to Figure 3.1) is plotted against the incidence angle θ on the sample. The y-position corresponds to the angle-selection plate position in the optical model. Only rays reflected off the sample and reaching the detector contribute to the plotted distribution. Each ray traced through the system and hitting the detector is represented as a red dot in the

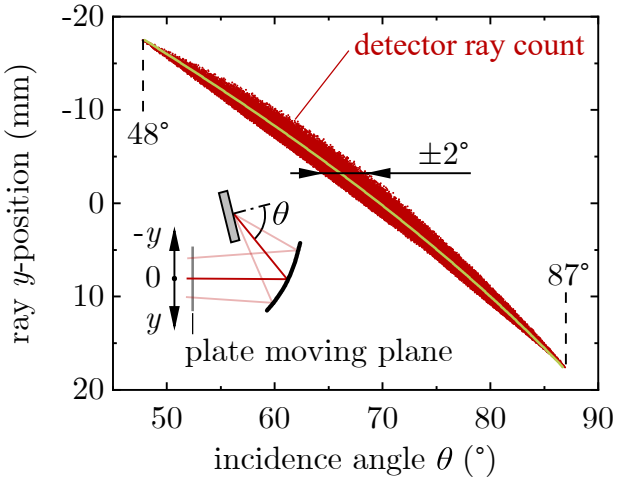

Figure 3.9: Plot for evaluating the spread of the incidence angle when the angle selection plates form a very narrow slit. The y-position where the rays of the beam intersect the plane of the angle-selection plate movement is plotted as function of the incidence angle θ on the sample. Only the rays reflected off the sample and reaching the detector contribute to the plotted distribution. Each ray is represented by a red dot. The light green, solid line is an intensity weighted fit described by $y(\theta) = -34 + 0.06\,\theta + 0.006\,\theta^2$.

diagram. The zero of the y-position is defined by the intersection of the principal ray with the plate moving plane. Figure 3.9 reveals a minimum incidence angle θ_{min} onto the sample of 48°, exhibiting nearly no angle spread at low incidence angles. As the incidence angle θ increases, the angle spread grows to ±2° for a ray y-position around −3 mm. For more grazing incidence angles, the angle spread decreases again. At 87°, representing the upper incidence angle limit of the IRAS system, the angle spread is negligibly small and the intensity vanishes. This means that a perfectly straight cut of the IR beam around the central region ($y = 0$) with one of the angle-selection plates is accompanied by a incidence angle spread of ±2°. The beam clipping further away from the centre shows smaller angle spreads. Furthermore, the simulation shows that the incidence angle range of the IRAS system reaches from 48° to 87°. The green line in the plot represents an intensity-weighted fit, enabling the recalculation of the y-position of the ray for a given θ according to the equation: $y(\theta) = -34 + 0.06\,\theta + 0.006\,\theta^2$. Note that Figure 3.9 estimates the angle-selection error expected at each selection angle. It is not an exact description of the real aperture movement. The angle-selection plates in the real system move along circular trajectories compared to the linear motion in the simulation. Furthermore, the edges of the two plates clipping the IR beam move on two trajectories with a slight offset to each other (see chapter 4). This avoids crashing of the angle-selection plates. It is important to note that the plot illustrates the incidence angle variation within the plane of incidence. Perpendicular to this plane and parallel to the sample surface, the beam always features a non-zero cone angle (largest at $\theta \approx 65$–$70°$).

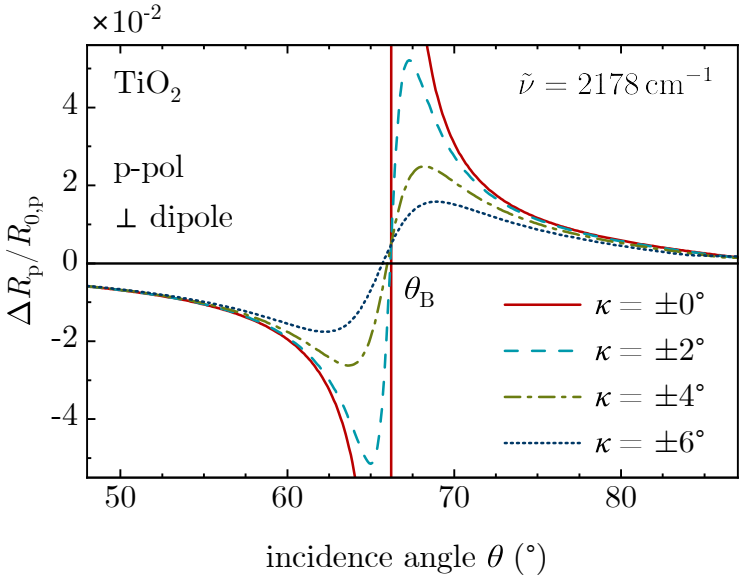

Figure 3.10: Various angle spreads influencing the ideal normalised reflectivity difference, calculated for p-polarised light reflected on TiO_2 with a dipole moment normal to the surface at $\tilde{\nu}$ = 2178 cm^{-1}. The red, solid curve indicates the ideal calculation with no angle spread (κ = ±0°) of the IR beam. The light blue (dashed) curve shows a depolarisation of κ = ±2° applied to the ideal curve, and the dark green (dash-dotted) and dark blue (dotted) curve show a depolarisation of κ = ±4° and κ = ±6°, respectively. θ_B marks the Brewster angle at the zero-crossing of the ideal curve.

Figure 3.10 shows the effect of angle spread on the ideal calculation of $\Delta R/R_0$ for p-polarised light and a dipole moment normal to the surface on TiO_2. To simulate the angle spread, the reflectivity of the adsorbate-covered and the clean surface was first integrated in the $\pm\kappa$ range around θ, and then the normalised reflectivity difference $\Delta R/R_0$ was calculated. The main influence of the angle spread is located around the Brewster angle θ_B, where band inversion leads to the simultaneous contribution of positive and negative peaks to the signal and thus a cancellation of the signal. At incidence angles sufficiently far from θ_B, the angle spread decreases the signals only slightly. This is caused by averaging of the ideal signal $\Delta R/R_0$ over the angle range $\theta\pm\kappa$. Therefore, the signal decrease is more pronounced for larger angle spreads κ and where the ideal curve exhibits steeper slopes. Note that the zero crossing slightly shifts to lower angles at higher angle spreads. It is important to consider the angle spread only when performing p-polarised measurements near the Brewster angle. Nevertheless, some values are collected in Table 3.4. A comparison of the values at the half-angle-points ($\theta = 57.1°$ and $\theta = 76.6°$) between θ_B and the minimum and maximum measurement limit shows that the decrease of the signal due to the angle spread is small compared to the depolarisation. It is more pronounced for angles $\theta > \theta_B$. The calculation for the angle-dependent signal intensity for p-polarisation and a parallel dipole moment orientation behaves similarly, except for the different peak orientations above and below θ_B. This calculation is shown in the appendix in Figure A.1.1.

κ (°)	$\Delta R/R_{0,\max}$	$\theta_{\max}$ (°)	$\Delta R/R_{0,\min}$	$\theta_{\min}$ (°)	$\Delta R/R_0(57.1°)$	$\Delta R/R_0(76.6°)$
0	3.04	66.3	-7.60×10^{-1}	66.2	-1.32×10^{-2}	9.27×10^{-3}
±2	5.21×10^{-2}	67.3	-5.14×10^{-2}	65	-1.30×10^{-2}	8.99×10^{-3}
±4	2.49×10^{-2}	68.2	-2.62×10^{-2}	63.7	-1.26×10^{-2}	8.21×10^{-3}
±6	1.58×10^{-2}	68.9	-1.76×10^{-2}	62.3	-1.19×10^{-2}	7.11×10^{-3}

Table 3.4: Collection of the $\Delta R/R_0$ values for various values κ of the incidence angle spread for p polarisation and a perpendicular dipole moment. The values are evaluated from Figure 3.10. The table shows the maximum and minimum values of the incidence angle dependent $\Delta R/R_0$ for a TiO_2 surface with an adsorbate defined in Section 2.4.2. Furthermore, the expected signal intensities at 57.1° and 76.6° are tabulated, marking the half-point between the measurement limit and θ_B on each side of θ_B.

The $\Delta R/R_0$ calculation for s-polarisation and a dipole moment oriented parallel to the surface and perpendicular to the incidence plane is shown in Figure 3.11. The dark blue (dashed) curve representing an angle spread of $\kappa = \pm6$ exhibits only a negligible drop in the signal over the whole incidence angle range compared to the ideal case [red (solid) curve, $\kappa = \pm0$]. This is because no band inversion occurs for s-polarisation and the slope compared to p-polarisation is low. The small deviation from the ideal case at very grazing angles is caused by the cut-off of the reflected intensity at 90° leading to a narrowing of the effective angle range when $\theta + \kappa > 90°$. Therefore, a slower decrease in the signal intensity occurs.

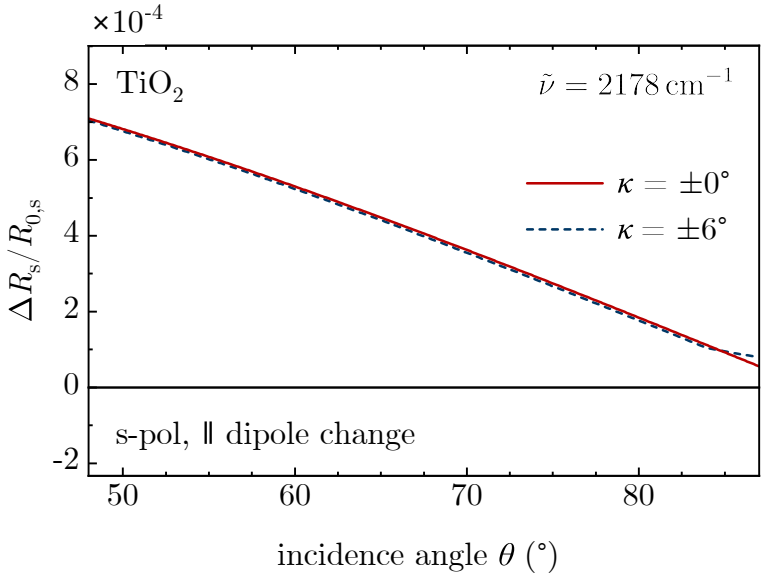

Figure 3.11: Various angle spreads influencing the ideal normalised reflectivity difference. Calculated for s-polarised light reflected on TiO_2 with a dipole moment oriented parallel to the surface and perpendicular to the incidence plane at $\tilde{\nu} = 2178\,\mathrm{cm}^{-1}$. The red, solid curve indicates the ideal calculation with no angle spread ($\kappa = \pm 0°$) of the IR beam. The dark blue (dotted) curve shows an angle spread of $\kappa = \pm 6°$ applied to the ideal curve.

The p-polarised normalised reflectivity difference $\Delta R/R_0$ on Fe_3O_4 (see Figure 2.9) shows overall shallower slopes compared to TiO_2 (see Figure 2.8). Consequently, the angle spread has a smaller impact on the peak height. S-polarised signals on Fe_3O_4 behave the same as on TiO_2.

The decrease in signal intensity due to the angle spread is primarily caused by the band inversion at the Brewster angle θ_B, which only occurs for p-polarised measurements. The plots in this section show that a relatively sharp cutoff of the incidence angle is possible, which is crucial for optimising the signal. Also, a minimum angle spread due to divergence must be considered.

3.3.3 Maximum Achievable $\Delta R/R_0$ Peak Heights with the IRAS Setup

Effects like the depolarisation discussed in Section 3.3.1 and the angle spread shown in Section 3.3.2 lead to altering of the ideal $\Delta R/R_0$ discussed in Section 2.4.2. To estimate the maximum achievable peak heights with the real IRAS system, a minimum depolarisation of $\Gamma = 0.005$ due to the polariser and an incidence angle spread of $\kappa = \pm 2$ originating from the divergent beam and optical errors are assumed. As the skew polarisation aberration is specific to the optical design, it is not considered in the minimal corrections. For materials with vanishing absorption coefficient ($k \to 0$), the

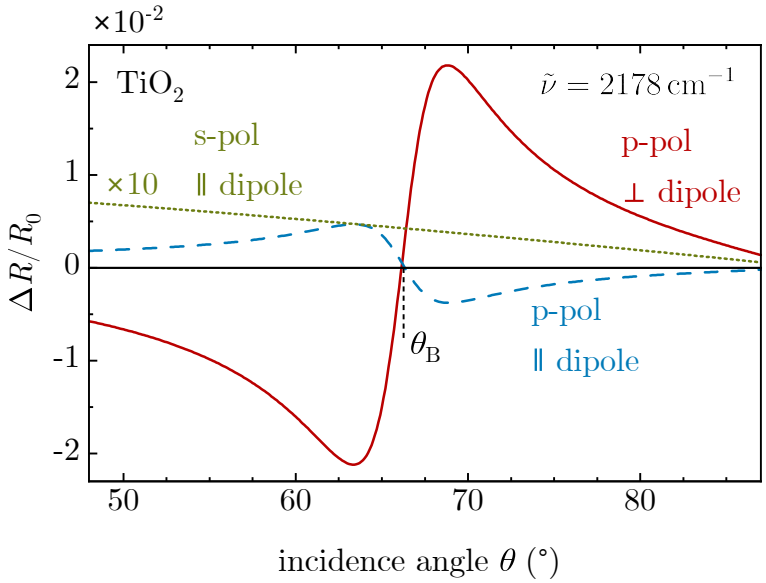

Figure 3.12: Corrected normalised reflectivity difference for an adsorbate on TiO_2 at $\tilde{\nu} = 2178\,\mathrm{cm}^{-1}$ in a system without skew polarisation aberration. The red, solid curve indicates p-polarised light with a dipole moment normal to the surface. The blue, dashed line depicts p-polarisation with a dipole moment parallel to the surface and incidence plane. The dark green, dotted curve indicates s-polarisation with a dipole moment parallel to the surface and perpendicular to the incidence plane. The s-polarised calculation is multiplied by a factor of 10 to enhance clarity. The black (dashed) line indicates the Brewster angle. This figure is adapted from [34].

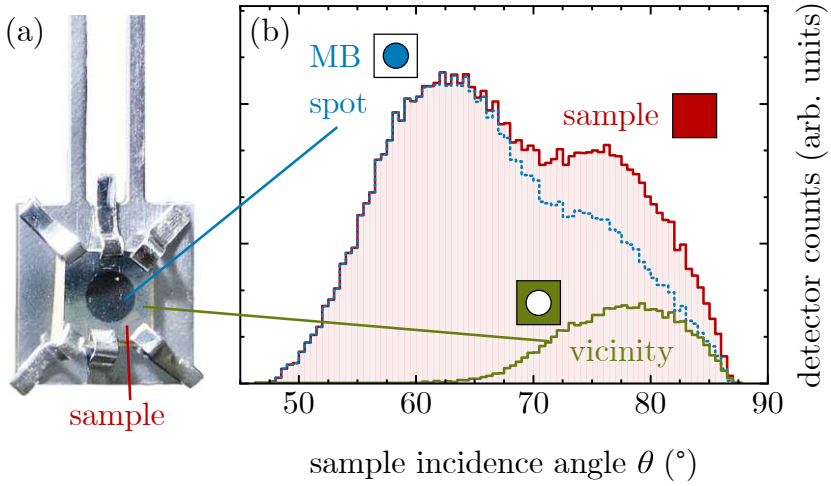

Figure 3.13: Simulated sample intensity. (a) Photograph of the sample and the sample holder. The dark area in the centre of the sample indicates the MB spot (adsorbate-covered area). (b) shows the incidence-angle-dependent intensity on various sample areas: full sample I_{full} (red, solid), MB spot I_{MB} (blue, dotted) and vicinity I_{v} (dark green, solid). This Figure is adapted from [34].

$1/x$-like singularity changes to a continuous curve and decreased peak heights, around the (pseudo-) Brewster angle. Figure 3.12 accounts for a depolarisation of $\Gamma = 0.005$ and an angle spread of $\kappa = \pm 2$ in the real-optical system. Materials with a non-zero absorption coefficient like Fe_3O_4 only exhibit a minor reduction of the peak heights considering the effects from before.

3.3.4 Illumination of Areas without Adsorbate

Besides the effects discussed above, peak heights are also influenced by the geometry of the adsorbate-covered area on the surface in combination with the illumination intensity. The setup presented herein is tailored for examining samples featuring a small adsorbate-covered area in the centre of the sample. In this case, the adsorbates are located in the MB spot, depicted as a dark circular area in Figure 3.13(a). This area is 3.5 mm in diameter. The surrounding area is the vicinity and is adsorbate-free. To understand the decrease in signal intensity attributed to the beam spot, it is important to investigate the illumination intensity of the different areas on the sample.

Figure 3.13(b) shows the simulated incidence angle dependent intensity for rays reflected off the different sample areas reaching the detector. The areas are divided into the MB spot (blue), vicinity (dark green) and full sample (red). A set of rays was traced through the system, and the counts on the detector were recorded with respect to the incidence angle θ onto the sample. To evaluate the incidence angle θ, every ray hitting the surface was projected on the incidence plane. A $6 \times 6\,\text{mm}^2$ sample surface was used in the simulation. The red (solid) curve in Figure 3.13(b) describes the intensity reflected from the full sample area, with incidence angles from 48° to 87°, as shown in

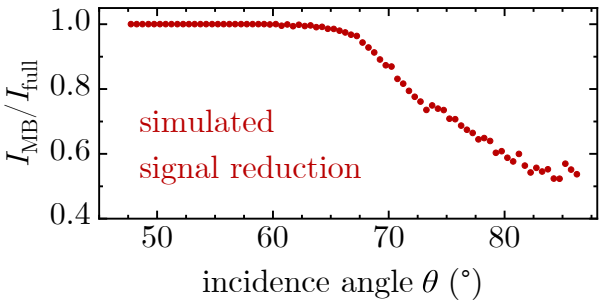

Figure 3.14: Reduction of the signal intensity due to the vicinity illumination in the IRAS measurement range. The plot shows the ratio of the simulated intensities reflected from the MB spot (I_{MB}) and the full sample (I_{full}). The intensities with respect to the incidence angle θ are shown in Figure 3.13(b).

Figure 3.9. Two maxima at 63° and 73° and a local minimum between the maxima are visible. This local minimum is caused by the inhomogeneous intensity distribution of the parallel beam at the spectrometer output (a prism for the HeNe laser obstructs beam path), described in further detail in Ref. [38]. In the first maximum, only the MB spot is illuminated. For angles of incidence less than 65°, the illumination is concentrated in this area due to the illumination-shaping slit (see Figure 3.1), which reduces the vicinity illumination at non-grazing angles to zero. This ensures maximum $\Delta R/R_0$ in the non-grazing region. With increasing θ, the size of the illumination spot increases along the plane of incidence (shown in Figure 3.2), exceeds the MB spot and starts to illuminate the vicinity (dark green, solid curve in Figure 3.13) more and more. The illumination intensity in the vicinity reaches its peak at about 78°. The illumination shaping slit minimises the intensity in the vicinity area. At very grazing angles, vicinity illumination is unavoidable, and up to about 48% of the IR light reaching the detector is reflected from the adsorbate-free area on the sample (see Figure 3.14). Completely restricting the illumination to the MB spot is not possible due to the grazing incidence of the light. A narrower illumination shaping slit would allow to concentrate the light more to the MB spot. However, this would reduce the system throughput, introducing high noise. Note that the illumination of the vicinity affects both polarisations at grazing angles. The current setting of the illumination shaping slit balances between intensity throughput and signal intensity reduction for grazing incidence angles to achieve a good SNR in all cases; for non-grazing and grazing angles. Hence, for measurements at non-grazing angles, the throughput of the system can be further optimised by increasing the width of the illumination shaping slit.

Figure 3.15 shows the effect of the vicinity illumination on the signal intensity. The calculation was performed at $\tilde{\nu}$ = 2178 cm^{-1} on the TiO_2 surface with an adsorbate defined in Section 2.4.2. The solid curves indicate the ideal case, and the dashed lines include the correction of the vicinity illumination. All three main cases are presented in the plot: s-polarisation with a surface-parallel dipole moment perpendicular to the incidence plane (s$\parallel$, dark green), and p polarisation with the dipole moment normal (p$\perp$, red) and parallel (p$\parallel$, blue) to the surface, both in the plane of incidence. To

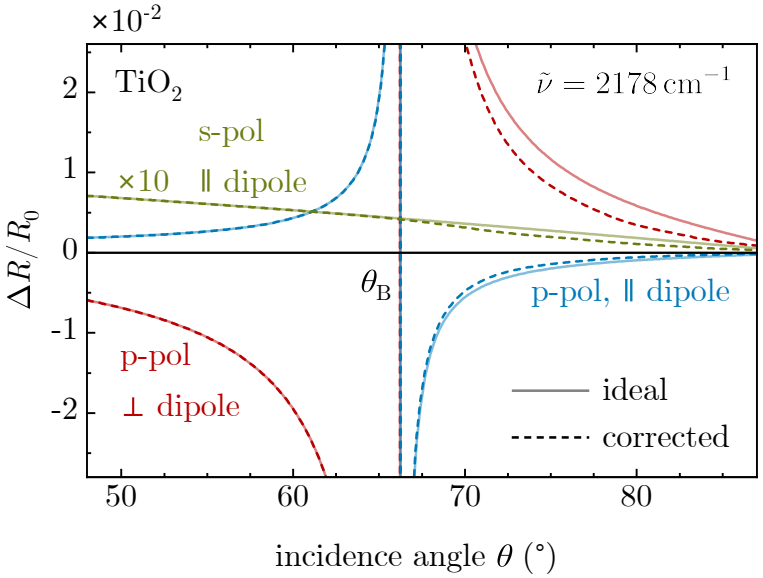

Figure 3.15: Influence of the sample illumination on the normalised reflectivity difference $\Delta R/R_0$. The plot shows the ideal $\Delta R/R_0$ and the influence of the vicinity illumination on $\Delta R/R_0$. The data are for TiO_2 at $\tilde{\nu}$= 2178 cm^{-1}, for p-polarisation and dipole moment normal to the surface (red), p-polarisation and a dipole moment parallel to the surface (blue) and s-polarisation with the dipole moment (dark green) parallel to the surface. The s-polarised curve is multiplied by 10 for clarity. θ_B indicates the Brewster angle.

consider the vicinity illumination in the calculation, $\Delta R/R_0$ was multiplied by the ratio of the intensities reflected from the MB spot and the full sample I_{MB}/I_{full}, shown in Figure 3.14. Fits of the angle-dependent intensities plotted in Figure 3.13, were used to include the angle-dependent reflectivity in the calculation. For angles lower than 65°, high similarity to the ideal case is observed as the illumination-shaping slit prevents the illumination of the vicinity. This can also be seen in Figure 3.14. At higher incidence angles ($\theta > 65°$), the illumination of the vicinity grows with increasing incidence angle θ, reducing the signal intensities in this range by almost 50 % at very grazing angles. This shows the importance of the illumination-shaping slit controlling the illumination on the sample and the additional complication arising from a small adsorbate area.

To further reduce the influence of vicinity illumination at grazing angles, the surface normal of the sample can be rotated when dosing the gas, such the MB spot is not circular but elliptical on the sample. This enlarges the adsorbate-covered area on the surface, and enhances the signal intensities. However, the coverage homogeneity of the adsorbate-covered is reduced by this method.

3.3.5 Combined Effects for the IRAS Setup

This section illustrates the effects occurring in the presented IRAS system affecting $\Delta R/R_0$. Before, it was shown that depolarisation and angle spread decreased the reach-

able signal intensities. The angle spread impacts the signal intensities, mainly when the measurement angle range exceeds the Brewster angle, leading to simultaneous measurement of positive and negative peaks. Restricting the incidence angle range with the angle-selection plates to one side of the Brewster decreases the influence of this effect. Contrarily, depolarisation also occurs for very restricted angle ranges and is stronger than the angle spread. Due to the strong influence of the depolarisation and the result shown in Figure 3.4, it cannot be neglected in the calculation of $\Delta R/R_0$. At grazing angles, also the vicinity illumination has to be considered.

Figure 3.16 shows the normalised reflectivity difference $\Delta R/R_0$ on TiO_2 for an angle spread of $\kappa = \pm 2°$ (see Section 3.3.2), the system specific depolarisation of $\Gamma = 0.21$ by the "leakage" of s- or p-polarised light from the clean surface, evaluated by simulation (see Section 3.3.1) and the vicinity illumination discussed in Section 3.3.4. The magnitude of the peak height for p polarisation and a perpendicular oriented dipole moment arises at low incidence angles in the non-grazing range below the zero-crossing. The maximum peak height above the zero-crossing is slightly smaller. This is caused by the reduction of the signal intensity in the range from $\theta = 64°$ to $\theta_{\max}$ due to the vicinity illumination. The exact values are tabulated in Table 3.5. On average, the signal intensity in the non-grazing range from $\theta_{\min}$ up to the zero-crossing (negative part of the curve) is higher than in the grazing range (positive part of the curve). Therefore, higher signals are expected in the non-grazing range, confirmed by the characterisation measurements in Section 5.3. Also, for p polarisation and a parallel dipole moment (blue, dashed curve) the non-grazing range is predicted to deliver larger peak heights. Also, s-polarised signals (dark green, dotted) show larger peak heights at non-grazing angles.

Compared to the minimal corrections depicted in Figure 3.12, the maximal possible peak heights for p polarisation decrease by about one order of magnitude. Furthermore, the extrema for p-polarised $\Delta R/R_0$ shift further away from the Brewster angle than in the case with minimal corrections. This leads to a shallower slope of the $\Delta R/R_0$ curve at the zero-crossing, influencing the ideal angle range setting for the angle-selection plates. Due to the shallower slope, the impact of angle spread is weaker, and the depolarisation and vicinity illumination dominate.

The normalised reflectivity difference $\Delta R/R_0$ on Fe_3O_4 for an angle spread of $\kappa = \pm 2°$ (see Section 3.3.2), the system specific depolarisation of $\Gamma = 0.21$ and the vicinity illumination is shown in the appendix A.1.2. Here, the pseudo-Brewster angle is at higher angles of incidence than on TiO_2, thus also here the preferred measurement range is in the non-grazing range for p-polarised signals.

3.3.6 Summary

A solid design framework is essential for a well-designed system. Identifying the key design parameters beforehand is crucial for optimising a system. Two factors must be considered when IRAS is used on non-metallic substrates. The first factor is the intensity throughput of the system, which directly influences the noise characteristics in the

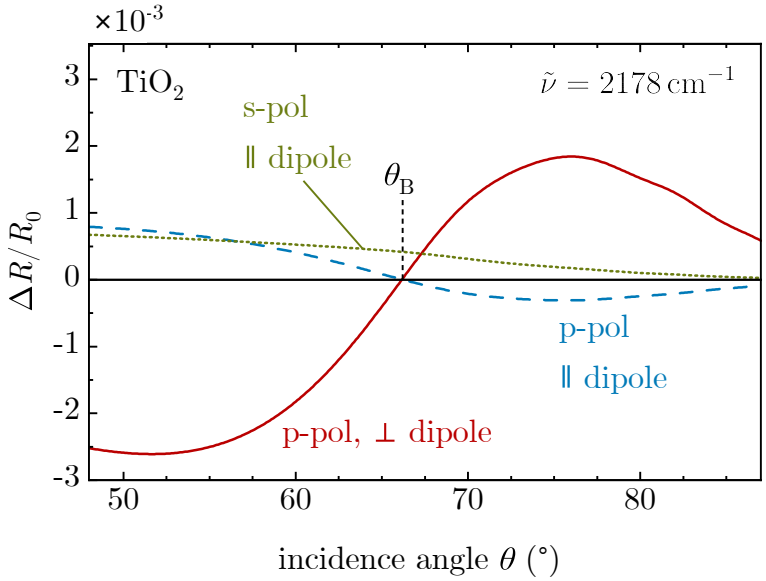

Figure 3.16: Normalised reflectivity difference for an adsorbate on TiO_2 at $\tilde{\nu} = 2178\,\mathrm{cm}^{-1}$ with the combined corrections for the IRAS setup. These are $\Gamma = 0.21$, $\kappa = \pm 2°$ and the effect of the vicinity illumination. P polarisation with a dipole moment normal to the surface (red, solid), p-polarisation with a surface-parallel dipole (blue, dashed) and s-polarisation with a parallel dipole moment orientation (dark green, dotted). The black (dashed) line indicates the Brewster angle (the zero crossings for p polarisation).

curve	$\Delta R/R_{0,\max}$	$\theta_{\max}$ (°)	$\Delta R/R_{0,\min}$	$\theta_{\min}$ (°)	$\Delta R/R_0(57.1°)$	$\Delta R/R_0(76.6°)$
p ⊥	1.84×10^{-3}	76	-2.61×10^{-3}	51.6	-2.31×10^{-3}	1.83×10^{-3}
p ∥	7.92×10^{-4}	48	-3.1×10^{-4}	75.6	5.51×10^{-4}	-3.06×10^{-4}
s ∥	6.7×10^{-4}	48	2.74×10^{-5}	87	5.66×10^{-4}	1.63×10^{-4}

Table 3.5: Collection of the system specific $\Delta R/R_0$ values for p- and s polarisation and parallel or perpendicular dipole moment orientation. The values are evaluated from Figure 3.16. The table shows the maximum and minimum values of the incidence angle dependent $\Delta R/R_0$ for a TiO_2 surface with an adsorbate defined in Section 2.4.2 and the system-specific corrections applied. These are $\Gamma = 0.21$, $\kappa = \pm 2°$ and the effect of the vicinity illumination. Furthermore, the expected signal intensities at 57.1° and 76.6° are tabulated, marking the half-point between the measurement limit and θ_B on each side of θ_B.

measurements. A higher intensity reduces noise and is largely influenced by the optical design. The second factor involves understanding the specific signal behaviour on non-metallic substrates originating from the low reflected p-intensity at the Brewster angle and the effect of band inversion. Additionally, various factors, such as depolarisation of light, angle spread, and the illumination of adsorbate-free sample areas, must be considered; all of which typically occur in real optical systems. These effects reduce

the maximum peak intensities and impact the optimised IRAS measurement ranges compared to the ideal signal intensity behaviour.

CHAPTER 4

REALISATION

The realisation of the IRAS design necessitated considering several critical parameters at the outset, including the investigation of the underlying theory to identify the essential parameters for the optical design, the careful optimisation of the optical system and the boundary conditions given by the existing surface analysis chamber. This established the foundation for the mechanical design of the system to create a measurement system that achieves high SNRs on non-metallic sample substrate materials with small areas of adsorbates. Also, the mechanical stability of the system is a critical point to consider, as it enhances optical alignment stability within two consecutive measurements and over long periods.

During the initial development phase of the 3D design, minor adjustments were made to the optical design to accommodate the spatial restrictions of the chamber itself and the purchased components incorporated in the design. The purchased components were selected to ensure optimal performance, compact size and vacuum compatibility. After this, the 3D design was finalised, and the technical production drawings were prepared. These drawings specify the dimensions, maximum tolerances and the material of the parts. An overview of materials applicable in the vacuum can be found in Ref. [75]. Additionally, sensitivity checks of the optical system were performed to identify the necessary precision of the mechanical parts. According to this, the tolerances on the technical drawings were chosen. The manufacturing of the parts was carried out in-house and by external companies. Before the assembly, the critical dimensions of the

individual components were measured. This was also done for parts of the assembled system to ensure the position of the optical elements before the complete assembly and the installation of the IRAS system. Parts of the chapter can be found in [34].

4.1 Surface Chemistry Chamber

The existing surface chemistry chamber [62, 63] was one of the constraints influencing the design of the IRAS system. It is used to study surface reactions under ultra-high vacuum (UHV) conditions in a base pressure of about 5×10^{-11} mbar. It consists of one main chamber with two levels of the sample position, where all the measurement and preparation techniques are located.

The investigated single crystal samples are held in place with Ta clips on a Ta sample plate fixed on a liquid helium flow cryostat. With this setup, sample temperatures down to 30 K are possible. A gold foil between the sample and the sample plate ensures good thermal contact. The cryostat sits on a manipulator, allowing sample rotations through 360° and x-, y-, and z-movements. A custom-made molecular beam (MB) source doses molecules onto the surface, creating an adsorbate area, with 3.5 mm in diameter, on the sample surface. In combination with a mass spectrometer, temperature-programmed desorption (TPD) measurements can be performed. Additional surface characterisation techniques like low-energy ion scattering (LEIS), ultraviolet photoelectron spectroscopy (UPS) and x-ray photoelectron spectroscopy (XPS) are used to characterise the sample surfaces and adsorbed species. A sputter gun, generating Ne^+ ions, is used to prepare and clean the sample. Furthermore, the sample can be heated to a maximum temperature of about 1100 K and a tube doser is used for oxidative annealing cycles. The mounted metal evaporators are calibrated with a quartz crystal microbalance (QCM) and are used to dose different types of metals onto the surface. The whole vacuum chamber is pumped with five turbo molecular pumps and four rotary pumps acting as fore-pumps.

The newly developed IRAS setup upgrades the UHV surface chemistry chamber with an additional technique for adsorbate characterisation. The new measurement system integrates a commercial Bruker VERTEX 80v FTIR spectrometer and the custom-built IRAS unit into the existing surface chemistry chamber. It provides an additional layer of information for surface reaction studies.

The dimensions and positions of the measurement techniques on the UHV chamber heavily influenced the design of the IRAS system. The main goal was to implement a system with high throughput and optimised sample illumination. Additionally, also the user-friendliness of the chamber itself was improved.

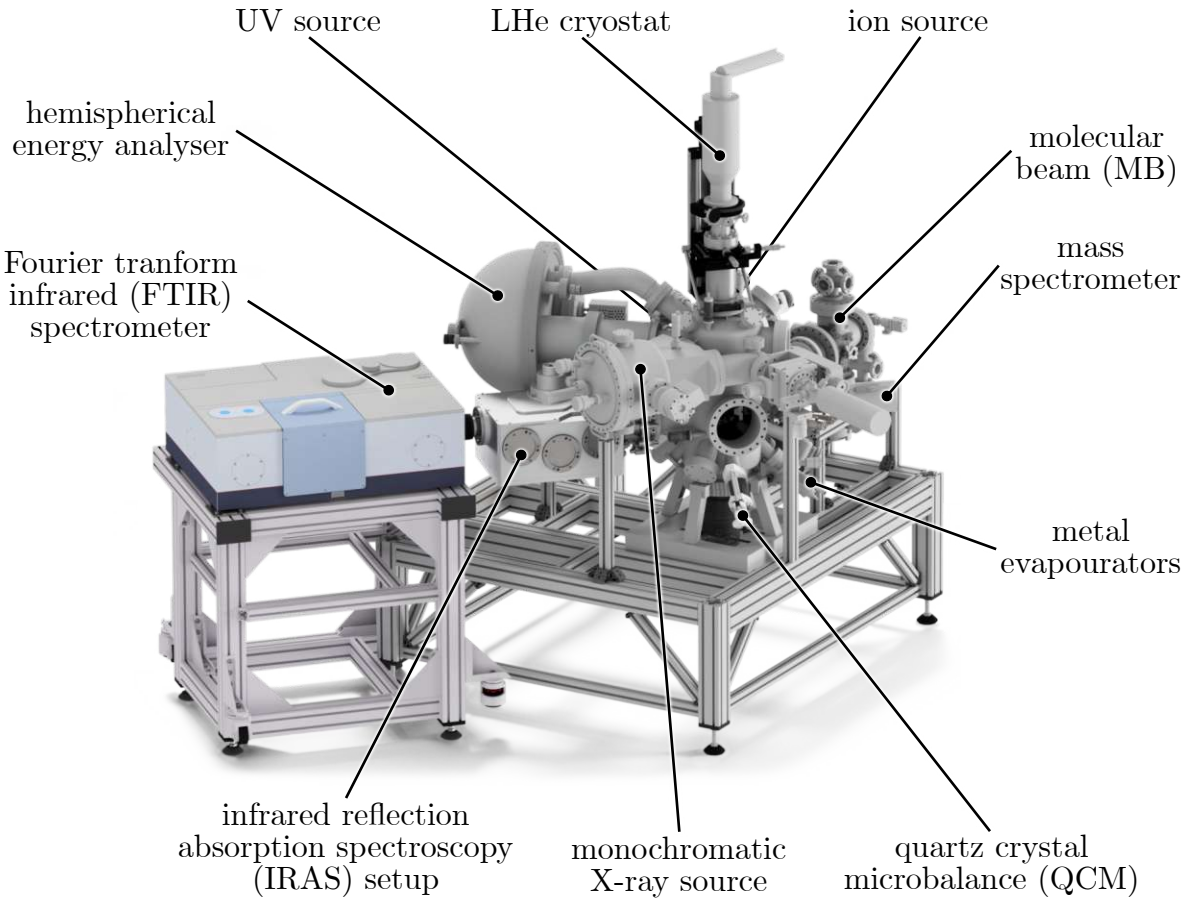

Figure 4.1: 3D visualisation of the UHV surface chemistry chamber and the IRAS setup. The chamber features a base pressure of about 5×10^{-11} mbar and incorporates multiple analytical techniques: X-ray electron spectroscopy (XPS) with a monochromatic X-ray source, low energy ion scattering (LEIS), temperature programmed desorption (TPD) with the combination of the mass spectrometer and the molecular beam (MB), and ultraviolet photoelectron spectroscopy (UPS). A liquid helium (LHe) cryostat allows sample temperatures down to 30 K. An ion source (for sputtering), metal evaporators, gas lines with various gases and the molecular beam can be utilised for sample preparation.

4.2 Mechanical Design

The surface chemistry chamber, specifically the molecular beam, the mass spectrometer, and the port positions greatly influenced the design as they restricted the placement of the mirrors inside the chamber. These spatial parameters also influenced the coupling of the IR beam in and out of the chamber. Furthermore, other techniques on the chamber, like the XPS analyser, the XPS monochromator or the room size, restricted the design (see Figure 4.1). It was essential to utilise a minimum amount of flanges during the design to implement the IRAS setup. Besides these challenges and the consideration of the parameters for optimal optical throughput and light incidence angle, focus was also put on the stability of the system. The stability of the optical system and the stability of the mechanical platform are interlinked and influenced by several parameters: environmental vibrations (e.g., from vacuum pumps), sample vibrations, temperature stability of the room, or tilt errors of the sample mounted on a cryostat [38]. Considering these points, the optical alignment can be maintained, leading to more equal baselines of consecutive measurements (spectral stability), and long-term performance is given by keeping the throughput without a realignment of the optical system. This also contributes to the user-friendliness of the IRAS system.

A key design element to ensure stability is that all important optical components are precisely connected to one central flange (see Figure 4.2). The precise connection is realised by fits or milled corner joints between the components and pinned fittings for optical elements. The majority of the screwing connections are spring-loaded or utilise retaining washers to keep the parts securely in place, also during thermal cycles, i.e., bakeouts at 150 °C. To prohibit cold welding in threaded connections, a graphite-Milli-Q (ultrapure water) solution was applied to screws and threaded rods before assembly.

Figure 4.2 shows a partial section view of the IRAS setup. It can be split into a high vacuum part enclosed by the high-vacuum box and a UHV part, inside the UHV surface chemistry chamber. The detection platform and its optics are located in the high-vacuum box. The pressure here is $\approx 1 \times 10^{-4}$ mbar or lower. This high-vacuum box connects the UHV surface analysis chamber with the FTIR spectrometer and is pumped with a turbomolecular pump. The pressure in the spectrometer during operation is about 1 mbar. Most flange connections on the high-vacuum box are realised with DN 63 ISO-K connections and a modified bolt ring. This bolt ring utilises six M4 screws instead of the four standard screws usually used for DN 63 ISO-K flanges. The modification was necessary to react to the limited wall thickness of the high-vacuum box. Additionally, the threads in the high-vacuum box are strengthened with Helicoil thread insets to protect the weaker aluminium threads. The whole box is made from aluminium of the type EN AW-6061-T6. A window adapter, made from EN AW-6082-T6, on the spectrometer exit flange, holds a 3.5 mm thick wedged BaF_2 window (⌀55 mm). Two O-rings on each flat optical surface and a screwed clamp hold the window in place, separating the spectrometer from the high-vacuum box. The O-ring compression is 20%. The thicker part of the window is at the top of the window adapter, indicated by

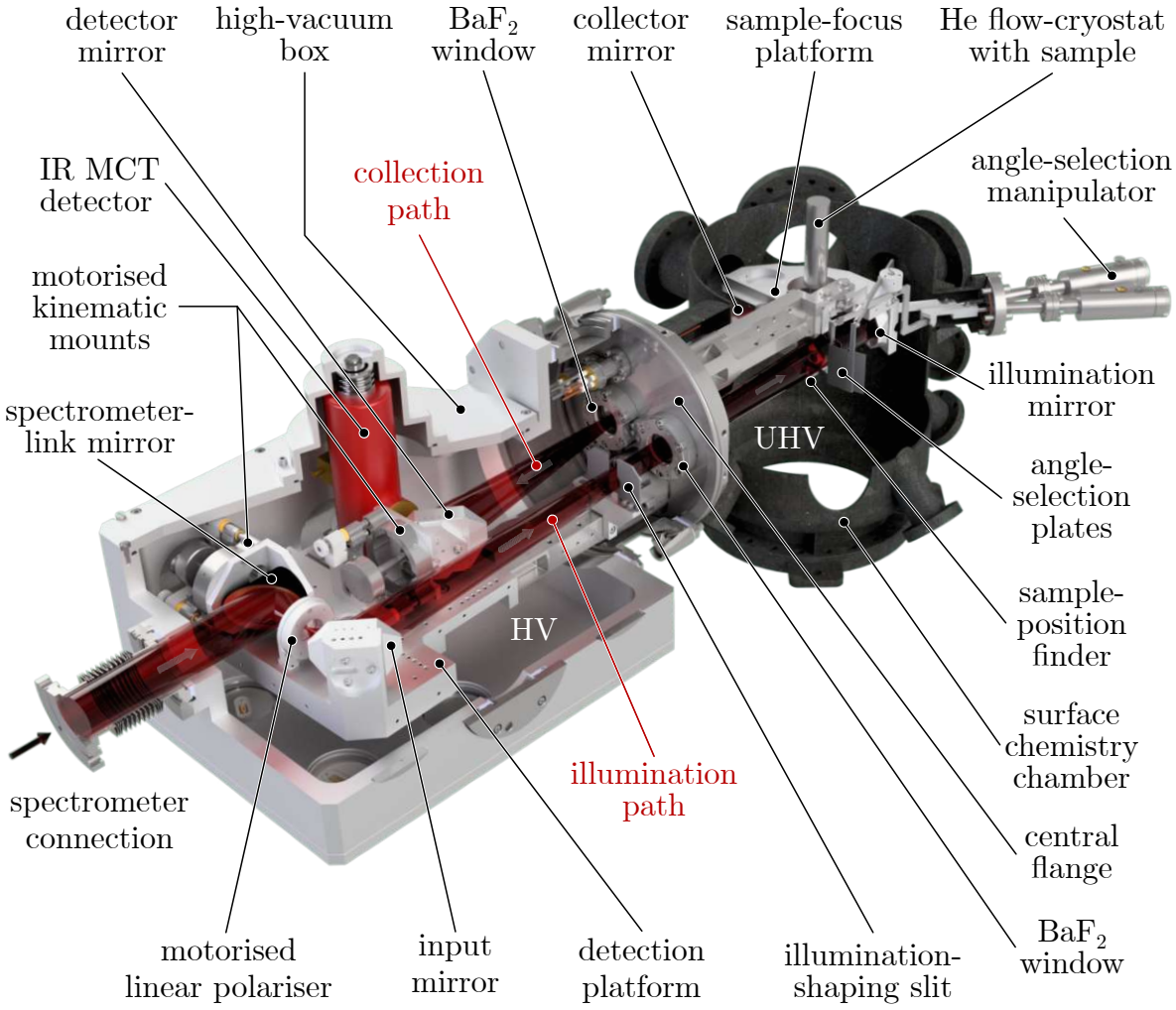

Figure 4.2: 3D visualisation of the IRAS system. The components of the IRAS system are shown. The main parts are the detector platform in the HV box, the sample focus platform in the UHV surface chemistry chamber, and the central flange separating the two pressure regimes. The IR beam through the system is visualised in red. This figure is adapted from [34].

a scratch mark. Note that the IR beam exiting the spectrometer is slightly deflected up after transmission through the wedged window when the thicker part of the window is on top.

Figure 4.1 shows the spectrometer on a stable rack, which allows height adjustments of the spectrometer and spectrometer shifts along the short edge of the spectrometer by adjusting screws. Furthermore, the rack is placed on vibration dampers made from stainless steel wire. The spectrometer-box connection is realised with a DN 63 ISO-K edge welded bellows, as seen on the left side in Figure 4.2. One side connects to the window adapter, and the second connects to the box. The bellows compensates for distance tolerances and the 2.4° tilt between the spectrometer and the box. Also, it reduces the transfer of vibrations from the box to the spectrometer. The two sidewalls of the box, not facing the spectrometer or the chamber, feature five DN 63 ISO-K flange connections for future extensions. On the flange behind the MCT detector, two double-sided SMA coaxial feedthroughs are placed to connect the detector electronics, separated from the detector. Usually, the detector electronics is mounted directly to the underside in the standard detector configuration.

The top and bottom of the box are sealed with Viton O-rings. These O-rings are held in place by a dovetail-shaped groove. The special shape of the grooves keeps the O-ring in place when the covers are not mounted. The top groove utilises a 360 × 4 (inner diameter in mm × cross section diameter in mm) big O-ring made from the compound Vi 564 (FKM 70). A 394 × 4 sized O-ring from the same material is placed in the bottom grove. Additional lubrication with Krytox LVP grease improves the sealing. The O-ring compression is 20 %. The bottom cover features five DN 63 ISO-K flanges for electrical feedthroughs. Two are used for the motorised kinematic mounts, thermocouples, and the heating system. One of these flanges is connected to water cooling, which keeps the detection block below 60 °C during the bakeout. Copper braids connect the HV support beam to the cooling flange. The detector protrudes through the top cover. Therefore, a custom-made tube is required to seal the box utilising an O-ring (132 × 3, made from Viton, 20 % compression). Around the tube, the thickness of the cover is increased to enhance the stability of the top cover under evacuation and avoid misalignment of the detector. On the UHV-chamber-facing side of the box, a DN 200 ISO-K tube with 200 mm length connects the high-vacuum box to the central flange.

In the following sections, the circled numbers in the figures indicate the different components of the assemblies, which will be referenced as "# part number" in the text, e.g., #11 for the central flange (see Figure 4.3 and Table 4.1). Additionally, boxed letters specify the critical reference surfaces. In the text, they are indicated by a □ before the letter, e.g. □A.

4.2.1 Core Part Assembly – Central Flange

The central flange of the IRAS system is the heart of the mechanical design. It separates the two pressure regimes, high vacuum and UHV, and allows the IR beam to enter and

exit the surface analysis chamber through two windows. Two stainless steel support beams extend from the flange into the high vacuum and UHV. Each stainless steel beam supports an optical platform, described in Section 4.2.2 and 4.2.3. The centralised flange design enables a precise and reliable connection between components in the high vacuum and UHV regime, ensuring the optical alignment. Figure 4.3 shows a 3D representation of the core part assembly of the IRAS system, including the central flange (#11). The component names are referenced in Table 4.1. The important reference surfaces are collected in Table 4.2.

On the very top of the central flange (#11), which is made from stainless steel of type 1.4301, the levelling platform (#5) is fixed. This platform represents the main reference surface □A of the IRAS setup. It allows the levelling of the complete system after assembly. The two optical platforms are levelled with this reference surface within an error of less than ±0.2°. Furthermore, it is always accessible because it is outside of the vacuum. Two DN 16 CF feedthroughs are mounted below the levelling platform on the front surface of the central flange. This part is in a high vacuum. On the type K thermocouple feedthrough (#2), one thermocouple measures the temperature at the end of the UHV support beam (#9) close to the sample focus platform. The other thermocouple measures the temperature on the sample focus platform. The second feedthrough features one type K thermocouple connection and a current feedthrough rated for 16 A and 1 kV (#3). The current feedthrough is connected to the heating system (#8) of the UHV support beam.

Two modified DN 40 CF window flanges (#4) hold wedged BaF_2 windows, pressed against a Viton O-ring with a spring-loaded clamp. To account for the wedge on the window, a wedged stainless steel ring is placed between the clamp and the window to ensure an equal compression of 20% of the O-ring. A ring-shaped Kapton foil is in between the window and the wedged ring to protect the window from the sharp edges of the metal ring. The window in the illumination path (see Figure 3.1) has its thick part at the bottom, and the window in the collection path is oriented with the thick part on top. This compensates for the deflection of the IR beam when it passes through the wedged window. The windows are designed with a clear aperture of 34 mm. A DN 16 CF blank flange (#6) is above the two window flanges. Behind this flange, a hole goes through the UHV beam and the sample-focus platform (see Section 4.2.3), providing access to the sample-pass hole in the sample-focus platform if necessary.

Before the window in the illumination beam, two aperture plates (#12 and #13, highlighted in blue) form the 10 mm wide illumination-shaping slit. Manual adjustments, guided by the illumination-shaping support (#14), shift the plates into and out of the beam (indicated by the dark blue arrows on the plates). This enables a precise shaping of the illumination area on the sample. The illumination-shaping plate on the right (#12), depicted in Figure 4.3, alters the sample illumination on the left side (refer to Figure 3.2). This side of the sample is closer to the illumination mirror. The right edge of this plate extends 6.5 mm beyond the illumination-shaping support. The

left illumination-shaping plate (#13) affects the right side of the sample illumination, which is closer to the collector mirror. The illumination-shaping plates are secured to the illumination-shaping support (#14) using spring-loaded screws. This support features additional holes to ensure compatibility with future upgrades to the IRAS setup. Both plates are covered in a low-IR-reflectance black-coated aluminium foil (Acktar Metal Velvet Black Foil) to avoid reflections. To the left of the illumination-shaping slit, the stray light shield (#1) prevents stray light from being detected inside the high-vacuum box. It is made from a IR absorbing black coated steel foil (Lambertian Black™ Foil).

On the very bottom of the central flange, the high vacuum support beam (#15) (in grey) is fixed with spring-loaded screws in a slightly recessed cut-out to define its position precisely. This support beam is made from stainless steel of type 1.4301 and features a reduced cross-section area to minimise thermal conduction. The reference surface □E on top of the high vacuum support beam is parallel to □A. The detection platform is mounted to the high vacuum support beam with a milled corner joint. The three reference surfaces □D ensure a precise and reproducible mounting and define the position of the detection platform □F (see Figure 4.4).

The UHV support beam (#7) is fixed in a recessed cut-out on the back side of the central flange by six spring-loaded screws. The reference surface □B is parallel to the reference surface □A. The support beam is made from stainless steel with the material specification 1.4435. This steel is characterised by its low permeability, thus avoiding magnetic fields inside the chamber. A heating system (#8) is installed to heat the mirror block in case molecules adsorb on the illumination or collector mirror (see Figure 4.5; #30, #34). At the end of the UHV support beam, the sample focus platform (see Figure 4.5) slides over the positioning pin (#9) into the milled corner joint (reference surfaces □C). The sample-focus platform is precisely and reproducibly pressed against the three reference surfaces with spring-loaded screws.

4.2.2 Detection Platform

The detection platform is a single part of aluminium (EN AW-6061-T6) supporting optical components and the detector. Here, the light from the FTIR spectrometer exit gets polarised, is coupled into the measuring chamber and guided from the measurement chamber to the detector. The rigid platform features precise pin mounts and milled corner joints for fixing the kinematic mounts and the platform to the high vacuum support beam. Furthermore, an adjustable detector mount is incorporated into the design. All mirrors utilise a pin mount and fastening with threaded rods, disc spring washers and nuts (shown differently for the spectrometer-link mirror #17 in Figure 4.4). The detection platform is designed with additional mounting points on the top, sides and underside, thus ensuring compatibility of the design with potential future upgrades. Figure 4.4 shows a 3D representation of the detection platform and its components. These components are cross-referenced with Table 4.3. Furthermore, the coloured arrows represent the degrees of adjustment freedom.

part number	part name
1	stray light shield
2	thermocouple feedthrough
3	current and thermocouple feedthrough
4	IR window flange
5	levelling platform
6	cover flange
7	UHV support beam
8	heating system
9	positioning pin
10	BaF_2 window
11	central flange
12	right illumination-shaping plate
13	left illumination-shaping plate
14	illumination-shaping support
15	high vacuum support beam

Table 4.1: Part list of the core part assembly of the IRAS system shown in Figure 4.3.

reference surface	reference surface description
A	central flange levelling surface
B	UHV support beam levelling surface
C	milled corner joint for the sample-focus platform
D	milled corner joint for the detection platform
E	high vacuum support beam levelling surface surface

Table 4.2: Reference surfaces of the core parts of the IRAS system shown in Figure 4.3.

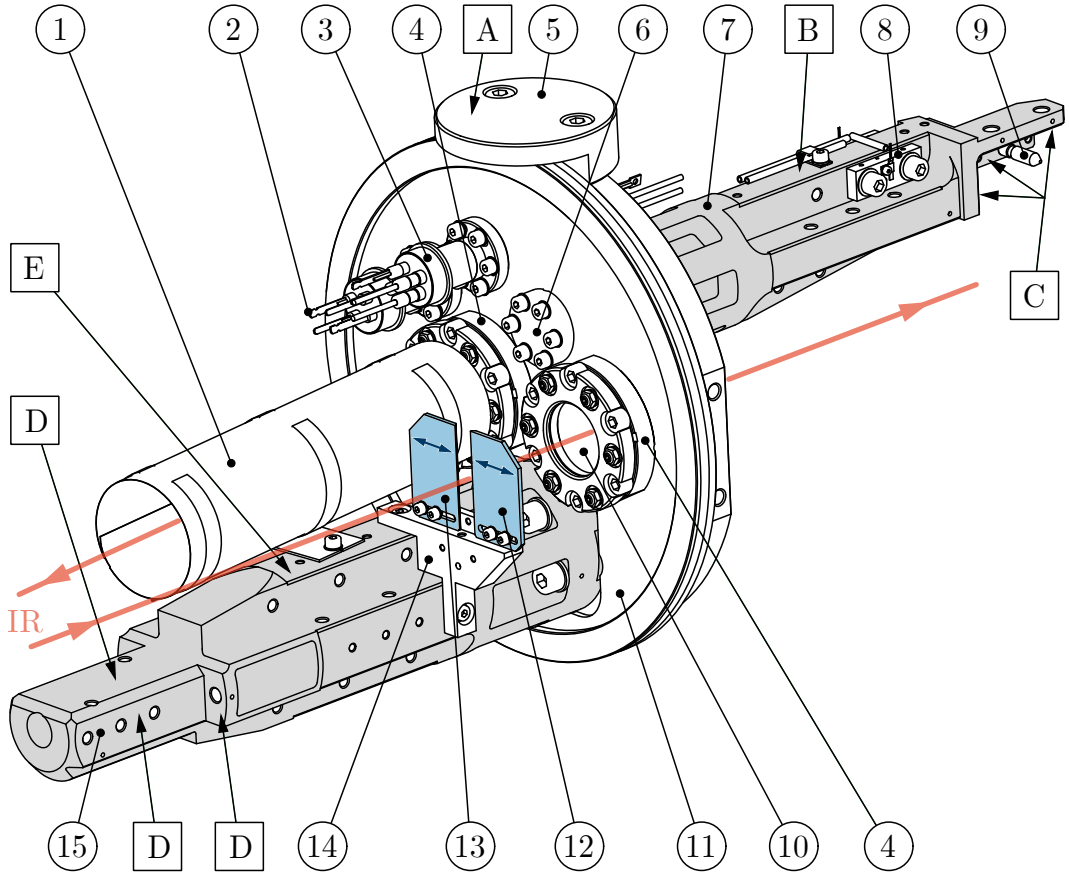

Figure 4.3: 3D representation of the core part assembly with the central flange (#11). The circled numbers are the part numbers (see Table 4.1), and the boxed letters define the reference surfaces (see Table 4.2). The illumination-shaping slit is indicated in blue. Double arrows show the degree of freedom of the aperture plates. The semi-transparent red line indicates the IR beam path and light direction through the system.

On the detection platform (#27), two adjustable mirrors are placed: the spectrometer-link mirror (purple, #17) and the detector mirror (blue, #25). Each of these mirrors is attached via an adapter piece to a motorised kinematic mount (New Focus 8822-AC-UHV, #18), providing two degrees of freedom and tilts of ±5°, as indicated with the purple and blue arrows in Figure 4.4. The kinematic mounts are secured in milled corner joints using spring-loaded screws. It is important to note that the two L-brackets of the kinematic mounts are 10 mm apart, which is different from the original delivery state. Adjusting the spectrometer-link mirror (purple, #17) changes the illumination on the sample from its central position upwards, downwards, to the left, or right. However, it is crucial to avoid over-adjusting the mirror, as this degrades the system performance. At the end of the beam path, adjusting the detector mirror (blue, #25) makes it possible to move the focal spot on the detector to its optimal position. This has to be done in conjunction with the alignment of the detector (red, #19) because the focusing cone angle of the detector mirror has to fit the light acceptance angle of the detector.

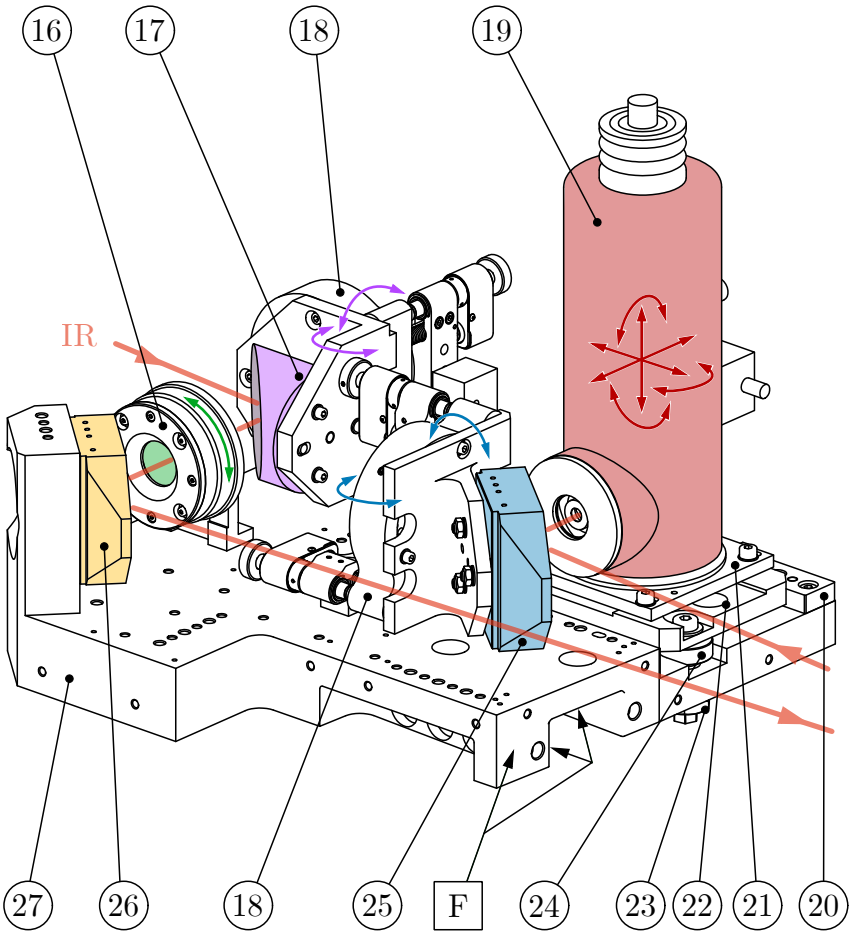

Figure 4.4: 3D visualisation of the detection platform. The circled numbers are the part numbers (see Table 4.3), and the boxed letters define the reference surfaces. Important optical components are highlighted in colour. The colour-matched arrows indicate the degrees of freedom of the components, which allows the alignment of the optics. The semi-transparent red line indicates the IR beam path and light direction through the IRAS system.

Therefore, the detector is mounted on a manually adjustable detector plate stack consisting of the detector base plate (#21) and the detector adjustment plate (#22) made from EN AW-6082-T6 aluminium. The detector base plate was already mounted to the detector after purchase. Linear adjustments along the optical axis of the detector by ±5 mm are possible by loosening the four screws holding the detector base plate. The detector adjustment plate (#22) allows movements parallel to the detection platform surface in the range of ±1.2 mm without any directional limits within the plane. Therefore, rotations of the detector around the centre axis of the dewar are possible (±1°). The detector adjustment plate is placed on three height adjusters (#24) made from stainless steel of type 1.4301. These height adjusters reduce the thermal conductivity from the platform to the detector and enable lifting the detector by up to 5 mm. For adjustment, the three screws holding the detector adjustment platform and the counter

part number	part name
16	rotatable polariser
17	spectrometer-link mirror
18	2-axis kinematic mount
19	MCT detector
20	position-definer
21	detector base plate
22	detector adjustment plate
23	counter nut for height adjuster
24	height adjuster
25	detector mirror
26	input mirror
27	detection platform

Table 4.3: Part list of the detection platform assembly of the IRAS system shown in Figure 4.4.

nuts (#23) on the underside of the detection platform have to be loose. Then they can be screwed up and down. The detector can also be slightly tilted by setting the three height adjusters to different heights. This flexibility in adjustment facilitates a good alignment of the detector with respect to the incoming IR beam.

To remove the detector, including the detector plate stack, the three spring-loaded screws holding the detector adjustment plate in place have to be removed, and the two cables for the detector signal and the temperature measurement of the cold finger disconnected. A position-definer (#20) enables a reproducible and precise remounting of the detector after it is aligned.

The input mirror, highlighted in yellow (#26), is mounted directly to the detection platform with no adjustment possible. Between this mirror and the spectrometer-link mirror (purple), a holographic wire grid polariser (marked in green) is mounted to the motorised rotation stage SR-5714 from SmarAct (#16) with an angular resolution better than 0.1°. This rotatable polariser is fixed with two screws, and pins define its position.

The detection platform is designed such that the complete assembly of the detection platform, shown in Figure 4.4, can be removed from the core assembly. The connection of the detection platform and the core assembly is realised with a milled corner joint, seven spring-loaded screws and two custom threaded insets. The three reference surfaces □F on the detection platform, and the reference surfaces □D on the high vacuum support beam (shown in Figure 4.3) define the connection.

4.2.3 Sample-Focus Platform

The sample focus platform provides the mechanical platform for the optics in the UHV chamber to direct the IR light from the high-vacuum box onto the sample, collect it, and guide it out of the chamber. Furthermore, it holds the sample-position finder and the mechanism for selecting the incidence angle range of the light onto the sample. Another function of the sample-focus platform is to protect the mirrors from sputter derbies from the top level and evaporated metal. Figure 4.5 shows a 3D representation of the sample-focus platform and its components. The Figure also shows the UHV support beam (see Figure 4.3) visualised in grey lines. The component names are tabulated in Table 4.4.

The sample-focus platform holds the illumination mirror (dark red, #30) and the collector mirror (dark yellow, #34). The platform is made from EN AW-6061-T6 aluminium. Both mirrors utilise a pin mount, three threaded rods per mirror, disc springs, and nuts to secure them. These mirrors are fixed and cannot be adjusted. A 60 mm diameter central hole in the sample-focus platform provides a pass-through to the IRAS measurement position for the sample (#33). This results in a clearance of 15 mm between the sample pass hole and the centrally in the hole positioned cryostat. The sample-position finder (grey, #32) is located below the sample. This optical device enables the user to read the sample position. Further details are described in Section 4.2.3. To the right of the sample-position finder, a metal evaporator shield (#31) made from Cu protects the mirrors from being covered by the evaporated metals in the UHV chamber. An additional assembly interface, indicated by the reference surfaces □I, is used to mount the angle-selection mechanism described in Section 4.2.3.

Like the detection platform, the sample-focus platform, as seen in Figure 4.5, can be assembled independently from the core assembly. To mount it to the core assembly, the sample-focus platform is pushed over the positioning pin (#9) into the milled corner joint of the UHV support beam (#7) through a DN 150 CF port. This can be done one-handed. After sliding the platform into position, it hangs securely in place without needing support. This design feature facilitates the installation of the sample-focus platform inside the UHV vacuum chamber, as it needs to be installed when the core assembly is mounted to the chamber. The core assembly with the sample-focus platform attached does not fit through the DN 150 CF port of the vacuum chamber. The connection is defined by the three reference surfaces □C on the UHV beam (see Figure 4.3) and three reference surfaces □G on the sample-focus platform. In Figure 4.5, one reference surface □G is hidden on the backside of the sample-focus platform. To make the installation on the UHV chamber possible, the whole sample focus platform (except the Cu shield) is designed to fit sideways through a DN 150 CF flange. Three spring-loaded screws (disc springs) and a nut are utilised to secure the sample-focus platform precisely in place. Two custom threaded insets (#28) replace the aluminium thread in the sample-focus platform with a stainless steel thread to enhance the strength and durability of the connection.

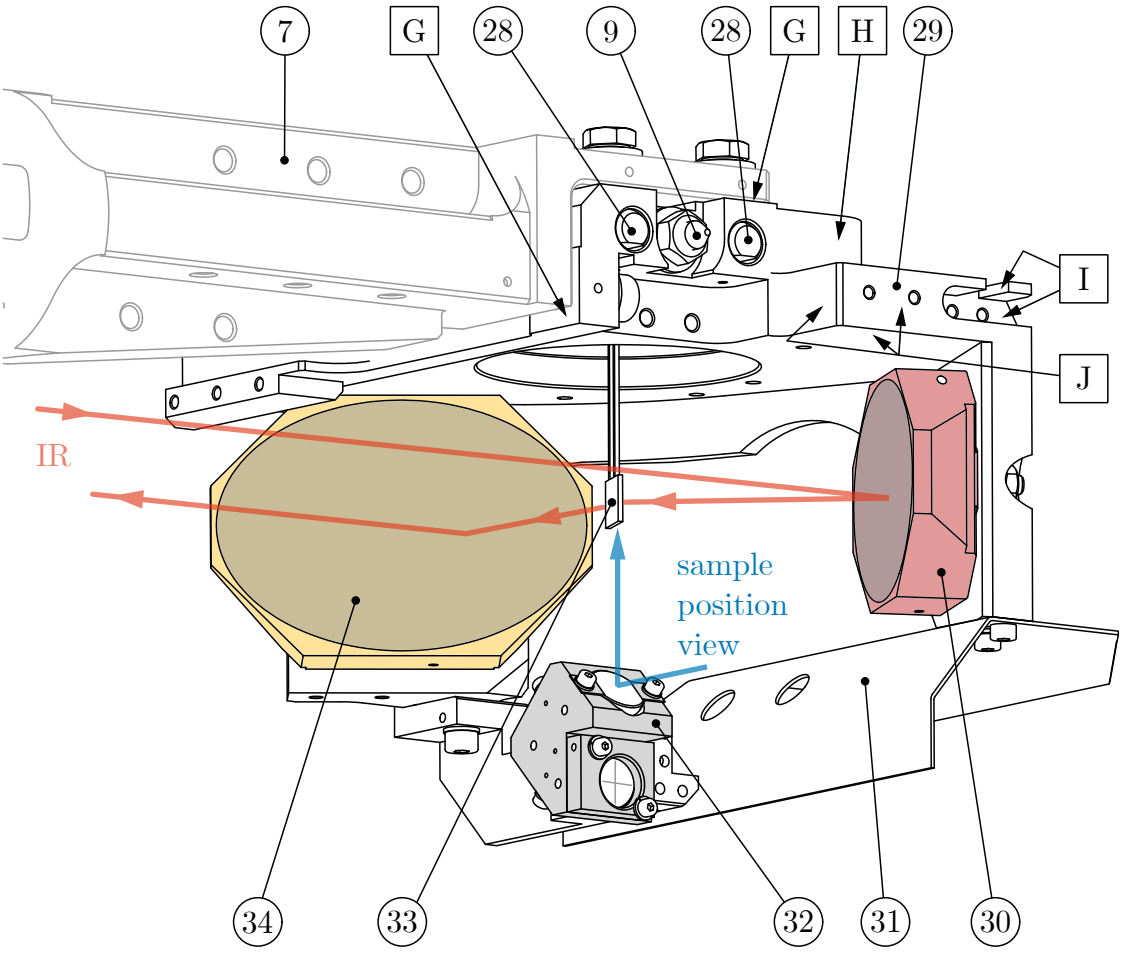

Figure 4.5: 3D visualisation of the sample focus platform. The circled numbers are the part numbers (see Table 4.4), and the boxed letters define the reference surfaces (see Table 4.5). Important optical components are highlighted in colour: the collector mirror in dark yellow (#34) and the illumination mirror in red (#30). The sample position finder is marked in grey (#32). The semi-transparent red line indicates the IR beam path and light direction through the system. The blue arrow represents the user view to the sample via the sample position finder.

part number	part name
7	UHV support beam
9	positioning pin
28	threaded inset
29	sample-focus platform
30	illumination mirror
31	metal evaporator shield
32	sample-position finder
33	sample plate
34	collector mirror

Table 4.4: Part list of the sample-focus platform assembly of the IRAS system shown in Figure 4.5.

reference surface	reference surface description
G	UHV support beam connection surfaces
H	angle selection plate calibration reference
I	angle selection mechanism mounting connection
J	calibration bracket mounting edge

Table 4.5: Reference surfaces of the sample-focus platform of the IRAS system shown in Figure 4.5.

Sample Positioning

The sample-position finder, shown in Figure 4.5 as part #32, enables the determination of the sample position and rotation angle. By looking at the sample position finder (indicated by the blue arrow in Figure 4.5), one can observe an image of the bottom of the sample and a measurement grid simultaneously, as shown in Figure 4.7(b). The design of the sample-position finder ia compact to avoid obstructing the free ports in the chamber.

Figure 4.6(a) shows the schematic optical path and function of the sample-position finder. The optical setup uses a 50/50 beam splitter (Thorlabs BSW04) made from fused silica to separate the beam into a sample and reticle path. The sample path measures 37.5 mm from the beam splitter centre to the sample bottom (blue dashed line) and is calibrated for the IRAS measurement position. For the design of the optical layout, a sample size of $6 \times 6\,\mathrm{mm}^2$ was assumed. A key design feature of the sample-position finder is that the reticle appears at the same distance as the sample bottom. This design enables a simultaneous view of the sample and the grid, allowing the measurement of the sample position based on the grid spacing without perspective errors, altering the visual size of the grid, even without a telecentric lens. It is important to note that the design accounts for the fact that the reticle image appears closer to the eye than given by the geometric length of the ray due to the beam splitter and the prisms (made from fused silica) in the reticle path [39].

Figure 4.6(b) schematically shows the 1 mm × 1 mm grid (grey) on the reticle and the sample on the sample plate, as it is visible for the user. The grid is aligned with the directions of the cryostat manipulator axis of the UHV chamber (x- and y-axis) and rotated by 20° with respect to the 0°-position of the cryostat manipulator. The origin of the manipulator coordinate system is not aligned with the centre of the grid. The centre of the grid marks the focal spot of the illumination mirror and, therefore, the ideal IRAS measurement position. Furthermore, an additional line defines the surface orientation for IRAS measurements. Here, the sample is rotated by 43.5° around the z-axis of the cryostat.

To calibrate the sample position for IRAS measurements, the sample was initially positioned in the grid centre, shown in Figure 4.7. Subsequently, the x- and y-coordinates of the sample were altered to maximise the ADC-count (infrared intensity at the detector) displayed by the OPUS software [40]. The fine-tuning of the position was then achieved through the use of a thick layer of ethylene ice formed on the sample surface by the molecular beam. By measuring p-polarised single-beam spectra and maximising the ADC-count and the peak height of the absorption band at $1440\,\mathrm{cm}^{-1}$ [76], the optimum IRAS measurement position shown in Figure 4.7 was found. This calibrated IRAS measurement position shows a x-offset of 0.25 mm and a y-offset of -0.65 mm to the centre of the grid.

It should be noted that the alignment of the optical system can change this position. An additional angle calibration of the grid was performed. Here, a custom mirror holder

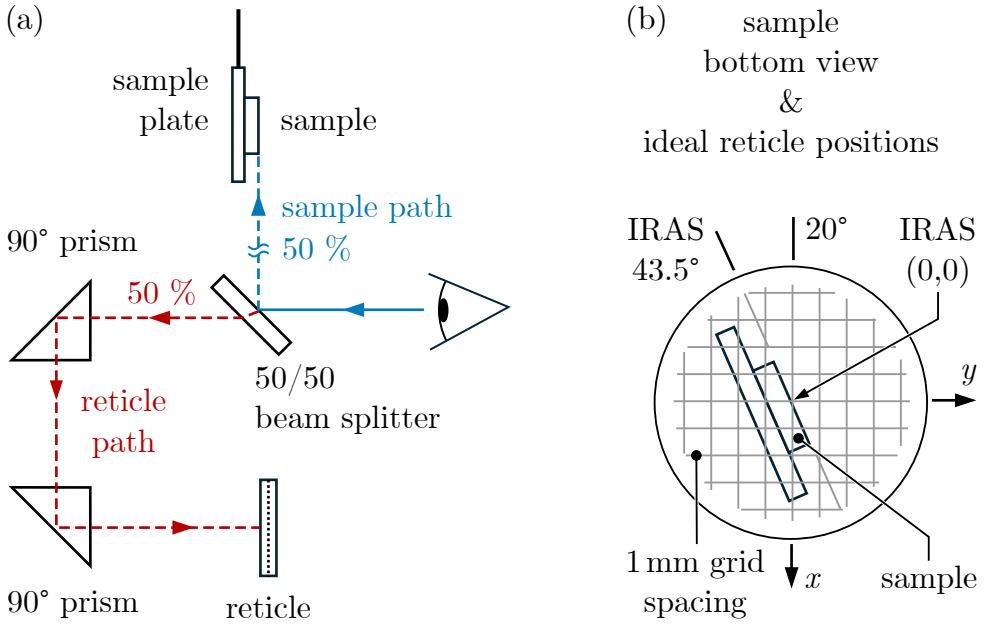

Figure 4.6: Schematic function of the sample position finder. (a) shows the side view of the sample position finder optics: a beam splitter, two prisms and a reticle (scale grid). A blue dashed line marks the view to the sample, and the red one marks the view to the reticle (adapted from [34]). (b) depicts a schematic image of the user view with the sample and reticle overlapping. The x- and y-axis are along the respective sample manipulator movement direction of the UHV chamber. The angle values indicate the manipulator rotation angles in the chamber coordinate system.

and a custom sample-focus adapter bracket (the same as for the intensity distribution measurement, see Section 5.1) were used. The calibration shows an angle offset of the ideal position of -1.4° from the reference surface □H seen in Figure 4.5. Assuming that the reference surface □H aligns with the y-axis of the chamber coordinate system, the vertical grid lines are at an angle of 18.6° instead of 20°. The expected calibration error is approximately ±0.15°, originating from the tolerances of the parts.

During measurements, a camera is used to determine the exact position of the sample. A virtual grid is overlapped with the reticle image and then shifted according to the calibration results as shown in Figure 4.7.

Angle-Selection Mechanism

The angle-selection mechanism enables the user to select any desired light incidence angle range to illuminate the sample. With the IRAS system, the range can be set between 48° and 87° (see Figure 3.13). As explained in Section 3.2.1, selecting the appropriate measurement parameters is crucial for achieving good SNR. Most of the angle-selection mechanism is within the UHV chamber, and the angle-selection plates can directly clip the beam (see Figure 4.2). Therefore, the primary design considerations were rigidity and precise movement to guarantee optimal functionality and stability.

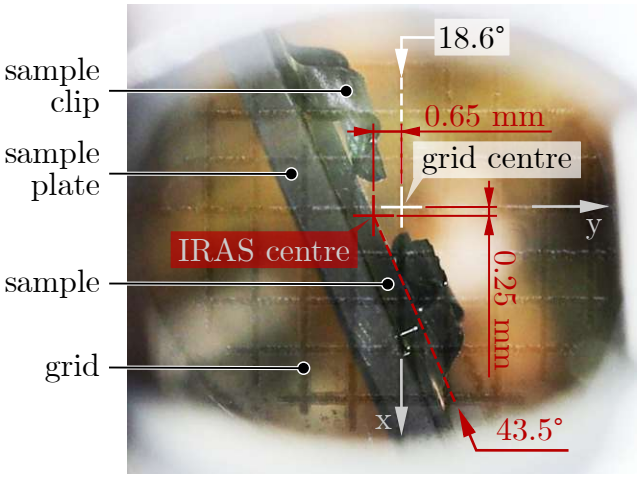

Figure 4.7: Photo of the sample and the scale grid through the sample-position finder. The grid centre and orientation are marked in white. The calibrated IRAS centre is marked in red. The calibrated IRAS measurement position (red) shows a slight offset to the grid centre (white). The grid is rotated by -1.4° with respect to the reference surface □H (see Figure 4.5), seen in Figure 4.5 and, therefore, the vertical lines have an angle orientation of 18.6° instead of 20° in respect of the chamber coordinate system.

Figure 4.9 shows a 3D representation of the angle-selection mechanism and its functionality. The component names are listed in Table 4.6. The angle selection mechanism can be split into two independent kinematic parts: red-marked components are linked to the change of the grazing incidence angle limit $\theta_{L,G}$, and blue-marked components alter the non-grazing angle limit $\theta_{L,N}$(see Figure 4.8). The full and framed arrows show the kinematic connection between the angle-selection plates and the angle-selection manipulator.

By rotating the rear part on, e.g., the grazing angle manipulator (red, #39) along the full arrow direction (clockwise, when viewed from outside of the chamber), the grazing angle link (#37) moves backwards and pulls the grazing angle lever (#35). The sliding linkage between the grazing angle link and grazing angle lever, in conjunction with the pivot mounting of the grazing angle lever on the grazing angle rotator (#36), moves the grazing angle plate (#46) into the IR beam and clips part of it. The kinematic design allows the two aperture plates to move independently and block specific incidence angles from reaching the sample.

Both angle-selection plates, the grazing angle plate (red, #46) and the non-grazing angle plate (blue, #47), are screwed to the levers and secured with lock washers. The plates and the levers are made from stainless steel of type 1.4404, which has low magnetic permeability so as not to disturb the XPS signal. Each lever is screwed to a rotator (see also Figure 4.10), which represents the pivot point for the levers and allows one to read the position of the angle-selection plates. Inside each rotator, two grooved ball bearings (SKF, 623) are stacked, enabling precise rotation. The double

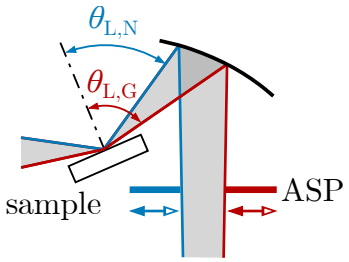

Figure 4.8: Schematic representation of the angle selection limits realised with the angle selection plates (ASP). The red line visualises the limiting angle for the grazing angles $\theta_{L,G}$. The limiting angle for the non-grazing incidence angles $\theta_{L,N}$ is shown in blue. The double arrows close to the selection plates indicate the movement direction (compare also to Figure 4.9).

ball bearing design reduces the clearance in the rotation mechanism. This is important because small movements in the pivot point translate to large movements at the angle-selection plates. Furthermore, the plates are less susceptible to vibrations (introducing noise). The distance between the angle-selection plates and the pivot point is around 100 mm. Three additional spring-loaded zirconia balls inside each rotator stabilise the rotation system by slightly pressing against the static plate position scale (#43). Both rotators (#36, #45) and the static plate position scale are stacked onto the bearings seat (#44), which connects the angle selection mechanism to the sample-focus platform (#29), precisely defined in position by the reference surfaces □I, shown in Figure 4.5. The components of the angle-selection mechanism described in this paragraph (#35, #36, #42, #43, #44, #45, #46, #47) are assembled independently from the linear motion shown on the right side in Figrue 4.9.

The actuation of the angle-selection plates is achieved by two linear bellows drives from UHV design (LBD16-25-H) with a stroke of 25 mm (red,#39 and blue,#40). These are mounted to a custom DN 40 CF flange with angled DN 16 CF half nipples welded to the flange. The two motion links (#37, #41) connect the rotational motion of the angle-selection plates to the linear motion of the linear manipulators. The claw design of the motion link hooks the lever and enables a sliding motion between the lever and the motion link. A clearance of up to 2 mm between the lever and the motion link allows the decoupling of the rotational motion from the linear motion, reducing the vibrations on the angle-selection plates. For IRAS measurements, the levers are decoupled. Then, the spring-loaded zirconia balls in the rotators hold the aperture plates in place. The linear motion part described in this paragraph consisting of the components #37 to #41 can be assembled separately from the rotational part. To mount it to the chamber, both linear bellows drives have to be in the fully extended position.

To set the angle selection plates to a range limiting angle $\theta_{L,G}$ or $\theta_{L,N}$ (see Figure 4.8), respectively, the rotators and the static plate position scale feature engraved lines, schematically shown in Figure 4.10. Figure 4.10 (a) depicts a detailed view of the rotation mechanism for the angle-selection plates. As described above, the plates are

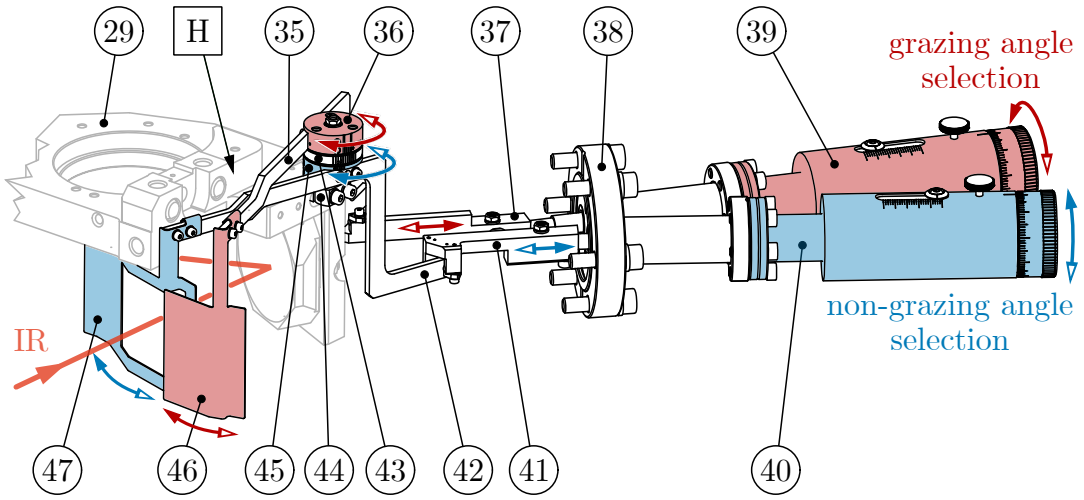

Figure 4.9: 3D view of the angle-selection mechanism. The mechanism to select the grazing angle limit $\theta_{L,G}$ is coloured in red. The mechanism to select the non-grazing angle limit $\theta_{L,N}$ is marked in blue. The arrows illustrate the connected kinematics of the angle-selection manipulator and the respective angle-selection plate. The rotation mechanism between the apertures and the manipulators features a scale to read the aperture position (see Figure 4.10).

directly connected to the rotators (#36 in red and #45 in blue). Figure 4.10(b) shows how to read the position of the aperture plates. On the static position scale, between the two rotators in red and blue, eleven lines are engraved, defining the possible positions ap_N for the non-grazing angle plate and ap_G for the grazing angle plate. The first line on the right marks position one. In total, eleven positions are visible. A continuous setting of the plate position is possible.

The grazing angle rotator on top, highlighted in red, features five engraved lines. The indicator line is the right edge of the most left engraved line, marked in dark red at the right to the circular mark. It is used to read the position of the grazing angle plate, altering the grazing angle limit $\theta_{L,G}$. The position of the indicator line in respect of the engraved lines on the static plate position scale defines the position ap_G, e.g., if the indicator line (dark red) is aligned with the 4^{th} line of the static scale, then $ap_G = 4$. Using the edge of the engraving enhances the accuracy of the position reading. The same concept applies to the non-grazing rotator (highlighted in blue). The non-grazing angle plate connected to this rotator alters the non-grazing angle limit $\theta_{L,N}$. Five engraved lines are visible. The position indicator line is the right edge of the centrally engraved line (dark blue). Overlapping this line with the static scale on top gives the non-grazing aperture plate position ap_N. Figure 4.10(b) shows an example for $ap_N = 5.5$. Here, the blue marked position indicator is located halfway between positions 5 and 6. By utilising a camera and a virtual scale, the position can be read with a precision of ±0.1 translating into an incidence angle error of about ±1° (see Table A.3).

part number	part name
29	sample-focus platform
35	grazing angle lever
36	grazing angle rotator
37	grazing angel motion link
38	angle-selection flange
39	grazing angle-selection manipulator
40	non-grazing angle-selection manipulator
41	non-grazing angle motion link
42	non-grazing angle lever
43	plate position scale
44	bearing seat
45	non-grazing angle rotator
46	grazing angle plate
47	non-grazing angle plate

Table 4.6: Part list of the angle-selection mechanism. The assembly drawing with the referenced part numbers can be seen in Figure 4.9.

The angle-selection mechanism was calibrated to link the aperture plate positions ap_{G} and ap_{N} to the incidence angle θ on the sample. This was done by utilising the 3D model of the IRAS system and replicating the real system. The calibration reference is given by the two levers aligned parallel to the reference surface □H. As a result, the positions of non-grazing angle plate ap_{N} changing $\theta_{\mathrm{L,N}}$ and the position of the grazing angle plate ap_{G} altering $\theta_{\mathrm{L,G}}$ can be calculated according to

$$ap_{\mathrm{N}}(\theta_{\mathrm{L,N}}) = 11.767 - 0.108 \cdot \theta_{\mathrm{L,N}}, \text{ and} \tag{4.1}$$

$$ap_{\mathrm{G}}(\theta_{\mathrm{L,G}}) = 11.448 - 0.09927 \cdot \theta_{\mathrm{L,G}}. \tag{4.2}$$

The inverse functions allow to calculate the range limiting angles $\theta_{\mathrm{L,N}}$ or $\theta_{\mathrm{L,G}}$ with the known aperture plate positions ap_{N} or ap_{N}.

$$\theta_{\mathrm{L,N}}(ap_{\mathrm{N}}) = 108.898 - 9.254 \cdot ap_{\mathrm{N}}, \text{ and} \tag{4.3}$$

$$\theta_{\mathrm{L,G}}(ap_{\mathrm{G}}) = 115.31 - 10.07 \cdot ap_{\mathrm{G}}. \tag{4.4}$$

Table A.3 in the appendix shows the relationship between the aperture plate positions ap_{i} and the limiting angle $\theta_{\mathrm{L,i}}$ for the complete angle of the IRAS system. I stands for G or N. The expected calibration error is approximately ±1°.

The absolute limiting angle setting error is influenced by the minimum angle spread discussed in chapter 3.3.2, scale grid calibration inaccuracies, imprecise limiting angle position setting, and angle-selection mechanism calibration errors, together achieving an absolute precision of approximately ±2.5°. The reproducibility is within ±1°.

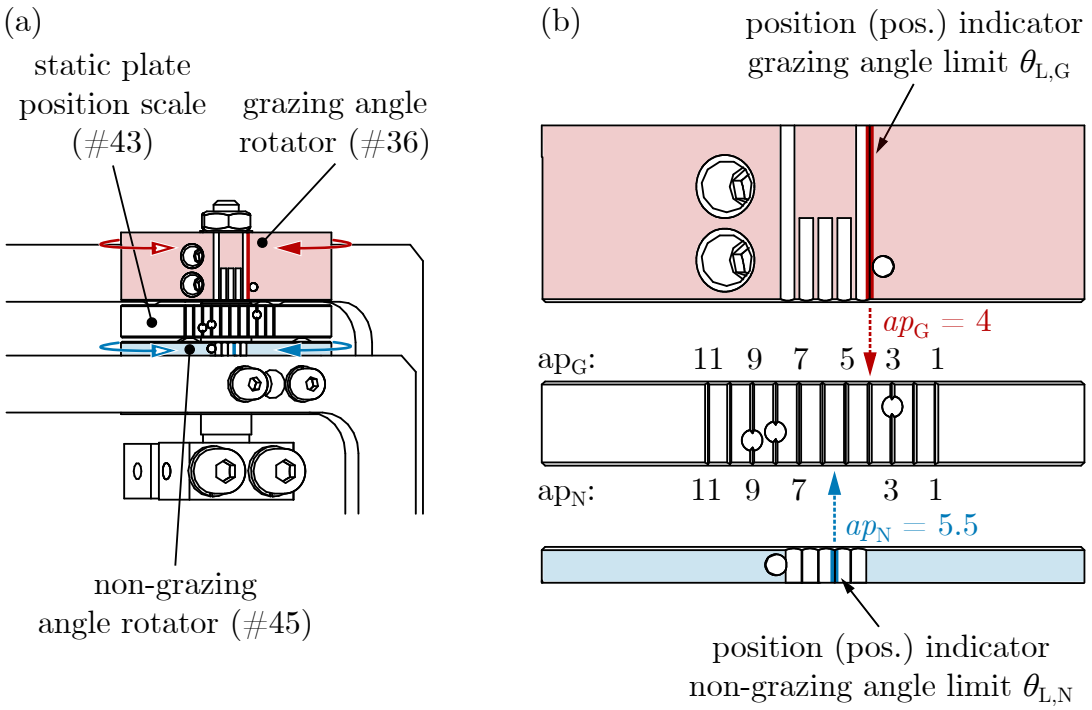

Figure 4.10: Detail view of the angle-selection mechanism. (a) shows the rotation mechanism with the non-grazing angle rotator (red) and the grazing angle rotator (blue). The coloured double arrows indicate the rotatable parts. (b) illustrates the schematic principle for reading the aperture position: the grazing angle selection position ap_G and non-grazing angle selection position ap_N. The thick coloured vertical lines show the position indicator. The dashed, coloured arrows and the positions to the right are examples. The visible engraving on the scale mimics the scale in the real system.

4.2.4 Summary

The IRAS setup is designed as a compact measurement system. Its assembly incorporates four distinct sub-assemblies: the core part assembly, detection platform, sample-focus platform, and angle selection mechanism, each of which can be assembled independently. The central flange design concept serves as the foundation for precisely connected components and a stable IRAS measurement platform. The additional implementation of the angle-selection mechanism allows the choice of optimised incidence angle ranges for IRAS measurements.

CHAPTER 5

PERFORMANCE EVALUATION

The performance evaluation of the IRAS system was done in two steps. First, the optical system was characterised by measuring the intensity distributions in the critical focal points, the sample and the detector focus point (see Figure 3.1). The measurement results were then compared to the simulation. This ensured that the optics was working properly and that the IRAS system was checked before mounting it to the UHV chamber. In the second step, the performance of the IRAS system in UHV was compared to IRAS results published in the literature [16, 18, 23, 27, 77, 78]. The comparison focuses on the SNR performance of the system. Here, the completely assembled IRAS setup mounted to the surface chemistry chamber was used. The FTIR spectrometer Bruker VERTEX 80v equipped with the standard mid-IR source, also known as glowbar, was used for all the performance checks. Parts of this chapter can be found in [34].

5.1 Optical Path Evaluation

The complete performance check of the intensity distribution at the sample and detector focus was carried out with the IRAS system mounted via the central flange to a home-built optical table. The central flange features two mounting surfaces on the sides and one on the bottom. The IRAS setup was partly assembled for these measurements to ensure easy access to the optical components. Before the measurements, the optical system was aligned. The ideal component positions, given by the simulation, served

as a starting point for the alignment process. In addition to the sample and detector focus, intensity checks in the polariser focus were utilised for alignment.

For the intensity characterisation, the BaF_2 windows in the illumination and collection path on the central flange and the motorised polariser (see Figure 3.1 and 4.2) were not mounted. Furthermore, the high-vacuum box did not enclose the optics between the spectrometer and the central flange. The angle-selection plates were completely open to not obstruct the IR beam. During all the measurements, the optics was exposed to atmospheric conditions, and the laboratory was completely dark to avoid daylight disturbing the measurements.

A CMOS camera DMM 37UX178-ML from The Imaging Source was used to measure the intensity distributions in the different focal points. Its sensor (Sony IMX 178, back-illuminated) is sensitive to wavelengths in the NIR region, but the pixels have a limited acceptance angle. Therefore, the camera cannot detect light incidence at grazing angles. A thin, framed glass plate protects the sensor. Note that the glass plate must be considered when positioning the camera because it shifts the image closer to the object. For the measurements, the camera was mounted on holders designed for placing the camera sensor in the respective focal point position, as evaluated from the simulation. The camera holders were designed with the protective glass plate taken into account. The camera holder for the detector focus provided some adjustment possibilities.

Measurements in the detector focal point were obtained by replacing the sample with a flat aluminium mirror (⌀ 12.5 mm). This mirror was positioned in the IRAS position by a custom mirror holder and a custom sample-focus adapter bracket holding the mirror holder and the mirror in place. The bracket was screwed to the sample-focus platform utilising a milled corner joint (see reference surface □J in Figure 4.5). The same bracket was also used to hold the camera mounted on a holder in the ideal sample focus position.

During the measurements of the intensity maps, the J-stop of the spectrometer was 6 mm. The helium neon (HeNe) laser for position detection of the moving mirror inside the FTIR spectrometer (see Figure 2.2) was turned off to avoid saturating the camera sensor. This also necessitated stopping the moving interferometer mirror at an unknown position because the alignment of this mirror relies on the HeNe laser. Under standard operation of the spectrometer, the laser and the moving mirror are running.

Figure 5.1 illustrates the simulated and measured intensity distributions in the sample and detector focal points. The colour scale ranges from dark blue, indicating zero relative intensity, to dark red, representing a high relative intensity of one [see Figure 5.1(b)]. Horizontal and vertical line profiles through intensity-weighted centroid ("centre of mass") are plotted on the sides of the intensity maps. Due to the stationary interferometer mirror in the spectrometer during the measurement and the idealised simulation, the intensity maps are qualitative. The values for the FWHM and $w_{i,5\,\%}$

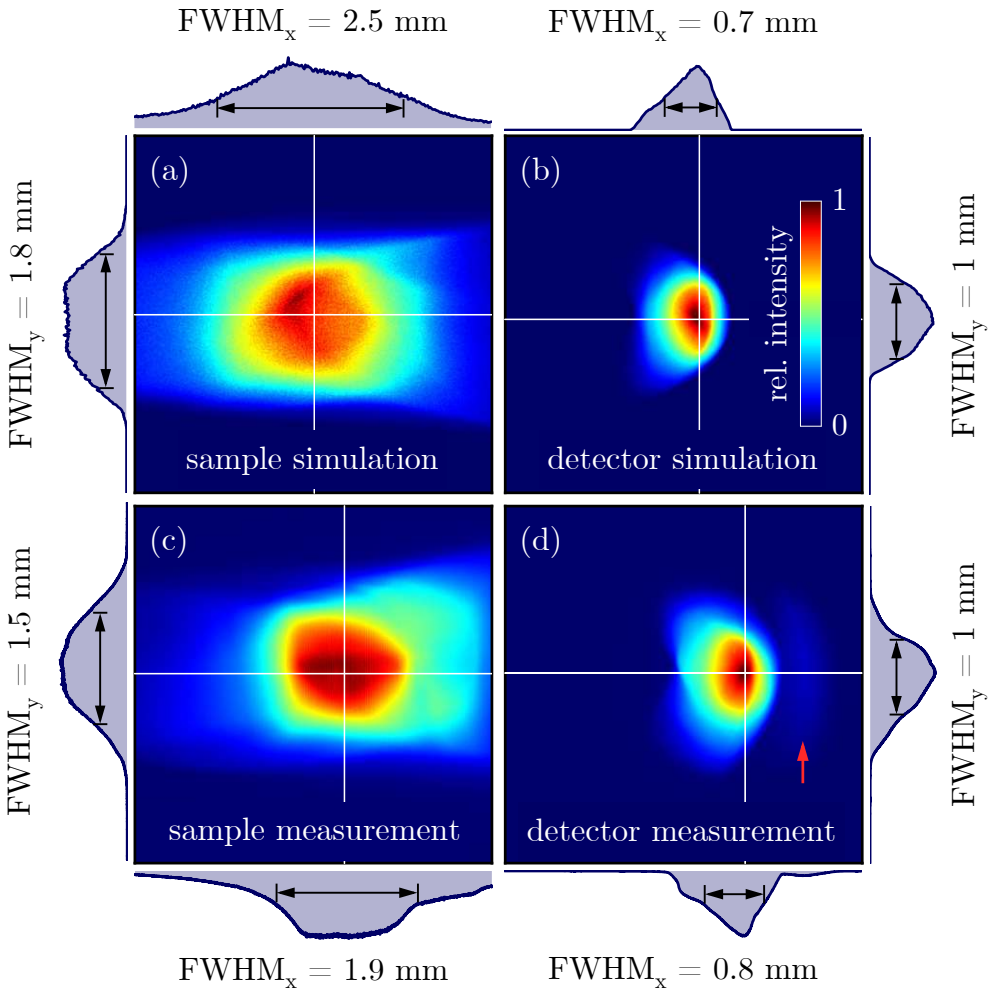

Figure 5.1: Simulated and measured intensity maps in the sample and detector focus. A J-stop setting of 6 mm was used. The dark blue areas represent zero relative intensity, and the dark red areas show maximum relative intensity. Besides the intensity maps, line profiles crossing the intensity-weighted centroid ("centre of mass") are shown. Their position is indicated with white lines. The black double arrow in the line profiles marks the FWHM in each profile. (a) Simulated intensity on the sample and (b) on the detector. (c) and (d) visualise the measurement results for the sample and the detector, respectively. All images are $4.8 \times 4.8\,\mathrm{mm}^2$ in size. See also Figures 4.9 and 4.10. This figure is adapted from [34].

are tabulated in Table 5.1. The width $w_{i,5\,\%}$ is introduced as a measure of the spot size in the x- or y-direction. It defines the width of the line profile at 5 % of the maximum relative intensity ($I_{\mathrm{rel,\,max}} = 1$). Therefore, it will be called spot width in the following.

A comparison of the sample intensity maps in Figure 5.1(a) and (c) reveals a good agreement of the distributions, particularly in the central region indicated by the colour transition from yellow to red. The FWHM in the x- and y-direction is smaller in the experiment than in the simulation, which indicates slightly better focusing. However, the measurement shows a less symmetric intensity distribution around the central area along the x-direction than the simulation. This can be attributed to the grazing incidence of the light, which cannot be detected with the camera due to the limited light acceptance angle. The grazing illumination creates a large elongated illumination area along the x-axis, exceeding the sample size. The outer dimensions of the intensity maps (a) and (c) replicate a sample size of $4.8 \times 4.8\,\mathrm{mm}^2$. Due to the illumination-shaping slit, the majority of the intensity is concentrated within the 3.5 mm circular MB spot. The spot sizes in the y-direction ($w_{y,5\,\%}$) shown in the simulation (2.6 mm) and the measurement (2.9 mm) fit very well inside the MB spot. This helps to reduce the sensitivity for sample shifts along the cryostat axis (z-axis). The results are summarised in Table 5.1.

In the detector focus [see Figure 5.1(b) and (d)], the simulation and the measurement show excellent agreement in the high-intensity region (yellow to red), also confirmed by the excellent match of the FWHMs in x- and y-direction. A spot broadening in the experiment at lower relative intensities (< 0.5) in both directions can be seen compared to the simulation. Also, the spot size evaluated from the experimental data exceeds the value of the simulation (see Table 5.1). This is caused by a slight out-of-focus position of the camera during the measurement. The spot width $w_{y,5\,\%}$ in the simulation (see Figure 5.1) is 1.5 mm. Due to the asymmetric shape of the illumination, the maximum extension in y-direction is shifted to the left of the intensity weighted centroid and is 1.9 mm at 5% of the maximum intensity. This is bigger than the 1.4 mm diagonal of the $1 \times 1\,\mathrm{mm}^2$ IR detector element. However, the majority of the intensity is focussed on the IR detector element. The asymmetric shape of the illumination occurs because the detector element is placed 0.5 mm behind (along the light direction) the focal point of the detector mirror. This offset from the ideal focus point allows more light to pass through the cold stop of the detector, which is placed in front of the detector element. The spot size in the x-direction is smaller than in y-direction, due to the illumination-shaping slit and grazing illumination of the sample. The additional feature seen in the measured detector intensity distribution, as marked in with a red arrow in Figure 5.1(d), can be attributed to light reflected from the sample replacement mirror support.

The overall good agreement between simulation and measurement confirms the correctness of the simulation and the design of the IRAS setup. A more detailed charac-

terisation of the beam path with intensity maps in the different focal points and various J-stop settings can be found in the report prepared by Vojtěch Mikerásek [79].

Additional power measurements were conducted using the controller PM100D and the power sensor S401C from Thorlabs. The sensitivity of the sensor covers the wavelength range from 190 nm to 20 µm. Only one BaF_2 window on the central flange was installed, and no polariser was present in the beam path. The measurements were carried out with an aluminium mirror, replacing the sample and the HeNe laser in the spectrometer turned off (moving interferometer mirror stopped). Note that the IRAS system was exposed to atmosphere. The power meter measurements in the detector focus resulted in 5.6 mW of IR light reaching the detector position with a J-stop of 6 mm. When the J-stop was reduced to 3 mm, the measured power decreased to 2.9 mW. Considering the additional losses due to the absence of some components (polariser, second window on the central flange, detector window) and the presence of metal oxide samples in the final application, the power at the detector position is estimated to be in the order of hundredths of µW, depending on the polarisation, the J-stop, the angle-selection plate setting and the material. Note that at a J-stop of 6 mm, the power meter sensor is larger than the illumination spot, capturing all the light. The MCT detector element only detects portions of the spot at this J-stop setting, decreasing the detected power. This effect decreases when the J-stop is set to 3 mm.

In comparison, a power of 23 mW was measured at the standard detector position inside the FTIR spectrometer with a J-stop of 6 mm. When the J-stop was set to 3 mm, the power measurement resulted in 7.1 mW. In this case, the IR beam passed through the standard compartment of the spectrometer without encountering any obstructions.

	$FWHM_x$ (mm)	$FWHM_y$ (mm)	$w_{x,5\,\%}$ (mm)	$w_{y,5\,\%}$ (mm)	Figure
sample simulation	2.5	1.8	-	2.6	5.1(a)
sample measurement	1.9	1.5	-	2.9	5.1(c)
detector simulation	0.7	1	1.3	1.5	5.1(b)
detector measurement	0.8	1	1.5	2	5.1(d)

Table 5.1: Summary of the FWHMs and the spot widths $w_{i,5\,\%}$ in the sample and detector focal points. The spot width $w_{i,5\,\%}$ defines the width of the line profile at 5 % of the maximum relative intensity ($I_{rel,\,max}$ = 1). Due to the grazing incidence of the light on the sample, the relative intensity in the x-line profile does not drop below 0.05, and no values for $w_{x,5\,\%}$ can be evaluated. The measurements and simulations were performed at a J-stop setting of 6 mm.

5.2 Spectroscopic Performance for CO and D_2O on $TiO_2(110)$

The spectroscopic performance characterisation described in this section first focuses on the optimisation of the incidence angle range by optimising the SNR in IRAS measurements of CO on the $TiO_2(110)$ surface. In this model system, the dipole moment is normal to the surface [18, 27, 77, 78] and sensitive to p polarisation. Consequently, the Brewster angle is a relevant quantity for the optimisation process. IRAS spectra acquired with different incidence angle ranges and CO coverages are presented. To characterise the s-polarised IRAS performance for adsorbates with dipole moments parallel to the surface and perpendicular to the plane of incidence, D_2O was adsorbed on the reduced $TiO_2(110)$ surface. In this model system, the dipole moments are oriented predominately parallel to the surface [16, 23].

For all the measurements testing the IRAS performance, a synthetic rutile $TiO_2(110)$ bulk single crystal from CrysTec GmbH with a miscut angle smaller than 0.05° was used. The [001] direction of the $TiO_2(110)$ crystal was oriented along the incidence plane of the IR beam. Given the broad illumination cone angle, minor misalignments of the [001] direction relative to the incidence plane can be considered negligible. Four Ta clips pressed the sample on its corners onto a Ta sample plate. A 0.025 mm thick gold foil ensures thermal contact between the sample and the sample plate. Figure 3.13(a) shows a similar mounted crystal. A thermocouple was spot welded to the sample plate to read the temperature. The sample plate was screwed to the helium flow cryostat of the UHV chamber [62]. During the measurements, a base temperature of 37 K was reached.

Before performing IRAS measurements, the sample was prepared using the following standard preparation procedure. First, the sample was annealed to 950 K followed by cycles of sputtering (1 keV Ne^+, 15 min, at 300 K) and UHV annealing (20 min, at 900 K). From time to time, the sample was reoxidised by one cycle of O_2 annealing (15 min, at 900 K, with $p_{O_2} = 5 \times 10^{-7}$ mbar) and UHV annealing (10 min, at 900 K) [66, 78, 80]. After the standard preparation of the sample, CO or D_2O was dosed with the molecular beam to perform the test measurements. It should be noted that the reduction state of the sample may be different in all measurements presented here due to the repeated preparation steps involved in the lengthy test measurements. An estimation from D_2O TPD suggests a reduction state of about 5% [81–84].

If not mentioned otherwise, the IRAS spectra were recorded with a mirror speed of 60 kHz, corresponding to a mirror velocity of 19 mm/s (see equation 2.5). Furthermore, a resolution of 4 cm^{-1}, a zero filling factor of one and a Happ-Genzel apodisation were set for the measurements. In p-polarised measurements, a J-stop setting of 6 mm was used, and 1000 scans were averaged for one single beam spectrum. This resulted in a total IRAS measurement time of about 5 min for one $\Delta R/R_0$ spectrum for which two single beam spectra, the reference spectrum and the sample spectrum, are required. IRAS measurements with various angle ranges were performed. To avoid detector

saturation in s-polarised measurements, a J-stop diameter of 3 mm was used.[1] Due to the lower signals occurring for s polarisation, 4000 scans were averaged for one single beam spectrum, leading to measurement times of about 20 minutes for one $\Delta R/R_0$ spectrum. Here, the full angle range of the system from 48° to 87° was utilised.

As mentioned in Section 2.3, the standard IRAS measurement procedure is to first acquire a reference spectrum (R_0) from the clean sample, dose the adsorbates, and subsequently measure a sample spectrum (R). R_0 and R together give the normalized reflectivity difference $\Delta R/R_0$ according to equation 2.9. The spectra recorded with this procedure will be referred to as adsorption spectra. The dosing with the molecular beam must be performed in a position different from the IRAS position. Repositioning the sample between the reference spectrum and the sample spectrum requires returning to the same position for the sample spectrum measurements. Clearances in the sample manipulator introduce position reproduction errors and, with this, shifts and distortions of the baseline, which can also reduce the signal intensities. This mispositioning can be compensated by utilising the sample-position finder (see Section 4.2.3). Additional fine-tuning of the sample position before acquiring the complete sample spectrum can be done with correcting the baseline of the $\Delta R/R_0$ spectrum of quick repetitive sample spectra (about 100 scans) by slight sample movements. An IRAS measurement can also be performed in reverse order. First, the sample spectrum is acquired, and then the desorption of the adsorbed molecules from the sample is performed. Subsequently, the reference spectrum is measured. Spectra recorded in this manner are referred to as desorption spectra.[2] One advantage of this approach is that it eliminates the need for sample movements between the reference and sample spectrum, simplifying and speeding up the workflow. Therefore, most measurements presented in this chapter are desorption spectra. However, a drawback of this method is that the clean state of the sample after desorbing the adsorbates cannot be verified. Therefore, adsorption spectra were performed from time to time to check the cleanliness of the sample after desorption.

To evaluate the performance of the IRAS system, the signal intensities (directly measured in the spectrum) and the root mean square (RMS) noise between 1900 cm^{-1} and 2100 cm^{-1} were analysed for different spectra. For the noise evaluation, the OPUS software [40] and a parabolic fit were used.

5.3 CO on TiO_2(110)

To evaluate the performance of the IRAS system measuring p-polarised spectra, low coverages of CO adsorbed on reduced rutile TiO_2(110) were chosen. It qualifies as

[1] The throughput was limited to about 80 % of the MCT detector saturation limit (ADC-count$_{\mathrm{saturation}}$=32768).

[2] The spectrometer software OPUS [40] does not support the desorption procedure, leading to inaccurate signal intensities in the spectrum. However, as demonstrated in this thesis, the resulting error is minor and can be neglected for $\Delta R/R_0 \ll 1$. The desorption spectra presented in this thesis were manually processed using equation 2.9 with the acquired single-beam spectra and exhibit no error.

a good benchmark model system for the investigation of vibrational modes with the dipole moment normal to the surface because previous studies [18, 23, 27, 77, 78] provide comprehensive IRAS measurements.

5.3.1 Incidence Angle Range Optimisation

To obtain optimal SNR in p-polarised measurements, a restriction of the incidence angle range is necessary. This is due to the band inversion at the Brewster angle. Therefore, in the first step, the incidence angle range was optimised for the measurements of CO adsorbed on TiO_2 with p-polarised IR light, finding the best SNR. The angle-selection plates of the IRAS system can alter the incidence angle range, adapting the range for different polarisations and materials. By adjusting the angle-selection plates, any incidence angle range between 48° and 87° can be set, as shown in the Figures 3.1, 3.3 and in Section 4.2.3. The optimisation process was performed in the non-grazing and the grazing angle range. As mentioned in Section 4.2.3 the angle-selection plates can be set with a precision of ±2.5° and a reproducibility of ±1°, described in Section 4.2.3. The optimised measurement parameters are then used to demonstrate the performance of the system by comparing different incidence angle ranges. IRAS spectra of 1 ML CO on the reduced $TiO_2(110)$ surface were acquired, for optimising the incidence angle range. 1 ML CO corresponds to a dose of 1.36 L (Langmuir; $1\,\mathrm{L} = 10^{-6}\,\mathrm{Torr\,s}$). CO was dosed at 43.5 K and a desorption spectrum was acquired (see section 5.2). To desorb the CO, the sample was heated to 300 K. Only one angle-selection plate was adjusted between each measurement.

Figure 5.2 compares spectra acquired in the non-grazing, the grazing and the full incidence angle range. Here, 1 ML CO was adsorbed on the $TiO_2(110)$ surface. The upper panel of Figure 5.2(a) visualises the measurement angle ranges in the incidence angle dependent $\Delta R/R_0$ calculation for p-polarisation, considering the system specific corrections. More details of this plot can be found in Section 3.3.5. The optimum SNR of 69.4 can be seen for the non-grazing range, in Figure 5.2(b). Compared to the signal intensity observed in the grazing range, the blue curve in Figure 5.2(c), the peak height in the non-grazing range is higher by a factor of 1.8. This originates from the higher average signal intensity resulting from the non-grazing incidence angles [see Figure 5.2(a)]. Furthermore, the non-grazing range has the advantage that all the light gets reflected from the adsorbate-covered area. Therefore, the vicinity illumination does not reduce the signal intensity (see Figures 3.13 and 3.14). The higher signal intensity and the vanishing vicinity illumination are the main reasons the measurement performance is better in the non-grazing range. The noise is slightly higher in the non-grazing range than in the grazing range. The exact values are given in Table 5.2. Figure 5.2(d) shows the spectrum acquired with the full incidence angle range from 48° to 87°. Here, the noise is lower by a factor of 2.1 compared with the grazing range. The reason is the increased intensity throughput. However, a significantly lower peak height and lower SNR of 24.4 are observed, resulting from the simultaneous measurement of positive and negative peaks that partly cancel out [compared with Figure 5.2(a)]. Although the performance for p-polarised measurements in the full range is weaker than

in the non-grazing and grazing range, the peak orientation of the full incidence angle range provides information on which side a larger peak, and, hence, a better SNRs can be expected.

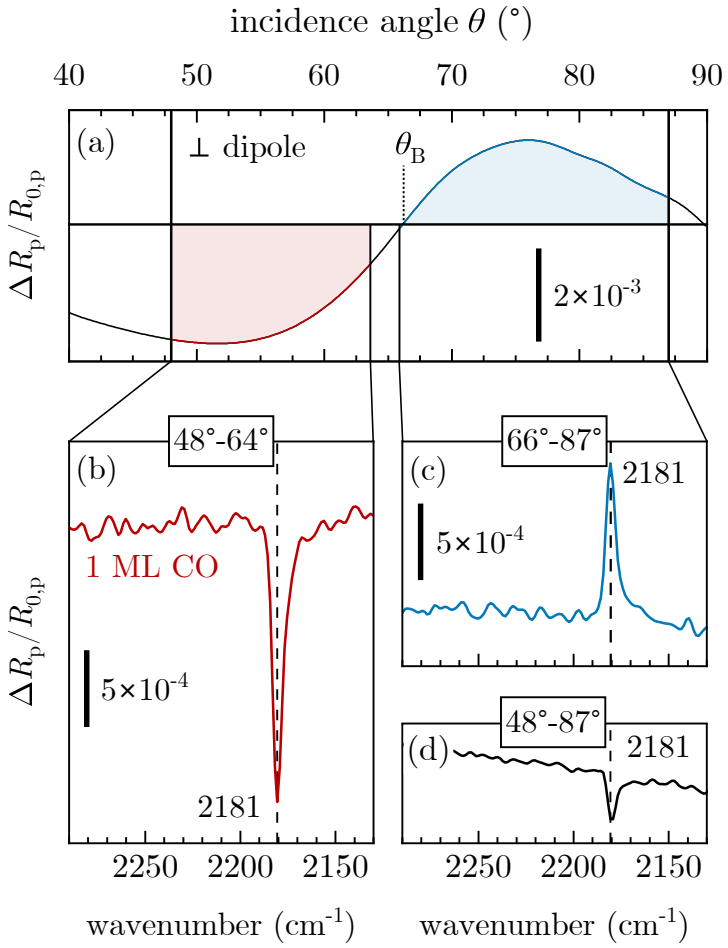

Figure 5.2: Calculated normalised reflectivity difference and IRAS raw spectra measured with different angular ranges in p-polarisation. (a) shows the normalised reflectivity difference $\Delta R_\mathrm{p}/R_{0,\mathrm{p}}$ with corrections for our IRAS system, for an adsorbate on the TiO_2(110) surface at $\tilde{\nu}$ = 2178 cm^{-1}. (b) to (d) depict spectra of 1 ML CO measured with a resolution of 4 cm^{-1} and 1000 scans. IRAS spectra acquired with the non-grazing range (b), grazing range (c) and full range (b) are shown. For comparability, the measured spectra are plotted with equal $\Delta R/R_0$scales. (b), (c) and (d) are adapted from [34].

On TiO_2, the Brewster angle splits the measurement range into approximately two halves. For materials with a lower refractive index than TiO_2 (n_{TiO_2} = 2.27), the Brewster angle is located lower (56° for n = 1.5). This decreases the usable non-grazing angle range, leading to a lower throughput. In this case, better SNRs are expected for the grazing incidence angle range. Another example is Fe_3O_4, a material with the pseudo-Brewster angle of 74.1°. Here, better performance is expected in the non-grazing range [see Figures 2.6(b) and 2.9].

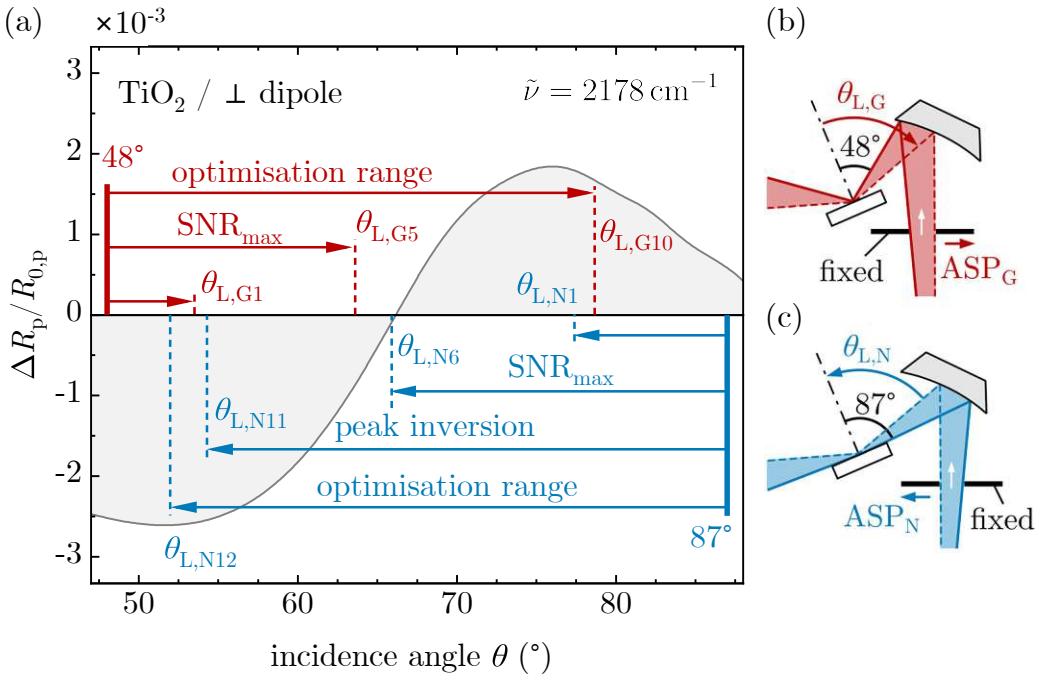

Figure 5.3: Concept of the SNR optimisation process. (a) shows the schematic measurement angle range representation of the optimisation process. The solid grey curve shows the calculated normalised reflectivity difference $\Delta R_p/R_{0,p}$ with the system-specific corrections (see Section 3.3.5) for TiO_2 and a dipole moment normal to the surface, as a function of the incidence angle θ. The non-grazing range optimisation is illustrated in red. The solid vertical line highlights the minimum incidence angle of θ_{min} = 48°, and the dashed line highlights the grazing limit angle $\theta_{\text{L,G}}$. The red arrows mark the first measurement angle range from θ_{min} to $\theta_{\text{L,G1}}$, the incidence angle range with maximum SNR and the complete non-grazing optimisation range. The grazing range optimisation is shown in blue. The arrows indicate the complete grazing optimisation range and the incidence angle range with maximum SNR. The blue, solid vertical line marks the maximum incidence angle of θ_{max} = 87°. The dashed lines indicate the non-grazing limit angle $\theta_{\text{L,N}}$. (b) shows the schematic optical path with a fixed non-grazing and moving grazing angle plate (ASP_G). (c) visualises the optical path for the grazing optimisation where the non-grazing plate ASP_N moves (see also Figure 4.9).

For the optimisation, various IRAS spectra with different non-grazing and grazing incidence angle ranges were measured to optimise the SNR. The schematic process of optimisation is depicted in Figure 5.3. In Figure 5.3(a), the grey curve describes the normalised reflectivity difference $\Delta R/R_0$ for p polarisation and a perpendicular dipole moment with the IRAS setup specific corrections, as shown in Section 3.3.5. A certain angle range was set for every measurement in the optimisation process. A measurement utilising an angle range integrates the reflectivities R and R_0 over all the angles in this angle range.

The red annotations, schematically shown in Figure 5.3(a), describe the optimisation process for the non-grazing angle range. Here, for every measurement $\theta_{\mathrm{min}} = 48°$ remained unchanged. This angle is visualised as a solid red vertical line. The limiting angle $\theta_{\mathrm{L,G}}$ was then increased step by step to more grazing incidence angles for every measurement from $\theta_{\mathrm{L,G1}}$ to $\theta_{\mathrm{L,G10}}$, partly indicated by the red dashed lines. The different incidence angle ranges for the measurements are shown as red arrows. The change of $\theta_{\mathrm{L,G}}$ is realised by moving the angle-selection plate $\mathrm{ASP_G}$, shown in Figure 5.3(b). The schematic optimisation in the grazing-incidence angle range, is visualised in blue in Figure 5.3(a). Here, $\theta_{\mathrm{max}} = 87°$ (blue solid line) was fixed, and the limiting angle for the non-grazing angles $\theta_{\mathrm{L,N}}$ was varied (blue dashed line). In every measurement, $\theta_{\mathrm{L,N}}$ was shifted step by step to lower incidence angles starting from $\theta_{\mathrm{L,N1}}$ and ending at $\theta_{\mathrm{L,N12}}$. The blue arrows indicate the incidence angle ranges. To realise the different limiting angles $\theta_{\mathrm{L,N}}$ the angle-selection plate $\mathrm{ASP_N}$ was moved out of the beam, as shown in Figure 5.3(c).

Figure 5.4 illustrates the outcome of the optimisation procedure, in which the signal-to-noise ratio (SNR) was evaluated from IRAS spectra of 1 ML CO on reduced $TiO_2(110)$, measured with varying incidence angle ranges within the grazing and non-grazing range. Figure 5.4(a) depicts the SNR of IRAS measurements acquired in the non-grazing range. Each data point represents a single measurement with an incidence angle range from $\theta_{\mathrm{min}} = 48°$ to a different limiting angle $\theta_{\mathrm{L,G}}$. The limiting angle is set by the grazing angle plate ($\mathrm{ASP_G}$). As $\theta_{\mathrm{L,G}}$ increases, the incidence angle range grows (indicated by the black arrows), resulting in more light passing through the opening slit. The SNR maximum of 69.4 for the non-grazing range is reached at $\theta_{\mathrm{L,G}} = \theta_{\mathrm{L,G5}} = 63.6°$, corresponding to an incidence angle range of 15.6°. Figure 5.3(a) (red) illustrates that this occurs shortly before the Brewster angle of $\Delta R/R_{0,\mathrm{p}}$, where the peak orientation inverts. Consequently, only negative peaks contribute to the signal. Further increases in $\theta_{\mathrm{L,G}}$ reduce the SNR due to the growing influence of the positive peak orientation. This leads to a superposition of positive and negative peaks, which can be directly related to the band inversion. However, the noise levels improve (see Figure 5.6). A negative peak orientation was observed throughout the entire range of optimisation.

Figure 5.4(b), in blue, shows the optimisation of the grazing angle range. Here, the maximum incidence angle is at $\theta_{max} = 87°$ and $\theta_{\mathrm{L,N}}$ changes towards lower incidence angles. This limiting angle is defined by the non-grazing angle selection plate ($\mathrm{ASP_N}$). The SNR reaches its maximum of 51.3 at a limiting angle $\theta_{\mathrm{L,N}} = \theta_{\mathrm{L,N6}} = 65.9°$, which

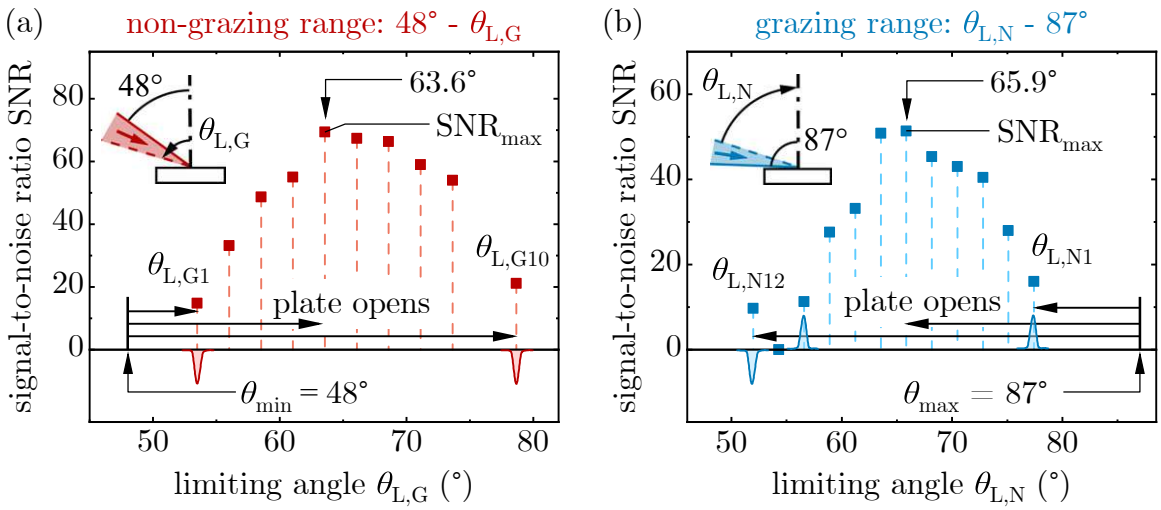

Figure 5.4: Measurement results of the SNR optimisation for the non-grazing and grazing range of 1 ML CO on the reduced TiO_2(110) surface acquired with 1000 scans and p-polarisation. The angle ranges are marked with arrows and the dashed vertical lines. (a) shows the SNR as a function of various non-grazing incidence angle ranges with fixed minimum incidence angle θ_{min} = 48° in the non-grazing range. The angle range (equivalent angle-selection plate slit width) was increased by changing $\theta_{L,G}$. (b) shows the SNR of different grazing incidence angle ranges. Grazing ranges from $\theta_{L,N}$ to θ_{max} = 87° were utilised. This figure is adapted from Ref. [34].

is almost at the position of the Brewster angle and corresponds to an incidence angle range of 21.1°. Up to this point, only peaks with positive orientation contribute to the signal, as illustrated in Figure 5.3. Further reduction of the limiting angle results in a disappearance of the signal in the spectrum (at $\theta_{L,N} = \theta_{L,N11}$ = 54.3°) and the SNR becoming zero. This indicates that the positive and negative signal contributions are equal. For lower limiting angles $\theta_{L,N} < 54.3°$, the negative peak contributions predominate.

In both cases, the optimum SNR is reached when the range limiting angle θ_L for either the non-grazing range or the grazing range are close to the the Brewster angle. When θ_L passes the Brewster angle, additional contributions from the reversed peaks decrease the SNR, although more light passes through the slit, decreasing the noise. Note that these results of the SNR optimisation are specific to TiO_2. Other materials exhibit a different behaviour of $\Delta R/R_0$ and require other optimum measurement parameters. Figure 5.4 showed that the limiting angles close to the Brewster angle are valid optimisation points. Because no band inversion is observed for s polarisation, no incidence angle range limit is needed to get the optimum SNR.

Figure 5.5 shows an analysis of the peak heights as function of the limiting angles. By following the plate opening direction in Figure 5.5(a) as indicated by black arrows, one can observe a maximum signal intensity of $\Delta R_p/R_{0,p} = 2.5 \times 10^{-3}$ at a low limiting

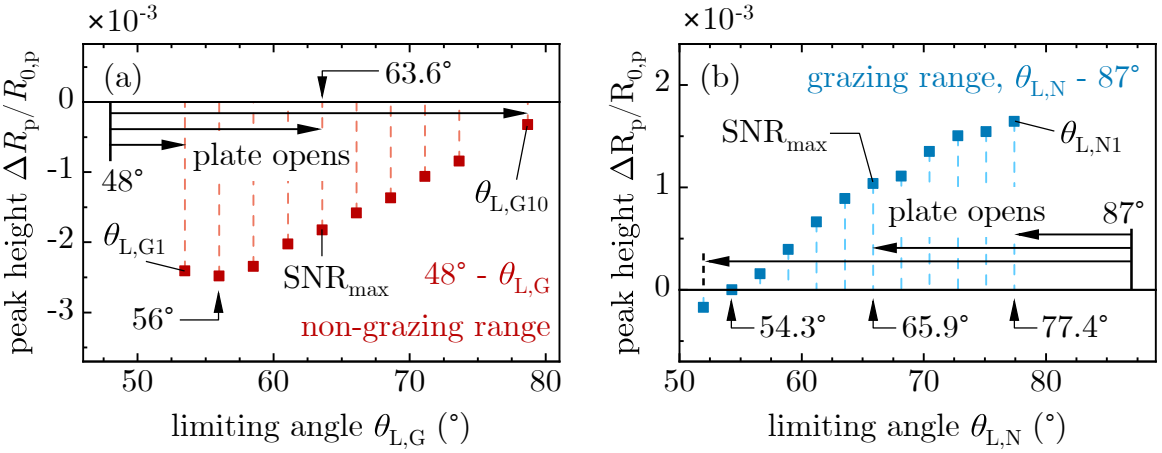

Figure 5.5: Peak height $\Delta R_p/R_{0,p}$ of 1 ML CO on TiO_2 measured with non-grazing and grazing ranges, 1000 scans and p-polarisation. The angle ranges are marked with arrows and vertical dashed lines. (a) shows the peak height as a function of various incidence angle ranges with fixed minimum incidence angle θ_{min} = 48° in the non-grazing range. The angle range was increased by changing $\theta = \theta_{L,G}$ (equivalent to an increasing angle-selection plate slit width).(b) shows the peak height resulting from various grazing incidence angle ranges. Grazing ranges from $\theta_{L,N}$to θ_{max} = 87° were utilised. The slit width was increased by altering $\theta_{L,N}$.

angle of $\theta_{L,G} = \theta_{L,G2}$ = 56°. For limiting angles $\theta_{L,G}$ > 56°, $\Delta R/R_0$ decreases due to smaller $\Delta R/R_0$ contributions at larger limiting angles (see Figure 5.3). However, increasing the slit width leads to higher system throughput and, consequently, the maximum SNR is found at a limiting angle greater than 56°. At SNR_{max} the peak height $\Delta R_p/R_{0,p} = 1.8 \times 10^{-3}$. The initial increase of the peak height suggests that changing θ_{min} to slightly higher values between $\theta_{min} < \theta < \theta_{L,N1}$ would increase the overall signal intensity (but not the SNR). Beyond the Brewster angle (66°), opposite peak orientations decrease the signal.

In the grazing range, depicted in Figure 5.5(b) and visualised in blue, the maximum $\Delta R_p/R_{0,p}$ value of 1.6×10^{-3} is achieved at the first measurement point of the optimisation at a limiting angle of $\theta_{L,N1}$ = 77.4°. Subsequently, the relative peak height continuously decreases with decreasing limiting angle $\theta_{L,N}$ (corresponds to increasing slit width). After the Brewster angle, the peak reverses its orientation, and the total peak height reaches zero at 54.3°. Here, the positive and negative peak contributions are equal. At the maximum SNR, the peak height $\Delta R_p/R_{0,p} = 1 \times 10^{-3}$ ($\theta_{L,N}$ = 65.9°). Here, the peak height is balanced with the throughput. Although, the noise level in the non-grazing range is slightly higher than in the grazing range, the factor of about 1.8 between the peak magnitudes dominates the difference in the maximum SNR on TiO_2. Thus, the non-grazing range yields the higher SNR.

A comparison of the calculated angle-dependent $\Delta R/R_0$ for p polarisation shown in Figure 5.3 measured values in Figure 5.5 confirms the trend of initially high peak

heights for the narrow angle ranges in the non-grazing and grazing range. As the angle range increases, smaller $|\Delta R/R_0|$ magnitudes reduce the average signal intensity. It is important to note that the measurement integrates over the angle range from $\theta_{\max}$ or $\theta_{\min}$ to θ_{L}. Differences between the calculated and measured $\Delta R_p/R_{0,p}$, shown in Figures 5.3 and 5.5, respectively, can be observed in the narrow angle ranges. In the case of the non-grazing range (visualised in red), one would expect the maximum peak height already at $\theta_{\mathrm{L,G1}}$, as the calculated $|\Delta R_p/R_{0,p}|$ value decreases for all angles between $\theta_{\mathrm{L,G1}}$ and the Brewster angle. For the grazing range (indicated in blue), the calculated $\Delta R_p/R_{0,p}$ curve would suggest an initial slight increase in the signal intensities followed by a decline. However, the measurement only shows a decreasing peak height with increasing angle range.

These results suggest minor discrepancies in the assumption for the effects influencing the ideal curves. Also, the error of angle selection (±2.5°, see Section 4.2.3) needs to be taken into account. Nevertheless, the outcome illustrates that the corrected $\Delta R_p/R_{0,p}$ calculation better represents the anticipated signal intensities than the ideal calculation shown in Figure 2.8. Aberrations in the IRAS system lead to a different behaviour of $\Delta R_p/R_{0,p}$ with the maximum peak heights shifted from around Brewster angles towards $\theta_{\max}$ and $\theta_{\min}$. This also influences how the incidence angle range has to be optimised for maximum SNR. The magnitude of these shifts depends manly on the polarisation leakage (skew aberration), as shown in Section 3.3.

In Figure 5.6, the RMS noise of the IRAS spectra is illustrated as a function of the partial intensity I_{p}, determined by integrating the reference spectrum R_0 from 1900 cm^{-1} to 2100 cm^{-1}. The data points shown in Figure 5.6 were obtained from the p-polarised IRAS optimisation spectra on TiO_2 used for in Figures 5.4 and 5.5. The noise decreases with increasing intensity according to $N_{\mathrm{RMS}} \propto 1/I_{\mathrm{p}}$ as indicated by the black curve (slope −1 in the log-log plot). This slope of the curve suggests additive noise, e.g., electronic noise. At higher partial intensities, the noise exhibits elevated fluctuations in the grazing range compared to the non-grazing range. Within the non-grazing range, the very grazing rays are excluded from the measurement (see Figure 3.1). The grazing rays exhibit a higher sensitivity to out-of-focus positions of the sample, potentially leading to the observed fluctuations due to sample vibrations. Hence, the non-grazing range exhibits greater stability than the grazing and full ranges. The maximum intensity observed in Figure 5.6 reaches about 25% of the detector saturation limit ($\mathrm{ADC\text{-}count}_{\mathrm{saturation}} = 32768$) and shows a minimal RMS noise of 1.4×10^{-5}. The relationship between ADC-count and I_{p} is described in Appendix A.4. This allows to estimate the RMS noise to about 4×10^{-6} for intensities close to the saturation limit of the detector (assuming the same measurement settings).

5.3.2 Spectra at High Resolution and Low Coverage

The spectra presented in Figure 5.7 were acquired with a high resolution of 1 cm^{-1} and the optimised incidence angle range of 48° to 64° at a J-stop of 6 mm. The effective J-stop of the IRAS setup (see equation 2.8) results in a resolution of 1.7 cm^{-1} at a J-stop

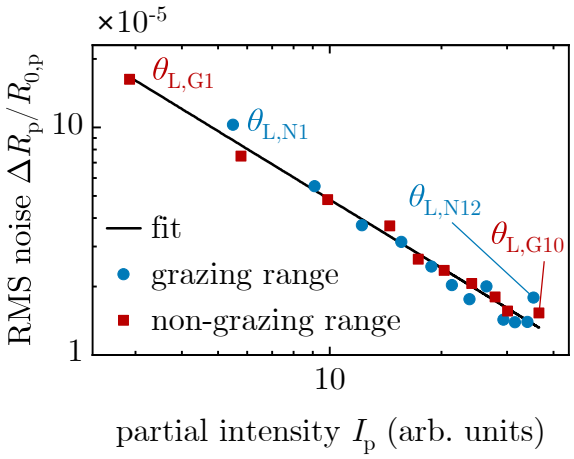

Figure 5.6: RMS noise evaluated from the $\Delta R_p/R_{0,p}$ optimisation spectra (aquired with 1000 scans) in respect of the intensity I_p evaluated between 1900 cm^{-1} and 2100 cm^{-1} from the associated reference spectra. Measurements performed in the grazing range (blue circles) and non-grazing range (red squares) are shown (see also Figure 5.4). The intensity variation was achieved by utilising different incidence angle ranges established the variation of the angle-selection plate slit width. The black curve shows the data fit according to $N_\mathrm{RMS} = 4.8 \times 10^{-4}/I_\mathrm{p}$.

diameter of 6 mm. However, this is a paraxial estimate, and considering the vignetting of peripheral rays and optical aberrations, a resolution of 1 cm^{-1} can be considered valid. The plot compares 1 ML and 0.1 ML CO adsorbed on the TiO_2(110) surface. A detailed view of the 0.1 ML peak is shown to the right in Figure 5.7. For 1 ML, the CO stretch is observed at 2181 cm^{-1} with a SNR of 43 achieved with 1000 scans for one single beam spectrum. The spectrum for 0.1 ML CO, obtained with 4000 scans, shows the main peak at 2187 cm^{-1} with a SNR of 11.6. An additional peak is visible at 2193 cm^{-1}, and no peak is observed at the 1 ML CO position (2181 cm^{-1}). The prominent peak for 0.1 ML CO is approximately seven times smaller in height compared to 1 ML CO, and the peak positions and shapes are consistent with previous work [18, 27]. Although there are minor differences in the peak position (2181 cm^{-1} in this thesis versus 2178 cm^{-1} in the literature for 1 ML CO), these variations may be due to a different reduction state of the TiO_2 sample. Wavenumber inaccuracies of the spectrometer can be excluded because the wavelength accuracy was checked by measuring a polystyrene film (inside the FTIR spectrometer) and ethylene ice [76] adsorbed on TiO_2. By comparing spectra obtained with 1000 and 4000 scans, we found that increasing the number of scans four times reduces the noise by a factor of 1.9, almost following the relationship of the noise being proportional to the square root of the number of scans, as expected. The result shows that the measurements of sub-monolayer coverages acquired with 1 cm^{-1} are possible within about 1.5 h measurement time. Compared to a resolution of 4 cm^{-1}, one scan with 1 cm^{-1} requires more time because the moving mirror in the spectrometer has to travel a larger distance.

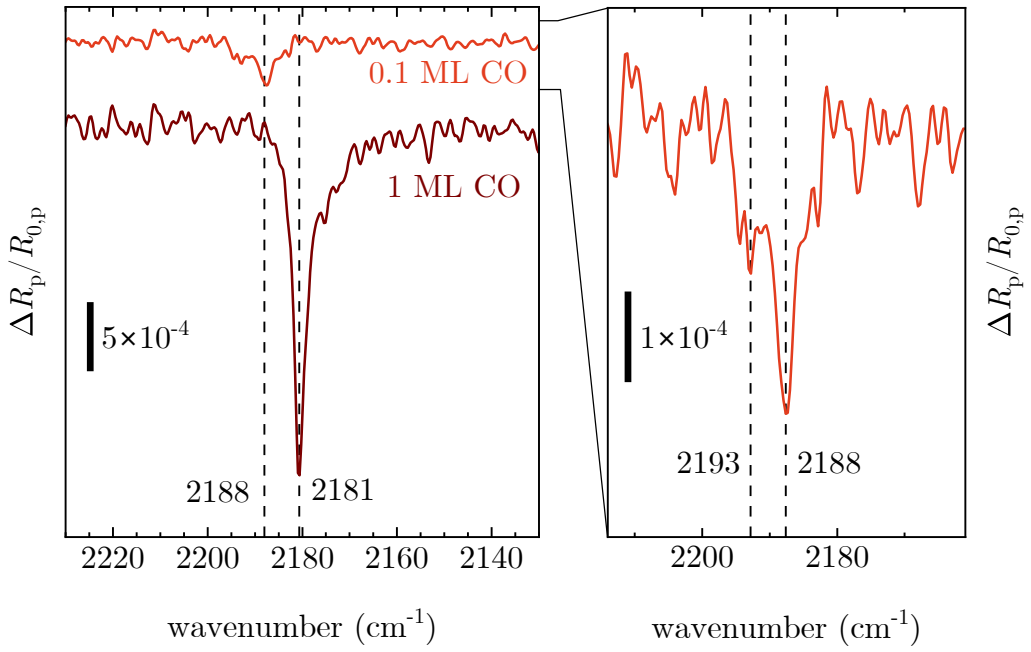

Figure 5.7: High-resolution p-polarised IRAS raw spectra of various CO coverages on reduced TiO_2(110). (a) shows a comparison of 1 ML (1.36 L) and 0.1 ML (0.14 L) CO obtained with 1000 and 4000 scans, respectively. The spectral resolution is 1 cm^{-1} and the beam incidence was along the [001] direction in non-grazing range (48° to 64°). The left graph shows a magnified view of 0.1 ML CO.

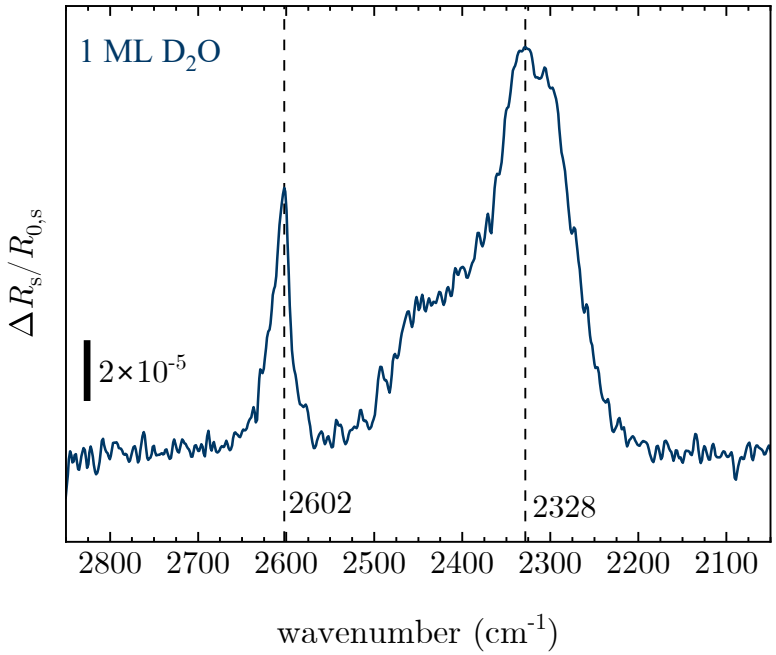

Figure 5.8: S-polarised spectrum of 1 ML D_2O on a hydroxylated and reduced $TiO_2(110)$ surface. The spectrum was acquired with the beam incidence along the [001] direction, a resolution of 4 cm^{-1} and 4000 scans. A baseline correction was applied to the spectrum. This figure is adapted from [34].

5.4 1 ML D_2O on $TiO_2(110)$

To evaluate the performance of the IRAS system for s polarisation, 1 ML (1.15 L) D_2O was dosed on the $TiO_2(110)$ surface. The vibrational modes on this model system are oriented mainly parallel to the surface, making it a suitable candidate for testing the IRAS system. This system has been thoroughly studied [16, 23] and provides a solid basis for benchmarking. As shown in Figure 3.16, for s polarisation, only one peak orientation is expected, allowing the full angle range of the IRAS system (from 48° to 87°) to be utilised. This maximises the throughput for the measurement, and no restriction of the IR beam by the angle-selection plates is necessary.

The sample was prepared according to the standard procedure outlined at the beginning of chapter 5.2. A reference spectrum was obtained after heating it to 950 K and then cooling it to 45.9 K. Following hydroxylation at 315.4 K with 1.5 L of D_2O, the reduced $TiO_2(110)$ surface was further treated by adsorbing 1 ML D_2O at 186.4 K. Here, 1 ML corresponds to a gas dose of 1.1 L. Subsequently, a sample spectrum was recorded at 45.9 K with a resolution of 4 cm^{-1} and 4000 scans taking about 20 minutes. The resulting IRAS spectrum is shown in Figure 5.8. Two peaks are visible. The first peak is located at 2602 cm^{-1}. A second broader feature at higher wavenumbers has its maximum of $\Delta R_s/R_{0,s} = 1.4 \times 10^{-4}$ at 2328 cm^{-1}, exhibiting a SNR of 64.5. The overall spectrum shape was already observed in previous work [23].

resolution (cm^{-1})	J-stop (mm)	No. scans	adsorbate	angle range	pol.	RMS noise	rel. peak intensity	SNR
4	6	1000	1 ML CO	48°–87°	p	1.23×10^{-5}	3.00×10^{-4}	24.4
4	6	1000	1 ML CO	48°–64°	p	2.63×10^{-5}	1.83×10^{-3}	69.4
4	6	1000	1 ML CO	66°–87°	p	2.02×10^{-5}	1.04×10^{-3}	51.3
1	6	4000	0.1 ML CO	48°–64°	p	3.01×10^{-5}	3.50×10^{-4}	11.6
1	6	1000	1 ML CO	48°–64°	p	5.74×10^{-5}	2.50×10^{-3}	43.6
4	3	4000	1 ML D_2O	48°–87°	s	2.17×10^{-6}	1.40×10^{-4}	64.5

Table 5.2: Collection of the key values from the $\Delta R/R_0$ spectra of CO and D_2O on reduced $TiO_2(110)$ shown in the Figures 5.4, 5.7 and 5.8. The RMS noise values were evaluated with the OPUS software [40] using a parabolic fit in the wavenumber range from 1900 cm^{-1} to 2100 cm^{-1}. The measurement polarisation (pol.) is given in the table.

5.5 Summary

The spectra presented in this chapter and the analysis of the signal-to-noise ratio (SNR) verify the functionality of the newly developed IRAS system and demonstrate its excellent performance. The angle-selection mechanism proves to be an exceptional tool for precisely adjusting the measurement parameters to their optimal settings. P-polarised measurements in the non-grazing range achieved the highest SNR for CO adsorbed on the $TiO_2(110)$ surface compared to the grazing and full range. For s polarisation, utilising the full range with maximum throughput can achieve minimal noise levels. All the essential values of the benchmark spectra are summarised in Table 5.2. The plots showing the results with varying incidence angle ranges (see Figures 5.4 and 5.5) illustrate the necessity of accounting for polarisation aberration in the system. This chapter emphasises that the developed IRAS system meets the high-performance criteria established prior to its development.

CHAPTER 6

DISCUSSION & OUTLOOK

External boundary conditions often limit the design of a measurement system. The IRAS setup presented in this thesis is designed to fit into an operational UHV chamber [62, 63]. Spatial restrictions and limited space in the laboratory had to be accounted for. Therefore, further room for improvement, e.g., enhanced throughput or reduced depolarisation, is possible when no restrictions are given. Also, ideas emerging at a point too late in the development process could not be realised any more, as the complementation of the project was prioritised. Furthermore, technical developments already used for specific IR spectroscopy applications present room for further development. However, the current state of the art enables only particular applications, and additional development is necessary until these technical developments are applicable in a multi-purpose measurement system. One example of a currently developed technique is the application of a laser for IRAS.

6.1 Throughput Improvement

The illumination area in the detector focus exceeds the size of the detector element at a J-stop setting of 6 mm (see sections 3.1.2 and 5.1). Additionally, the detector field of view is narrower than the actual focusing cone angle of the detector mirror. Both of these factors contribute to a reduction in throughput. Considering the constraints imposed by the source optics and the detector itself, some intensity reduction is

expected and in accordance with the concept of étendue. Consequently, replacing components with improved performance seems to present a greater potential for enhancing throughput rather than adjusting the optical path geometry.

Reducing reflective losses originating from mirrors and windows within the optical system can increase the throughput. This could be realised, i.e., by fewer optical surfaces or different materials of the optical components.

6.1.1 Different Detector

A potential improvement approach utilising the current optical design is possible by enlarging the detector element to $2 \times 2\,\mathrm{mm}^2$. In this case, the detector element would not cut the illumination area in the detector focus. This would enhance the intensity throughput of the system by about 33 % and minimise the sensitivity to misalignments of the optical system and mechanical vibrations. However, larger detector elements are typically less sensitive. Furthermore, a larger detector element leads to increased detection of light reflected off the adsorbate-free areas on the sample, reducing $\Delta R/R_0$ peak height at grazing angles.

6.1.2 IR Source improvement

The IRAS setup uses a glowbar (SiC rod) as an MIR source, typically operating at temperatures around 1200 to 1400 K. Changing to an external source operated at a higher temperature would improve the intensity. It is important to note that maintaining a large solid angle remains a crucial factor when considering an external source.

The spectrometer is designed to accommodate external sources through side ports. One potential configuration involves utilising the side port beside the bellows that connects the spectrometer to the IRAS system. By using this port, the IR beam is directed through the J-stop of the spectrometer. Commercial solutions, e.g. provided by Bruker or custom designs like a high-temperature graphite source [85], are viable options. It is worth noting that these sources typically have an encapsulated design and transmit IR radiation through an IR transparent window.

Alternatively, connecting an external source at the port to the left of the collimation mirror on the back side of the spectrometer is another option, which would require the implementation of an additional J-stop. If high resolutions (better than $1.7\,\mathrm{cm}^{-1}$– see Section 3.1.2) are not needed and the IRAS optics as presented is used, a fixed J-stop diameter can be utilised. In this case, the angle-selection plates in the system could also be used to control the system throughput, avoiding detector saturation.

6.2 Depolarisation Reduction

In Section 3.3.1, it was shown that depolarisation significantly reduces the attainable $\Delta R/R_0$ signal for p-polarised measurements. The high numerical aperture of the system

leads to depolarisation of the IR beam (skew aberration). After polarising the IR light, in the current design, the IR beam gets reflected by two mirror surfaces until it reaches the sample. Each mirror surface contributes to the depolarisation Γ.

A reduced depolarisation results in less s-polarised infrared light "leaking" into p-polarised measurements and vice versa. On non-metallic samples, s-polarised light features higher reflectivity than p-polarised light across almost the entire angle range from 0 to 90° (see Figure 2.6). Therefore, a reduced depolarisation lowers the detected s-polarised intensity in p-polarised measurements. With the noise of $\Delta R/R_0$ scaling inversely proportional to the intensity, as depicted in Figure 5.6, reduced depolarisation might not lead to significant enhancements in the signal-to-noise ratio (SNR) as long as the intensity on the detector remains below saturation. However, reduced depolarisation might contribute to higher stability. In addition, reduced depolarisation will mitigate the risk of misinterpretation of the direction of the dipole moment.

Moving the polariser from its current position one focus point closer to the sample (15 mm before the beam shaping slit) would reduce the number of mirror surfaces between the polariser and sample from two to one. With this position of the polariser, a reduction of the depolarisation from $\Gamma = 0.21$ to around 0.1 can be expected. This would decrease s-polarised IR light, "leaking" into the p-polarised measurements and vice versa. In the case of p-polarised measurements, an estimated increase in the $\Delta R/R_0$ magnitude by a factor of about two can be expected in the grazing and non-grazing measurement range, as used for the measurements in Figure 5.2. The reduction of the intensity on the detector due to a cleaner polarisation of the IR beam reaching the sample is not expected to lead to an improved SNR unless the saturation limit of the detector is reached.

Another possibility to improve the polarisation of the light hitting the sample requires a change of the optics, specifically the orientation of the input mirror and the illumination mirror to each other. Currently, the input and illumination mirrors are designed such that the shorter focal lengths of the two mirrors point to the same side (see Figure 3.1). The current configuration was chosen due to spatial restrictions given by the UHV chamber. Orienting the two mirrors with their short focal lengths pointing in opposite directions, i.e., a Z-like beam path, improves the depolarisation to about 0.1 or slightly better. In this configuration, the polarisation aberrations of the two mirrors partly compensate for each other. The polariser is kept in the same position between the spectrometer-link and the input mirror, where the beam is narrow enough to pass through the clear aperture of the polariser.

The best option for minimal depolarisation would require placing the polariser between the illumination mirror and the sample ($\Gamma = 0.005$ with the polariser used in the IRAS setup). However, this adds complexity to the design, as the polarisation must be changed in an ultra-high vacuum environment, and the space in the chamber is very restricted. Consequently, for such low depolarisations, the $\Delta R/R_0$ curve for p polarisation would show substantially stronger extrema close to the Brewster angle

(see Figure 3.5 and 3.6), which may allow using the partial incidence-angle range (see Figure 5.3) for the measurement to reach a high $\Delta R/R_0$ value. In this configuration, one limiting angle is set close to the Brewster angle, and the second is adjusted from $\theta_{\max}$ or $\theta_{\min}$ towards the Brewster angle. This impacts the throughput of the system and leads to smaller SNR improvements than one would expect from only considering the peak heights. Since Figure 5.6 suggests that the noise of $\Delta R/R_0$ scales inversely proportional to the intensity, a reduction of the angle range to maximise $\Delta R/R_0$ may lead to a decreased SNR.

6.3 Utilising the Angle-Selection Plates to Avoid Detector Saturation

When the system throughput exceeds the detector saturation limit, it is necessary to decrease the throughput. The intensity on the detector can be reduced by either the J-stop of the spectrometer (see Figure 2.2) or the angle-selection plates of the IRAS system, described in Section 4.2.3. In Section 5.2, it was noted that not to overshoot 80 % of the detector saturation limit in s-polarised measurements, the J-stop diameter was reduced from 6 to 3 mm. This adjustment does not impact the incidence angle range but the throughput (and improves the resolution).

Moving the angle-selection plates in and out of the IR beam allows the system throughput to be adjusted, and at the same time, the peak height can be optimised by choosing an appropriate incidence angle range. However, the exact setting of the angle range depends on the trend of $\Delta R/R_0$. The corrected $\Delta R_s/R_{0,s}$, depicted in Figure 3.12, shows this signal rising while the incidence angle decreases. Stronger $\Delta R/R_0$ signals are achieved by setting the grazing angle limit $\theta_{\mathrm{L,G}}$ to exclude grazing angles where $\Delta R/R_0$ is low. The average $\Delta R_s/R_{0,s}$ is higher for the non-grazing range than for the full angle range, leading to an improved SNR because the throughput is at its maximum. Also, the calculation with the system-specific corrections included, as shown in Figure 3.16, benefits from the utilisation of the non-grazing range instead of reducing the J-stop diameter to control the throughput of the system.

In the presented IRAS setup, detector saturation for measurements on bulk oxides can typically occur for s polarisation, not for p polarisation. This is because p polarisation generally features a lower reflectivity (see Figure 2.6) and is affected by band inversion, necessitating a limited incidence angle range for optimised SNR. Nevertheless, materials with a high refractive index, where the Brewster angle is shifted to grazing angles or measurements using a highly sensitive detector, would benefit from the previous method when measuring also p-polarised IRAS. Also, setups with high light intensity, e.g. systems utilising a source with a higher temperature than the current glowbar, would benefit from a limited incidence angle range.

6.4 Reduction of the Vicinity Illumination

As stated in Section 2.1, the vicinity illumination leads to a decreased achievable peak height $\Delta R/R_0$, particularly for incidence angles exceeding 65°. Further reduction of the vicinity illumination can be achieved by improving the design of the illumination-shaping slit or by optimising the adsorption geometry on the sample. However, in case of the $\Delta R/R_0$ noise scaling inversely proportional to the intensity, as shown in Figure 5.6, no significant SNR improvement is expected when the intensity on the detector remains below saturation.

6.4.1 Advanced Illumination-Shaping Slit

The illumination-shaping slit in the system reduces the light detected, which is reflected by the vicinity (adsorbate-free area) on the sample. Thus, the slit increases the $\Delta R/R_0$ peak height (see Section 3.3.4). The illumination-shaping slit in the presented setup is fixed. The current slit settings are a compromise between grazing and non-grazing angles, to maintain control over the vicinity illumination while not too badly affecting the system throughput over the whole angle range. By replacing the fixed illumination-shaping slit with a motorised slit, it is possible to achieve more control over the vicinity illumination. It allows for the selection of the optimal slit size to increase the IRAS system throughput when using non-grazing angles. In the current system, the illumination length along the incidence plane is smaller than the MB spot for incidence angles smaller than 65° (see Section 3.3.4). These measurements would benefit from a wider slit size. In contrast, narrower slits would be beneficial for measurements using grazing illumination, reducing the vicinity illumination. For each angle range, the slit opening must be balanced with the system throughput.

In addition, minor improvements can be realised by a change of the optics where the short focal lengths of the input mirror and the illumination mirror point to different sides (Z-like path), as described in Section 6.2. This mirror layout compensates for some optical aberrations and produces a sharper illumination cut on the sample. Furthermore, concave-shaped illumination-shaping plates would shape the sample illumination to fit the circular adsorbate area better, reducing the vicinity illumination. All these changes would be beneficial for measurements with s and p polarisation.

6.4.2 Dosing under an Angle

When dosing adsorbates, the standard procedure is to orient the sample surface perpendicular to the MB beam axis. This allows for dosing the adsorbates onto a circular area in the centre of the sample, as depicted in Figure 3.13(a). Dosing at an angle would cause the MB spot to expand along the plane of incidence of the IR light. The circular area would then change into an elliptical shape with an increased long axis. The larger MB spot would decrease the vicinity region on the sample, leading to less IR radiation being reflected from areas without adsorbates. Consequently, the reduction in peak heights due to illumination of the vicinity is reduced. The elliptical adsorbate

area would also allow an increase in the slit size of the illumination-shaping slit, and more light would pass through the system, improving the SNR of the measurements. Due to different distances from the orifice of the MB source this also decreases the homogeneity of the adsorbate coverage.

6.5 Improved Light Detection

As shown in Section 3.3.4, IR light is reflected from the MB spot, and the vicinity around the MB spot (adsorbate-free area) is detected simultaneously at the detector, as shown in Section 3.3.4. The light reflected from the different areas on the sample also hits the detector element at different locations, provided the detector element is in the focus point. This fact can be exploited by replacing the single detector element with an array of pixels. Then, it is possible to separate the vicinity illumination from the MB spot illumination to reduce the effect of the vicinity illumination heavily by not measuring signals from the pixels detecting light reflected from the vicinity. This would also allow to remove the illumination-shaping slit. To eliminate this effect, it might be necessary to exclude the sample regions on the border between the MB spot and the vicinity from the measurement, as mixing the reflected light from both regions is likely to occur due to optical aberrations.

This idea could be expanded, and the signal from pixels detecting light reflected from the vicinity could be used to acquire the reference spectrum simultaneously with the sample spectrum. The sample spectrum is measured by the pixels detecting light reflected from the MB spot. However, the current state-of-the-art array detectors lack sensitivity and suffer from high noise. Therefore, they have not yet fulfilled the high sensitivity requirement to detect low coverages of samples with IRAS. Another option would be to utilise two detector elements, such that one element detects light from the MB spot and the other from the adsorbate-free area.

6.6 Improved Incidence Angle Selection

The angle-selection plates are a key component of the IRAS system. Currently, these plates are operated using manual linear manipulators from UHV Design. However, it is possible to enhance their functionality by adding motors. UHV Design offers a modification kit for this purpose. Automating these manipulators would allow for the full automation of IRAS measurements, expanding the existing partial automation of the surface chemistry chamber.

The main application of the angle-selection plates is to optimise the SNR in IRAS measurements. In the future, the function of this aperture system can be further expanded to measure the orientation of the dipole moment (and, thus, the molecular bond) on the surface. For this, angle-resolved IRAS measurements can be performed. Subsequently, the spectra have to be analysed based on peak heights of the $\Delta R/R_0$ and the ΔR with respect to the incidence angle. Additionally, calculations of $\Delta R/R_0$ and

ΔR at the resonance frequency must be performed and fitted to the evaluated dataset. The calculation formulas must include a parameter (used as a fitting parameter) for the orientation of the dipole moment on the surface. Currently, the calculation formulas only cover the three main cases (p$\perp$, p$\parallel$, s$\parallel$). Note that the calculation also requires an exact knowledge of the angle-dependent intensity on the sample and the illumination geometry on the sample (vicinity illumination). The IRAS spectra, dependent on the incidence angle, can be measured in two ways.

The first method involves fixing one angle-selection plate to allow incidence angles of θ_{min} or θ_{max}. The second angle-selection plate is moved to alter the limiting angle, as shown in Section 5.3.1, and allows for recording IRAS spectra in two angle ranges (non-grazing and grazing) where every measurement point corresponds to a different incidence angle range. This method yields good SNR ratios and is well-suited for measuring low coverages. However, measuring over large angle ranges, including crossing the Brewster angle, increases the complexity of the data fit due to the contribution of signals from various incidence angles.

The second measurement procedure involves moving a narrow constant angle range (a slit) across the full angle range from θ_{min} to θ_{max}, measuring the angle-resolved spectra. This approach simplifies the fit procedure because fewer incidence angles than in the first case contribute to the signal. However, due to the narrow slit used, the intensity throughput is limited, making it challenging to resolve small signals efficiently.

The third method is to perform one measurement above the Brewster angle and one below and then use this to deduce p$\perp$ and p$\parallel$.

6.7 Lowering of the Electrical Noise

In Section 5.3.1 it was noted that the trend of the noise plotted over the intensity (shown in Figure 5.6) suggests electronic noise as the main contribution to the noise. Reducing the noise might be possible by replacing the operational amplifier in the first amplification stage with a model featuring lower noise levels.

6.8 IRAS with an IR laser

Another approach to increase the IRAS performance is to utilise a laser. This method offers the advantage of a small beam diameter with low divergence while delivering high intensity. Therefore, the laser can be directed onto the sample surface under a precise incidence angle without sacrificing throughput. The low divergence, high grade of polarisation and small angle spread lead to higher signal intensities. This simplifies also the optimisation of the SNR. Also, angle-dependent studies of adsorbates are easier to realise.

Quantum cascade lasers (QCLs) have shown promising potential for measurements within limited wavenumber ranges and are already in use [86]. Tunable IR lasers can be employed to cover broader measurement ranges. However, current tunable IR lasers do not cover the entire MIR range and do not fulfil the stability requirements for highly sensitive measurements. Another option is to use a supercontinuum laser as an IR source. Because such a laser outputs a broad spectrum it has to be guided through the interferometer of the FTIR to perform measurements, in contrast to the QCL and tunable broadband laser mentioned before.

The $\Delta R/R_0$ signal for p polarisation is significantly influenced by the grade of depolarisation of the laser beam reaching the sample. Assuming similar measurement parameters to those employed in the measurements presented in Section 5.3, a comparable IR intensity reaching the detector (reflected under an incidence angle of $\theta \approx 70°$ on the sample) and a low depolarisation of 0.005 of the laser, a SNR improvement by up to a factor of about 15 may be achieved for the case p$\perp$.

Using a laser, a two-beam setup can be realised [87], with one beam directed over a clean sample area to capture the reference spectrum and the second beam directed over the sample area of interest to obtain the sample spectrum. Both measurements can be performed simultaneously.

CHAPTER 7

CONCLUSION

This thesis introduces a newly developed IRAS setup for analysing adsorbates on non-metallic substrates, including dielectric materials. The system was specifically designed to investigate metal oxide single-crystals under UHV conditions, with the ability to control the light incidence angle on the sample. The new setup delivers high sensitivity and signal-to-noise ratios with the detection of adsorbates at sub-monolayer levels on small adsorbate areas. The optimised design was achieved by establishing three fundamental design parameters: throughput optimisation, optimal incidence angle range and stability.

Firstly, the optical design of the IRAS setup was carefully optimised to maximise light throughput. A key focus was placed on utilising a short focal length for the illumination and collector mirror, resulting in a high numerical aperture and precise illumination area on the sample. This concentration of illumination on the molecular beam spot at the centre of the sample minimises losses from grazing light incidence. It reduces the signal weakening of $\Delta R/R_0$ caused by IR light reflected and detected from the adsorbate-free area around the sample. Additionally, an illumination-shaping slit has been incorporated into the IRAS system to control the sample illumination. For low incidence angles ($\theta < 65°$), this slit effectively eliminates vicinity illumination, maintaining signal intensities. However, for very grazing angles, this slit does not fully suppress the illumination of the uncovered surface (see Section 3.3.4).

Also, careful selection of the optical materials and the implementation of intermediate focal points contribute to the high throughput compared with previous designs. The optical design was mainly restricted by the spatial constraints given by the UHV chamber and the laboratory space. Therefore, this still leaves room for improvement when no such constraints have to be considered.

The calculation of the normalised reflectivity difference $\Delta R/R_0$ including effects in the real system represents the foundation for the second design parameter. The optimal range of incidence angles is achieved using an angle-selection mechanism. This mechanism enables selecting the best range of incidence angles to ensure the highest signal-to-noise ratio, whether for different materials, measurement polarisations, or orientations of dipole moments. When using p polarisation, choosing an incidence angle range that does not cross the Brewster angle (which changes with the refractive index of the material) allows for a balance between throughput and signal intensity to achieve a maximum of the signal-to-noise ratio. This prevents the simultaneous measurement of positive and negative signals that result from band inversion effects on non-metallic substrates. Generally, s polarisation measurements exhibit lower signals than those measured with p polarisation. For s polarisation, utilising the full angle range provides the advantage of lower noise levels due to enhanced throughput (as long as the intensity stays below the detector saturation limit).

Ensuring the stability of the IRAS system was a critical aspect of the design. The central flange design is the key concept behind achieving this goal. All components are precisely connected and referenced to the central flange (DN 150 CF) of the IRAS setup. Rigid support beams in high and ultra-high vacuum securely hold the two optical platforms (detection and sample-focus platform) in place. The use of milled corner joints, pinned connections, and spring-loaded screwing ensures the exact positioning of the optical components, even over extended periods. This reduces the need for realignment, even after the UHV setup undergoes a bakeout. Additionally, minimising the use of kinematic mounts in the system enhances stability. These measures collectively improve the long-term stability of the system and ensure consistent baselines for successive measurements.

In addition to the performance-increasing measures, user-friendliness was a criterion throughout the design process. The implementation of the sample-position finder allows the user to measure the position of the sample precisely at any time. This benefits the IRAS measurements and improves other measurements conducted in the surface chemistry chamber. Furthermore, the unique design of the high vacuum support beam with minimised material in the cross section and the connected water cooling system eliminates the need to disassemble the IRAS system for UHV system bakeout, ensuring seamless operation.

Considering these features and utilising the different incidence angle ranges achieved a maximum SNR of up to about 70 at reasonably short measurement times. Here, 1 ML CO adsorbed on rutile $TiO_2(110)$ in the non-grazing incidence angle range was measured

with a resolution of $4\,\mathrm{cm}^{-1}$ and 1000 scans within 5 minutes including the reference spectrum. Also, sub-monolayer sensitivity is reached within minutes of measurement time. A similar signal-to-noise ratio performance was achieved using s-polarised IRAS to acquire spectra of 1 ML D_2O on a hydroxylated $TiO_2(110)$, utilising the full incidence angle range with the advantage of lower noise levels.

The UHV IRAS system presented in this thesis shows high performance on bulk oxide single crystals, with additional features implemented to make it a versatile, user-friendly system adaptable and optimisable to various measurement conditions.

APPENDIX

A.1 Additional Calculations

A.1.1 Angle Spread for p∥

Figure A.1.1 shows the effect of angle spread applied in different strengths to the ideal calculation of $\Delta R/R_0$ for p-polarised light and a surface-parallel dipole moment in incidence plane. The calculation was performed for an adsorbate on TiO_2. Here, the reflectivities of the adsorbate-covered and the clean surface were integrated in the range of $\pm\kappa$ around θ and then the normalised reflectivity difference $\Delta R/R_0$ was calculated. The calculation parameters are defined in Section 2.4.2.

A.1.2 $\Delta R/R_0$ on Fe_3O_4 with System-Specific Corrections

Figure A.1.2 shows the normalised reflectivity difference $\Delta R/R_0$ on Fe_3O_4 for an angle spread of $\kappa = \pm 2°$ (see Section 3.3.2), the system-specific depolarisation of $\Gamma = 0.21$ (see Section 3.3.1) and the vicinity illumination discussed in Section 3.3.4 (compare to $\Delta R/R_0$ on TiO_2 shown in Figure 3.16). According to the calculation, the maximum peak height for p-polarisation and a perpendicular dipole moment occurs at non-grazing angles and is in the order of 10^{-3}. Parallel dipole moments result in smaller $\Delta R/R_0$ values in the order of 10^{-4} exhibiting their maxima at low incidence angles. The calculation parameters are defined in Section 2.4.2.

A.2 Preliminary $\Delta R/R_0$ and ΔR Fit

The $\Delta R/R_0$ (from Figure 5.5 of the main text) and ΔR curves (from the experiment of Figure 5.5) for CO on $TiO_2(110)$ were fitted using the following parameters: $\kappa = \pm 2$, $\Gamma = 0.21$. For obtaining a good fit, it was required to shift the simulated IR intensities

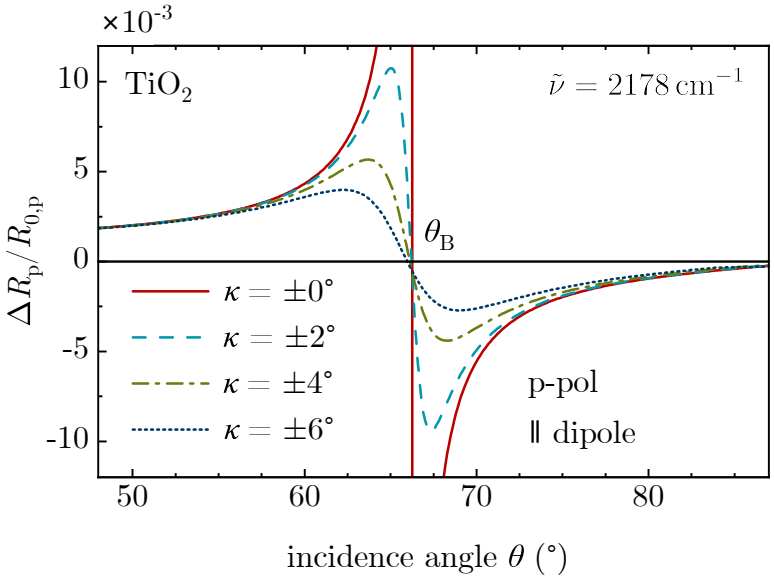

Figure A.1.1: Various angle spreads influencing the ideal differential reflectivity. Calculated for p-polarized light reflected on TiO_2 with an dipole moment parallel to the surface at $\tilde{\nu}$ = 2178 cm^{-1}. The red, solid curve indicates the ideal calculation with no angle spread (κ = ±0°) of the IR beam. The light blue, dashed curve shows a angle spread of κ = ±2° applied to the ideal curve, the green, dash-dotted and the dark blue, dotted curve show a angle spread of κ = ±4° and κ = ±6°, respectively. θ_B marks the Brewster angle of the uncorrected calculation.

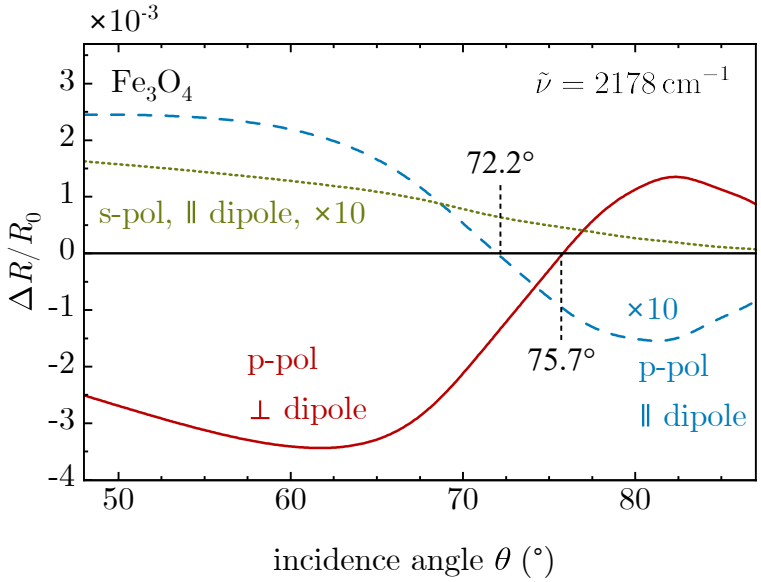

Figure A.1.2: Normalised reflectivity difference for an adsorbate on Fe_3O_4 at $\tilde{\nu} = 2178\,\mathrm{cm}^{-1}$ with the setup specific corrections. These are $\Gamma = 0.21$, $\kappa = \pm 2°$ and the effect of the vicinity illumination. The plot shows p polarisation with a dipole moment normal to the surface (red, solid), p polarisation with surface-parallel dipole (blue, dashed) and s polarisation with a surface-parallel dipole moment (greed, dotted). The latter two are multiplied by 10 to enhance clarity. The black (dashed) lines indicate the zero crossings.

(I_{full}, I_{MB}, I_{V} – see Figure 3.13) by $\Delta\theta = -5°$ to lower incidence angles and scale the magnitude to fit the ΔR plots shown below. Also a changed minimum illumination angle of $\theta_{\text{min}} = 50°$ instead of 48° was required to obtain a better fit. A total angle range of 39° was assumed. Then $\Delta R/R_0$ and ΔR were integrated from θ_{min} to $\theta_{\text{L,G}}$ or θ_{max} to $\theta_{\text{L,N}}$ to calculate the fit curve.

The fits, shown in the Figures A.2.3 and A.2.4, are only utilized to estimate the surface polarisability and to determine if the depolarisation and the vicinity illumination are valid concepts. The fit parameters were manually adjusted. For a more detailed interpretation, a thorough fit of the incidence angle dependent intensity reflected off the sample which includes an incidence angle dependent depolarisation would be necessary and an automated fitting procedure would need to be established.

It is important to note that ΔR depends on the intensity and is not decreased by the vicinity illumination. $\Delta R/R_0$ is not affected by the overall intensity as it is normalised to the reflectivity of the clean sample. However, the ratio between the illumination intensity of the MB spot and the entire sample (as shown in Figure 3.13) significantly impacts the peak height at grazing angles. Fitting $\Delta R/R_0$ data points provides a better understanding of the vicinity illumination and how the effects in the real system influence the ideal curve. Note that the detected vicinity illumination is highly dependent on the alignment of the detector element. The preliminary fit shows that the depolarisation and vicinity illumination are valid concepts to estimate the effects in the real system.

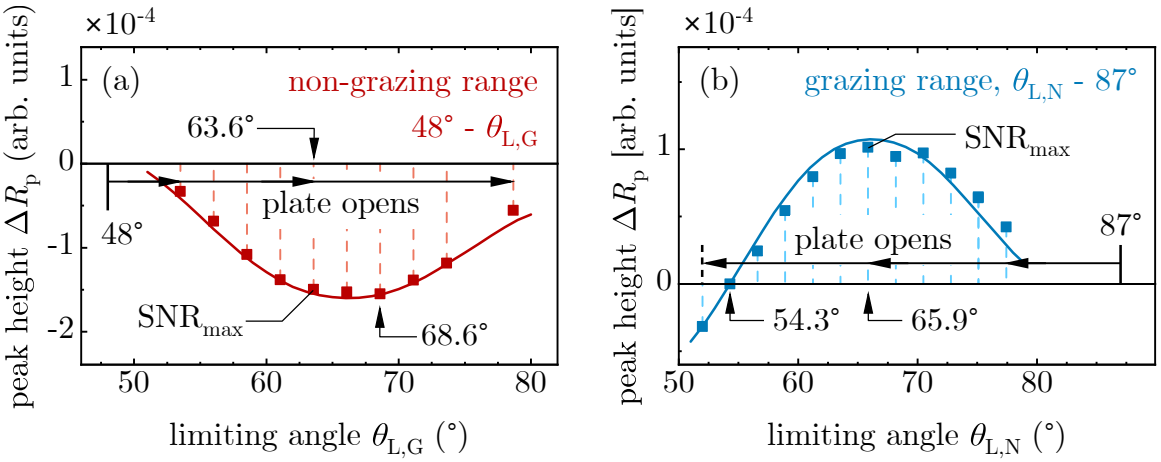

Figure A.2.3: Measured and calculated peak height in the ΔR_{p} spectra of 1 ML CO on TiO_2 for non-grazing and grazing ranges, with p polarisation. The measurement is described in Section 5.3.1. (a) shows the calculated (solid red line) and the measured ΔR_{p} peak height (red squares) as a function of various incidence angle ranges. (b) shows the calculated (solid blue line) and the measured ΔR_{p} peak height (blue squares) resulting from various grazing incidence angle ranges.

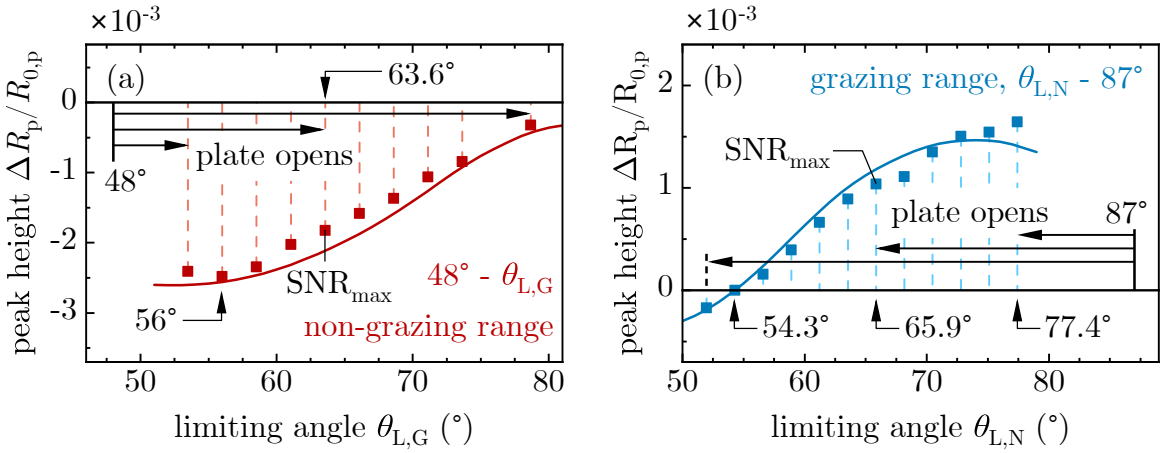

Figure A.2.4: Measured and calculated peak height in the $\Delta R_p/R_{0,p}$ spectra of 1 ML CO on TiO_2 for non-grazing and grazing ranges, with p polarisation. The measurement is described in Section 5.3.1 and depicted in Figure 5.5. (a) shows the calculated (solid red line) and the measured $\Delta R_p/R_{0,p}$ peak height (red squares) as a function of various incidence angle ranges. (b) shows the calculated (solid blue line) and the measured $\Delta R_p/R_{0,p}$ peak height (blue squares) resulting from various grazing incidence angle ranges.

A.3 Angle Selection Table

ap_i	$\theta_\mathrm{L,N}(ap_\mathrm{N})$ [°]	$\theta_\mathrm{L,G}(ap_\mathrm{G})$ [°]	ap_i	$\theta_\mathrm{L,N}(ap_\mathrm{N})$ [°]	$\theta_\mathrm{L,G}(ap_\mathrm{G})$ [°]
2.1	89.5	—	4.6	66.3	69.0
2.2	88.5	—	4.7	65.4	68.0
2.3	87.6	—	4.8	64.5	67.0
2.4	86.7	—	4.9	63.6	66.0
2.5	85.8	—	5	62.6	65.0
2.6	84.8	89.1	5.1	61.7	64.0
2.7	83.9	88.1	5.2	60.8	62.9
2.8	83.0	87.1	5.3	59.9	61.9
2.9	82.1	86.1	5.4	58.9	60.9
3	81.1	85.1	5.5	58.0	59.9
3.1	80.2	84.1	5.6	57.1	58.9
3.2	79.3	83.1	5.7	56.2	57.9
3.3	78.4	82.1	5.8	55.2	56.9
3.4	77.4	81.1	5.9	54.3	55.9
3.5	76.5	80.1	6	53.4	54.9
3.6	75.6	79.1	6.1	52.4	53.9
3.7	74.7	78.1	6.2	51.5	52.9
3.8	73.7	77.0	6.3	50.6	51.9
3.9	72.8	76.0	6.4	49.7	50.9
4	71.9	75.0	6.5	48.7	49.9
4.1	71.0	74.0	6.6	47.8	48.8
4.2	70.0	73.0	6.7	46.9	47.8
4.3	69.1	72.0	6.8	46.0	46.8
4.4	68.2	71.0	6.9	45.0	45.8
4.5	67.3	70.0	7	44.1	44.8

Table 1: Relation of the aperture position ap_i (see Figure 4.10) to the range limiting angle $\theta_\mathrm{L,N}$ (for non-grazing angles) or $\theta_\mathrm{L,G}$ (for grazing angles), respectively. The position of the high rotator is ap_G and defines the grazing angle limit $\theta_\mathrm{L,G}$. It is changed by the manipulator at the right side, and the full aperture blade is moved. The position of the low rotator is ap_N and is related to the non-grazing angle limit $\theta_\mathrm{L,N}$. The left-sided manipulator changes the angle limit $\theta_\mathrm{L,N}$ and moves the aperture plate with the hole.

A.4 ADC-Count vs. Intensity

Figure A.4.5 shows how the ADC-count, accessed in the OPUS software [40] to check the signal, is related to the intensity in the single beam spectrum. In this figure, the reference spectrum R_0 was integrated within the range of 1900 cm^{-1} and 2100 cm^{-1} to evaluate the partial intensity I_p of various IRAS measurements. One can observe a linear relation between the ADC-count and the partial intensity according to ADC-count = $220.8 \cdot I_p - 0.77$. Hence, the ADC-count is a measure of the relative intensity arriving at the detector. Estimations from the available data suggest that an ADC-count of 30000 is approximately equivalent to a power of ≈ 1 mW (detector saturation at ADC-count = 32768).

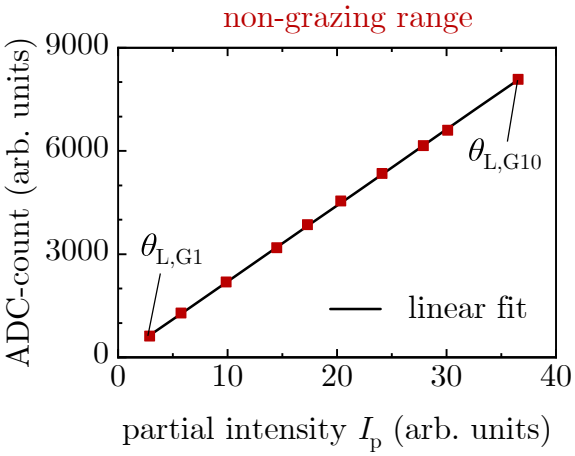

Figure A.4.5: Relationship between the partial intensity I_p and the ADC-count. The partial intensity I_p was determined by integrating the single beam spectrum between 1900 cm^{-1} and 2100 cm^{-1}. The ADC-count is utilised to verify the signal in the OPUS software [40]. The data points correspond to the measurements in Section 5.3.1 and were employed for optimising the non-grazing range. The plotted black curve represents the linear fit with the equation ADC-count = $220.8 \cdot I_p - 0.77$.

BIBLIOGRAPHY

[1] J. C. Védrine, *Metal oxides in heterogeneous catalysis* (Elsevier, 2018).

[2] F. Zaera, "New advances in the use of infrared absorption spectroscopy for the characterization of heterogeneous catalytic reactions", Chemical Society Reviews **43**, 7624 (2014).

[3] F. M. Hoffmann and M. D. Weisel, "Fourier transform infrared reflection absorption spectroscopy studies of adsorbates and surface reactions: Bridging the pressure gap between surface science and catalysis", Journal of Vacuum Science & Technology A: Vacuum, Surfaces, and Films **11**, 1957 (1993).

[4] G. Rupprechter, "Sum frequency generation and polarization–modulation infrared reflection absorption spectroscopy of functioning model catalysts from ultrahigh vacuum to ambient pressure", in *Advances in catalysis*, Vol. 51, edited by B. C. Gates and H. Knözinger, Advances in Catalysis (Academic Press, 2007), pp. 133–263.

[5] S. A. Francis and A. H. Ellison, "Infrared Spectra of Monolayers on Metal Mirrors", Journal of the Optical Society of America **49**, 131 (1959).

[6] R. G. Greenler, "Infrared Study of Adsorbed Molecules on Metal Surfaces by Reflection Techniques", The Journal of Chemical Physics **44**, 310 (1966).

[7] R. A. Shigeishi and A. King, "Chemisorption of Carbon Monoxide on Platinum {111}: Reflection-Absorption Infrared Spectroscopy", Surface Science **58**, 379 (1976).

[8] Campuzano and R. G. Greenler, "The Adsorption Sites of CO on Ni(111) as Determined by Infrared Reflection-Absorption Spectroscopy", Surface Science **83**, 301 (1979).

[9] R. F. Baddour, M. Modell, and R. L. Goldsmith, "Palladium-catalyzed carbon monoxide oxidation. Catalyst "break-in" phenomenon", The Journal of Physical Chemistry **74**, 1787 (1970).

[10] I. Ratajczykowa, "Hydrogen-palladium interaction studies by reflection-absorption infrared spectroscopy", Surface Science **48**, 549 (1975).

[11]H. G. Tompkins and R. G. Greenler, "Experimental development of reflection-absorption spectroscopy: Infrared spectrum of carbon monoxide adsorbed on copper and copper oxide", Surface Science **28**, 194 (1971).
[12]M. Kawai, T. Onishi, and K. Tamaru, "Oxidation of CO on a Pd surface: application of IR-RAS to the study of the steady state surface reaction", Applications of Surface Science **8**, 361 (1981).
[13]J. A. Mielczarski, "External reflection infrared spectroscopy at metallic, semiconductor, and nonmetallic substrates. 1. Monolayer films", The Journal of Physical Chemistry **97**, 2649 (1993).
[14]M. Moskovits, "Surface selection rules", The Journal of Chemical Physics **77**, 4408 (1982).
[15]H. Pearce and N. Sheppard, "Possible importance of a "metal-surface selection rule" in the interpretation of the infrared spectra of molecules adsorbed on particulate metals; infrared spectra from ethylene chemisorbed on silica-supported metal catalysts", Surface Science **59**, 205 (1976).
[16]G. A. Kimmel, M. Baer, N. G. Petrik, J. VandeVondele, R. Rousseau, and C. J. Mundy, "Polarization- and Azimuth-Resolved Infrared Spectroscopy of Water on TiO_2(110): Anisotropy and the Hydrogen-Bonding Network", The Journal of Physical Chemistry Letters **3**, 778 (2012).
[17]M. Creutzburg, K. Sellschopp, R. Gleißner, B. Arndt, G. B. Vonbun-Feldbauer, V. Vonk, H. Noei, and A. Stierle, "Surface structure of magnetite (111) under oxidizing and reducing conditions", Journal of Physics: Condensed Matter **34**, 164003 (2022).
[18]M. Xu, H. Noei, K. Fink, M. Muhler, Y. Wang, and C. Wöll, "The Surface Science Approach for Understanding Reactions on Oxide Powders: The Importance of IR Spectroscopy", Angewandte Chemie International Edition **51**, 4731 (2012).
[19]J. Kattner and H. Hoffmann, "External Reflection Spectroscopy of Thin Films on Dielectric Substrates", in *Handbook of Vibrational Spectroscopy*, Vol. 1, edited by P. Griffiths and J. M. Chalmers (John Wiley and Son Ltd., Chichester, 2002), pp. 1–19.
[20]Y. Wang and C. Wöll, "IR spectroscopic investigations of chemical and photochemical reactions on metal oxides: bridging the materials gap", Chemical Society Reviews **46**, 1875 (2017).
[21]N. A. Khan, A. Uhl, S. Shaikhutdinov, and H. .-. Freund, "Alumina supported model Pd–Ag catalysts: A combined STM, XPS, TPD and IRAS study", Surface Science **600**, 1849 (2006).
[22]J. Hoffmann, S. Schauermann, V. Johánek, J. Hartmann, and J. Libuda, "The kinetics of methanol oxidation on a supported Pd model catalyst: molecular beam and TR-IRAS experiments", Journal of Catalysis **213**, 176 (2003).
[23]N. G. Petrik, M. D. Baer, C. J. Mundy, and G. A. Kimmel, "Mixed Molecular and Dissociative Water Adsorption on Hydroxylated TiO_2(110): An Infrared Spectroscopy and Ab Initio Molecular Dynamics Study", The Journal of Physical Chemistry C **126**, 21616 (2022).
[24]C. R. O'Connor, M. F. Calegari Andrade, A. Selloni, and G. A. Kimmel, "Elucidating the water-anatase TiO2(101) interface structure using infrared signatures and molecular dynamics", The Journal of Chemical Physics **159**, 104707 (2023).

[25]N. G. Petrik and G. A. Kimmel, "Reaction Kinetics of Water Molecules with Oxygen Vacancies on Rutile TiO_2(110)", The Journal of Physical Chemistry C **119**, 23059 (2015).
[26]M. Setvin, M. Buchholz, W. Hou, C. Zhang, B. Stöger, J. Hulva, T. Simschitz, X. Shi, J. Pavelec, G. S. Parkinson, M. Xu, Y. Wang, M. Schmid, C. Wöll, A. Selloni, and U. Diebold, "A Multitechnique Study of CO Adsorption on the TiO_2 Anatase (101) Surface", The Journal of Physical Chemistry C **119**, 21044 (2015).
[27]N. G. Petrik and G. A. Kimmel, "Adsorption Geometry of CO versus Coverage on TiO_2(110) from s- and p-Polarized Infrared Spectroscopy", The Journal of Physical Chemistry Letters **3**, 3425 (2012).
[28]O. Seiferth, K. Wolter, H. Kuhlenbeck, and H.-J. Freund, "CO_2 adsorption on Na precovered Cr_2O_3(0001)", Surface Science **505**, 215 (2002).
[29]M. Buchholz, M. Xu, H. Noei, P. Weidler, A. Nefedov, K. Fink, Y. Wang, and C. Wöll, "Interaction of carboxylic acids with rutile TiO_2(110): IR-investigations of terephthalic and benzoic acid adsorbed on a single crystal substrate", Surface Science **643**, 117 (2016).
[30]C. Yang, Y. Cao, P. N. Plessow, J. Wang, A. Nefedov, S. Heissler, F. Studt, Y. Wang, H. Idriss, T. G. Mayerhöfer, and C. Wöll, "N_2O Adsorption and Photochemistry on Ceria Surfaces", The Journal of Physical Chemistry C **126**, 2253 (2022).
[31]J. Libuda, "Molecular Beams and Model Catalysis: Activity and Selectivity of Specific Reaction Centers on Supported Nanoparticles", ChemPhysChem **5**, 625 (2004).
[32]M. Bäumer, J. Libuda, K. M. Neyman, N. Rösch, G. Rupprechter, and H.-J. Freund, "Adsorption and reaction of methanol on supported palladium catalysts: microscopic-level studies from ultrahigh vacuum to ambient pressure conditions", Phys. Chem. Chem. Phys. **9**, 3541 (2007).
[33]H.-J. Freund, H. Kuhlenbeck, J. Libuda, G. Rupprechter, M. Bäumer, and H. Hamann, "Bridging the pressure and materials gaps between catalysis and surface science: clean and modified oxide surfaces", Topics in Catalysis **15**, 201 (2001).
[34]D. Rath, V. Mikerásek, C. Wang, M. Eder, M. Schmid, U. Diebold, G. S. Parkinson, and J. Pavelec, "Infrared reflection absorption spectroscopy setup with incidence angle selection for surfaces of non-metals", Review of Scientific Instruments **95**, 065106 (2024).
[35]P. R. Griffiths and J. A. de Haseth, *Fourier Transform Infrared Spectroscopy*, 2nd ed. (John Wiley & Sons, Inc., 2007).
[36]W. Demtröder, *Experimentalphysik 3*, Springer-Lehrbuch (Springer Berlin Heidelberg, Berlin, Heidelberg, 2016).
[37]Y. Ozaki, "Infrared Spectroscopy—Mid-infrared, Near-infrared, and Far-infrared/Terahertz Spectroscopy", Analytical Sciences **37**, 1193 (2021).
[38]D. A. Rath, "Design of an FTIR spectroscopy system for metal-oxide single crystals", M.Sc. thesis (Technische Universität Wien, Vienna, 2019).
[39]G. Schröder and H. Treiber, *Technische Optik*, 10th ed. (Vogel Communications Group GmbH & Co. KG, 2007).
[40]Bruker, *OPUS Base Package*, version 8.0, 2024.

[41]W. N. Hansen, "Electric Fields Produced by the Propagation of Plane Coherent Electromagnetic Radiation in a Stratified Medium", Journal of the Optical Society of America **58**, 380 (1968).
[42]W. N. Hansen, "Reflection spectroscopy of adsorbed layers", Symposia of the Faraday Society **4**, 27 (1970).
[43]J. A. Mielczarski and R. H. Yoon, "Fourier transform infrared external reflection study of molecular orientation in spontaneously adsorbed layers on low-absorption substrates", The Journal of Physical Chemistry **93**, 2034 (1989).
[44]Y. J. Chabal, "SURFACE INFRARED SPECTROSCOPY", Surface Science Reports **8**, 211 (1988).
[45]D. C. Langreth, "Macroscopic approach to the theory of reflectivity", Physical Review B **39**, 10020 (1989).
[46]M. N. Polyanskiy, "Refractiveindex.info database of optical constants", Scientific Data **11**, 94 (2024).
[47]S. Babar and J. H. Weaver, "Optical constants of Cu, Ag, and Au revisited", Applied Optics **54**, 477 (2015).
[48]M. Elshazly-Zaghloul and R. M. A. Azzam, "Brewster and pseudo-Brewster angles of uniaxial crystal surfaces and their use for determination of optical properties", Journal of the Optical Society of America **72**, 657 (1982).
[49]J. Kischkat, S. Peters, B. Gruska, M. Semtsiv, M. Chashnikova, M. Klinkmüller, O. Fedosenko, S. Machulik, A. Aleksandrova, G. Monastyrskyi, Y. Flores, and W. Ted Masselink, "Mid-infrared optical properties of thin films of aluminum oxide, titanium dioxide, silicon dioxide, aluminum nitride, and silicon nitride", Applied Optics **51**, 6789 (2012).
[50]M. Querry, *Optical constants*, CRDC-CR-85034 (US Army Armament, Munitions & Chemical Command, Chemical Research & Development Center, 1985).
[51]R. G. Tobin, "Asymmetric lines and background shifts in reflection-absorption infrared spectroscopy", Physical Review B **45**, 12110 (1992).
[52]A. Udagawa, T. Matsui, and S. Tanaka, "Fourier Transform Infrared Reflection Spectroscopy Studies of Organic Films Formed on Inorganic Substrates", Applied Spectroscopy **40**, 794 (1986).
[53]J. McIntyre and D. Aspnes, "Differential reflection spectroscopy of very thin surface films", Surface Science **24**, 417 (1971).
[54]D. L. Allara, A. Baca, and C. A. Pryde, "Distortions of Band Shapes in External Reflection Infrared Spectra of Thin Polymer Films on Metal Substrates", Macromolecules **11**, 1215 (1978).
[55]H. Brunner, U. Mayer, and H. Hoffmann, "External Reflection Infrared Spectroscopy of Anisotropic Adsorbate Layers on Dielectric Substrates", Applied Spectroscopy **51**, 209 (1997).
[56]P. B. Johnson and R. W. Christy, "Optical Constants of the Noble Metals", Physical Review B **6**, 4370 (1972).
[57]O. Gamba, H. Noei, J. Pavelec, R. Bliem, M. Schmid, U. Diebold, A. Stierle, and G. S. Parkinson, "Adsorption of Formic Acid on the Fe_3O_4(001) Surface", The Journal of Physical Chemistry C **119**, 20459 (2015).

[58]R. A. Dluhy, "Quantitative external reflection infrared spectroscopic analysis of insoluble monolayers spread at the air-water interface", The Journal of Physical Chemistry **90**, 1373 (1986).
[59]K. Ohta and H. Ishida, "Matrix formalism for calculation of electric field intensity of light in stratified multilayered films", Applied Optics **29**, 1952 (1990).
[60]J. Chaves, *Introduction to nonimaging optics*, 2nd ed. (CRC Press, Boca Raton, 2016).
[61]R. A. Chipman, W. S. T. Lam, and G. Young, *Polarized Light and Optical Systems* (CRC Press, Boca Raton, Aug. 10, 2018).
[62]J. Pavelec, "Surface chemistry setup and adsorption of CO_2 on $Fe_3O_4(001)$", PhD thesis (Technische Universität Wien, Vienna, 2019).
[63]J. Pavelec, J. Hulva, D. Halwidl, R. Bliem, O. Gamba, Z. Jakub, F. Brunbauer, M. Schmid, U. Diebold, and G. S. Parkinson, "A multi-technique study of CO_2 adsorption on Fe_3O_4 magnetite", The Journal of Chemical Physics **146**, 014701 (2017).
[64]D. Halwidl, *Development of an Effusive Molecular Beam Apparatus* (Springer Fachmedien Wiesbaden, Wiesbaden, 2016).
[65]Y. Wang, A. Glenz, M. Muhler, and Ch. Wöll, "A new dual-purpose ultrahigh vacuum infrared spectroscopy apparatus optimized for grazing-incidence reflection as well as for transmission geometries", Review of Scientific Instruments **80**, 113108 (2009).
[66]J. Kräuter and K. Al-Shamery, "Bulk defect-dependent initial steps of acetone oxidation on rutile $TiO_2(110)$", Molecular Physics **119**, e1963870 (2021).
[67]J. Libuda, I. Meusel, J. Hartmann, and H.-J. Freund, "A molecular beam/surface spectroscopy apparatus for the study of reactions on complex model catalysts", Review of Scientific Instruments **71**, 4395 (2000).
[68]S. Attia, E. J. Spadafora, J. Hartmann, H.-J. Freund, and S. Schauermann, "Molecular beam/infrared reflection-absorption spectroscopy apparatus for probing heterogeneously catalyzed reactions on functionalized and nanostructured model surfaces", Review of Scientific Instruments **90**, 053903 (2019).
[69]D. A. Rath, *Characterisation of the Bruker VERTEX 80v FTIR spectrometer*, internal report (TU Wien, 2019).
[70]A. Gericke, A. V. Michailov, and H. Hühnerfuss, "Polarized external infrared reflection-absorption spectrometry at the air/water interface: Comparison of experimental and theoretical results for different angles of incidence", Vibrational Spectroscopy **4**, 335 (1993).
[71]D. Blaudez, T. Buffeteau, B. Desbat, P. Fournier, A.-M. Ritcey, and M. Pézolet, "Infrared Reflection–Absorption Spectroscopy of Thin Organic Films on Nonmetallic Substrates: Optimal Angle of Incidence", The Journal of Physical Chemistry B **102**, 99 (1998).
[72]R. A. Chipman, "Polarization Analysis of Optical Systems", Optical Engineering **28**, 90 (1989).
[73]G. Yun, K. Crabtree, and R. A. Chipman, "Skew aberration: a form of polarization aberration", Optics Letters **36**, 4062 (2011).
[74]R. Clark Jones, "A New Calculus for the Treatment of Optical Systems IV", Journal of the Optical Society of America **32**, 486 (1942).

[75]S. Sgobba, *Materials for high vacuum technology, an overview*, technical report CERN-TS-2006-004 (CERN, 2006).
[76]R. Hudson, P. Gerakines, and M. Moore, "Infrared spectra and optical constants of astronomical ices: II. Ethane and ethylene", Icarus **243**, 148 (2014).
[77]S. Hu, Z. Wang, A. Mattsson, L. Österlund, and K. Hermansson, "Simulation of IRRAS Spectra for Molecules on Oxide Surfaces: CO on TiO_2(110)", The Journal of Physical Chemistry C **119**, 5403 (2015).
[78]M. Kunat, F. Traeger, D. Silber, H. Qiu, Y. Wang, A. C. Van Veen, Ch. Wöll, P. M. Kowalski, B. Meyer, C. Hättig, and D. Marx, "Formation of weakly bound, ordered adlayers of CO on rutile TiO_2(110): A combined experimental and theoretical study", The Journal of Chemical Physics **130**, 144703 (2009).
[79]V. Mikerásek, *Characterisation and alignment of the newly developed grazing incident infrared absorption spectroscopy unit - GRISU*, internal report (TU Wien, 2022).
[80]P. Scheiber, A. Riss, M. Schmid, P. Varga, and U. Diebold, "Observation and Destruction of an Elusive Adsorbate with STM: O_2/TiO_2(110)", Physical Review Letters **105**, 216101 (2010).
[81]M. A. Henderson, "An HREELS and TPD study of water on TiO_2(110): the extent of molecular versus dissociative adsorption", Surface Science (1996).
[82]M. A. Henderson, "Structural Sensitivity in the Dissociation of Water on TiO_2 Single-Crystal Surfaces", Langmuir **12**, 5093 (1996).
[83]M. B. Hugenschmidt, L. Gamble, and C. T. Campbell, "The interaction of H_2O with a TiO_2(110) surface", Surface Science **302**, 329 (1994).
[84]C. L. Perkins and M. A. Henderson, "Photodesorption and Trapping of Molecular Oxygen at the TiO_2(110)–Water Ice Interface", The Journal of Physical Chemistry B **105**, 3856 (2001).
[85]E. Herceg, H. Celio, and M. Trenary, "Sensitivity improvement in surface infrared spectroscopy: Design, characteristics, and application of a high-temperature graphite source", Review of Scientific Instruments **75**, 2545 (2004).
[86]A. Schwaighofer, M. Brandstetter, and B. Lendl, "Quantum cascade lasers (QCLs) in biomedical spectroscopy", Chemical Society Reviews **46**, 5903 (2017).
[87]C. K. Akhgar, G. Ramer, M. Żbik, A. Trajnerowicz, J. Pawluczyk, A. Schwaighofer, and B. Lendl, "The Next Generation of IR Spectroscopy: EC-QCL-Based Mid-IR Transmission Spectroscopy of Proteins with Balanced Detection", Analytical Chemistry **92**, 9901 (2020).